

# The North Atlantic circulation derived from inverse models

DISSERTATION

zur

Erlangung des Grades

Doktor der Naturwissenschaften

— Dr. rer. nat. —

dem Fachbereich I (Physik/Elektrotechnik) der  
Universität Bremen  
vorgelegt von

**Dmitry Sidorenko**

December, 2004

1. Gutachter: Prof. Dr. D. Olbers
2. Gutachter: Prof. Dr. R. Schlitzer

ALFRED-WEGENER-INSTITUT FÜR POLAR- UND MEERESFORSCHUNG



# Übersicht

Diese Arbeit stellt zwei Modelle zur Bestimmung der quasistationären Ozeanzirkulation im Nordatlantik vor und behandelt ihre Ergebnisse. Beide Modelle nutzen die adjungierte Methode und eine Diskretisierung durch finiten Elemente, um eine genauere Darstellung der Bodentopographie zu erreichen.

Zum einen wird das Inversmodell FEMSECT (Losch et al., 2004) zur Untersuchung hydrographischer Schnitte zusammen mit Ergebnissen aus der Anwendungen auf die Framstrasse präsentiert. FEMSECT verwendet die thermische Windrelation, um das Geschwindigkeitsfeld relativ zu einem Referenzniveau zu bestimmen. Damit wird im Sinne kleinster Quadrate ein optimaler Kompromiss zwischen Modell, sowie hydrographischen und Verankerungsdaten gesucht. Die Kontrollparameter sind die Referenzgeschwindigkeiten, und hydrographischen Felder. Die Neuerung dieses Modells ist die Fähigkeit, Bodendreiecke zu berücksichtigen.

Inversmodelle dieser Art sind Standardwerkzeuge zur Bestimmung von Transporten durch hydrographische Schnitte, jedoch ist es nicht möglich, Volumenerhaltung zu garantieren. Das Inversmodell IFEOM (Inverse Finite Element Ocean Model) das im Anschluss diskutiert wird, garantiert Volumenerhaltung lokal und global und nutzt darüberhinaus die Flexibilität und die Vorteile der Diskretisierung mit Finiten Elementen. Es basiert auf einer stationären Version des Ozeanmodells FEOM (Finite Element Ocean Model, siehe (Danilov et al., 2004a)). Aus den Impulsgleichungen wird ein stationäres Geschwindigkeitsfeld bestimmt, wobei die stationäre Dichtegleichung als schwache Zwangsbedingung eingeht. Um die Differenz zwischen FEOM Modellergebnissen und der diagnostizierten Ozeanzirkulation zu verringern wird eine zusätzliche Zwangsbedingung an den Dichtegradienten unter 2000 m Tiefe vorgeschlagen. Die Bedeutung dieser Massnahme wird im Anschluss daran diskutiert.

Schliesslich wird die Zirkulation im Nordatlantik durch Assimilierung verschiedener Datensätze abgeschätzt, darunter die Levitus Klimatologie Levitus 1994, neun Pentaden (von 1950 bis 1994) der Klimatologie von Lozier et al. (1995) sowie die Klimatologie von Gouretski and Koltermann (2004) die erst seit kurzer Zeit verfügbar ist. Es werden Transportabschätzungen durch verschiedene Schnitte (A5, AR1, A2, M50 und AR7E) berechnet und mit Ergebnissen anderer Studien verglichen.

Es stellt sich heraus, dass die Strömung, die aus der optimierten Levitus Hydrographie resultiert, die Transporte durch die meisten Schnitte unterschätzt. Transportvariabilität, meridionales Overturning sowie die barotrope Stromfunktion werden durch Assimilation jeder einzelnen der Lozier-Pentaden bestimmt. Die Lösung aus der Assimilation des Datensatzes von Gouretski and Koltermann (2004) reproduziert viele Eigenschaften der Zirkulation besser als die anderen Klimatologien.

Die Ergebnisse sind ermutigend und beweisen, dass IFEOM sehr gut geeignet ist, die Ozeanzirkulation durch Assimilation von qualitativ hochwertigen klimatologischen Datensätzen zu bestimmen.

# Abstract

This thesis describes two inverse models solving for a quasi-stationary ocean circulation, and discusses the circulation in the North Atlantic as derived from them. Both models are based on the adjoint technique and use finite-element discretization to accurately represent the sloping bottom topography.

First a finite element inverse section model FEMSECT (Losch et al., 2004) is presented together with results of applying it to Fram Strait. FEMSECT exploits the thermal wind relation to estimate the velocity with respect to some reference level, and seeks for a compromise in the least square sense between the hydrographic and mooring data. Its control parameters are the reference velocities and hydrographic fields. Its novel feature is the ability to take into account the bottom triangles.

Such inverse models are a standard tool to derive ocean transports from hydrographic measurements. However, they are not able to take into account the continuity constraint. The inverse finite element ocean model (IFEOM) presented afterwards respects the continuity locally and globally and also exploits the flexibility of 3D finite element grids. It is based on a steady-state version of the finite element ocean general circulation model FEOM (Danilov et al., 2004a). A steady state velocity field is determined from the momentum equations by the density field, and the stationary equation for the potential density is accounted for as a soft constraint. The IFEOM solves for density by minimizing the misfit between it and the density data under strong momentum and weak tracer balance constraint. Using an additional deep pressure gradient constraint (below 2000 m) is suggested and shown to be crucial for keeping the integral properties of the diagnosed ocean circulation close to those of the forward run of FEOM.

The circulation in the North Atlantic is estimated by assimilating several data sets which include the Levitus 1994 climatology, nine pentades (from 1950 to 1994) of the climatology by Lozier et al. (1995) and climatology by Gouretski and Koltermann (2004) that has become available only recently. The transport estimates through several sections (A5, AR1, A2, M50 and AR7E) are compared for different solutions and with available results of other studies. The circulation obtained by diagnosing the Levitus optimized hydrography was found to underestimate the transports through most sections. The variability of transports, meridional overturning and barotropic streamfunction is obtained by assimilation of each of the Lozier pentades separately. Finally the

solution obtained by assimilating the dataset of Gouretski and Koltermann (2004) reproduced features of circulation better than other climatologies.

The results are encouraging and indicate that IFEOM can be used to assimilate a climatological circulation from high quality hydrographic measurements.

# Contents

<b>Übersicht</b>	<b>3</b>
<b>Abstract</b>	<b>5</b>
<b>1 Introduction</b>	<b>9</b>
<b>2 Data and Models</b>	<b>13</b>
2.1 Databases on hydrography . . . . .	13
2.2 Reference level velocity . . . . .	15
2.3 Models for single sections . . . . .	16
2.4 Models for closed domains (Wunsch's method) . . . . .	17
2.5 Box Inverse models . . . . .	18
2.6 GCM-based inverse models . . . . .	22
2.7 Principles of Finite Elements method . . . . .	25
<b>3 Finite Element Inverse Section Model</b>	<b>29</b>
3.1 Model Construction . . . . .	30
3.2 Discretization of the Model Equations . . . . .	31
3.3 Testing the Discretized Thermal Wind Equations in Idealized Geometry: Triangular Domain . . . . .	34
3.4 A First Application: Fram Strait . . . . .	35
3.5 Conclusion . . . . .	40
<b>4 Inverse Finite Element Ocean Model</b>	<b>41</b>
4.1 Finite Element Ocean Model (FEOM) . . . . .	42
4.1.1 Model equations . . . . .	42
4.1.2 Finite element discretization . . . . .	44
4.1.3 Velocity correction . . . . .	46
4.1.4 Equation for the potential density . . . . .	46
4.1.5 Discrete formulation . . . . .	47
4.2 Constructing the IFEOM . . . . .	49
4.2.1 Control and dependent variables . . . . .	49
4.2.2 Cost Function . . . . .	49
4.2.3 Deriving the adjoint equations . . . . .	50
4.2.4 Sea surface height correction . . . . .	54

4.2.5	Discrete formulation . . . . .	55
<b>5</b>	<b>North Atlantic circulation</b>	<b>59</b>
5.1	Model setup . . . . .	61
5.2	Analysis of climatology data . . . . .	62
5.3	Forward estimate . . . . .	68
5.4	Choosing weights . . . . .	72
5.5	Experiment: Assimilation of Levitus Climatology . . . . .	74
5.6	Constraint on the deep pressure gradient . . . . .	75
5.7	Experiment: <b>LEV</b> . . . . .	79
5.8	Experiment: <b>LOZ</b> . . . . .	84
5.9	Remark on the velocity field . . . . .	89
5.10	Experiment: <b>GUR</b> . . . . .	90
5.11	Transports . . . . .	95
5.12	Interpentadal variability . . . . .	99
<b>6</b>	<b>Conclusions</b>	<b>103</b>
	<b>Acknowledgements</b>	<b>111</b>

# Chapter 1

## Introduction

The world ocean is an important part of the earth climate system. It interacts with the earth atmosphere exchanging heat and moisture, which also influences properties of water masses. The ocean currents and large-scale circulation redistribute these water masses over broad area thus making the interaction between the ocean and atmosphere non-local. The knowledge of the large-scale ocean circulation and its trends and variability is required to improve both our understanding of the earth climate system and our skill in predicting its changes.

Our current knowledge on the ocean general circulation is based on numerous observations and theoretical and modeling efforts. The observations are in many cases indirect or contaminated by superposition of transient signals from tides or different wave processes that mask slowly varying large-scale signals. Additionally, even with current dedicated efforts like World Ocean Circulation Experiment (WOCE) the coverage of the ocean with sections is still insufficient to judge about details of ocean circulation and its variability.

Theoretical and numerical models, on the other hand, are capable of providing us with solutions describing the circulation within some specified area, but under a set of simplifying assumptions concerning model geometry and a number of parameterization used to replace unresolved physical processes taking place in the real ocean. Although permanently improving due to advances in computer technology, current numerical models are still far from being able to represent the real ocean reliably.

A distinctive feature of solutions provided by numerical models is dynamic consistency — velocity, temperature and salinity fields are varying in a concerted way determined by the equations of motion and advection–diffusion. Raw observational data do not necessarily satisfy these equations because of many factors including the above-mentioned transient effects and the simple fact that their spatial coverage is typically insufficient to approximate differential operators in equations of motion with reasonable accuracy.

The best strategy under such circumstances is to combine observational data and ocean models and seek for compromise between them guided by a

priori information on data and model errors, and, possibly, additional constraints — the approach based on least-squares techniques and known under several general names such as data assimilation or inverse method.

This thesis follows this line of research and seeks in its two main parts (chapters 3 and 4) for such approaches as applied to two types of problems. The first one (chapter 3) is the old problem of observational oceanography — deriving transport through sections based on hydrographic data. The novel features suggested here is (i) combining the solution to these equations with hydrographic and mooring data in the least squares sense. (ii) using finite elements to solve the thermal wind equations. The former feature serves to overcome the problem of reference level velocity while latter offers a seamless strategy to take bottom triangles to be taken into account for transport estimates. This part of the work was done together by M. Losch and the author, and lead to the development of the model called FEMSECT that is currently employed at AWI. The application of FEMSECT model to the section across Fram Strait to was done by A. Beszczynska-Müller where she estimated variability of heat and volume transports.

The second approach (chapters 4 and 5) seeks to combine data and a model based on stationary primitive equations. The data could be on temperature or salinity as provided by standard CTD measurements, and on sea surface height as provided by altimetry. The model used here is the Finite-Element Ocean circulation Model (FEOM) developed at AWI. The compromise between the model solution and data is achieved by minimizing the cost function which penalizes both the deviation of the model density from the data and the residual in model equations, and also includes several other constraints that reflect our a priori knowledge about the ocean. A solution to the minimization problem is obtained by adjoint technique common for such type of problems and also used in FEMSECT. Using this technique required development of the adjoint to stationary FEOM, a task facilitated by the fact that the basic part of FEOM is formulated in term of matrix subproblems.

This approach is called further the Inverse Finite-Element Ocean Model (IFEOM). It is first applied to reconstruct the circulation in the North Atlantic based on the the most widely used Levitus climatology (Levitus and Boyer, 1994; Levitus et al. 1994). Second it is applied to nine pentades of Lozier climatology (Lozier et al., 1995) covering the period from 1950 to 1994 and to the novel climatology dataset by Gouretski and Koltermann (2004). We compute integral characteristics of the North Atlantic circulation such as the barotropic streamfunction and meridional overturning circulation as well as transports through several WOCE sections and compare our results with other available estimates obtained by other methods. The inversions of mean Lozier climatology and that of Gouretski and Koltermann (2004) agree much better with other estimates available than the inversion of Levitus data. The inversion of separate pentades of the Lozier climatology shows only limited variability with standard deviation of several Sv for the barotropic streamfunction and

around 0.5 Sv for the meridional overturning.

The key ingredient of the IFEOM allowing successful assimilation of data without destroying dynamical balances is the deep pressure gradient constraint suggested by the author. The gradient of deep pressure is required to be close to that in the forward run of FEOM averaged over a certain period of time. The physical motivation behind this constraint is based on the fact that the deep ocean (well below the main thermocline) should be minimally changed by data assimilation and main changes should occur in the density structure of the upper layers. Without this constraint, there is tendency to produce non-balanced hydrostatic pressure and surface pressure gradients when assimilating the density (or temperature and salinity) data. This shows up as bias barotropic velocity in the ocean circulation.

The thesis is organized as follows. Chapter 2 is an introductory one. It describes some hydrographic data sets and gives a short overview of main approaches used to estimate the ocean circulation. Chapters 3, 4 and 5 present FEMSECT and IFEOM and their results, respectively, and section 6 concludes.



# Chapter 2

## Data and Models

Observations are essential for understanding the ocean and form a basis to our knowledge of the ocean circulation. However, a considerable part of information on the ocean fields comes from CTD instruments providing one with temperature and salinity at some set of levels along sections. The current meter measurements are still not that dense as the hydrography data in most places of the world ocean, and are more prone to errors due to transient processes of various types (mostly because the amplitudes of the large-scale ocean currents are relatively small). In order to estimate the ocean large-scale circulation based on the hydrography data, one needs to use equations of dynamics and thermodynamics under certain sets of assumptions. This gave birth to a variety of models and approaches to estimating the ocean circulation, and the main aim of this section is to briefly review some of them that are relevant to the topic of this thesis. Also, our focus will be on the circulation in the North Atlantic so that the review here will be mostly concerned with models dealing with estimates of the circulation in the North Atlantic or global estimates. We begin, however, with description of three data sets used by us in chapter 5 for estimates of circulation in the North Atlantic — the World Ocean Atlas by Levitus et al. (1994); Levitus and Boyer (1994), the Lozier data set (Lozier et al., 1995) and the most recent set by Gouretski and Koltermann (2004). It is followed by description of models, and finally, a brief description of the finite element method used in both the FEMSECT and IFEOM.

### 2.1 Databases on hydrography

In addition to direct measurements of hydrography there are climatology databases available. They are based on direct measurement data projected on regular grids and smoothed using appropriate algorithms.

The climatology of the World Ocean produced by Levitus (1982) became commonly used as the reference data base within the oceanographic community. In the context of this work we mention that the inverse models by Olbers et al. (1985), Schiller (1995) and Yu and Malanotte-Rizzoli (1996) used it as

data in their optimizations. This climatology was followed by the World Ocean Atlas 1994 (WOA94) (Levitus et al., 1994; Levitus and Boyer, 1994) and World Ocean Databases 1998 and 2001 (WOD98 and WOD01), (Levitus et al., 1998; Conkright et al., 2002). These are atlases of objectively analyzed fields of major ocean parameters at the annual, seasonal, and monthly time scales. We will be using WOA94 climatology as data in chapter 5. The inverse model by Yu and Malanotte-Rizzoli (1998) also uses it for this purpose.

The dataset of WOA94 covers the global ocean at one degree resolution down to 5500m depth. The units and number of data points for temperature and salinity from WOA94 are indicated in the table 2.1.

Parameter	Unit	$N$ of Profiles
Temperature	degrees $^{\circ}C$	4,553,426
Salinity	p.s.u.	1,254,771

Table 2.1: Units and number of profiles for Temperature and Salinity in WOA94

The two other data sets are used less widely. The data set by Lozier et al. (1995) contains the annual mean climatology of the North Atlantic. It is constructed from measurements based on 143,879 hydrographic stations. To complete the hydrography in gaps averaging among the stations was used in conjunction with interpolation (Lozier et al., 1995). Resulting climatology represents a record on a  $1^{\circ} \times 1^{\circ}$  resolution grid. The distance between levels does not exceed 100 m.

The precision and resolution of climatology records depend on the set of available hydrography data. The biggest experiment whenever done to measure ocean properties was the World Ocean Circulation Experiment (WOCE), a component of the World Climate Research Program (WCRP). The main objective of WOCE was hydrography since it is the principal source of information about the ocean circulation. Hydrographic measurements within WOCE were made between 1990 and 1998, and Fig. 2.1 shows the map of WOCE one time surveys. The distribution of measurements is sparse in space and time and has different temporal scales.

The characteristic feature of the WOCE project is that the same types of devices were used for all measurements. The CTD sensors to measure conductivity  $C$ , temperature  $T$ , and pressure  $p$  versus time were calibrated against certified transfer standards. It is essential for accurate measurements and mapping of deep layers.

The WOCE Global Hydrographic Climatology (Gouretski and Koltermann, 2004) was produced combining already available databases and datasets from the WOCE experiment. According to Gouretski and Koltermann (2004) the WOCE Hydrographic program produced a data-set of unprecedented quality and substantially improved the data coverage for the deeper layers of the World Ocean.

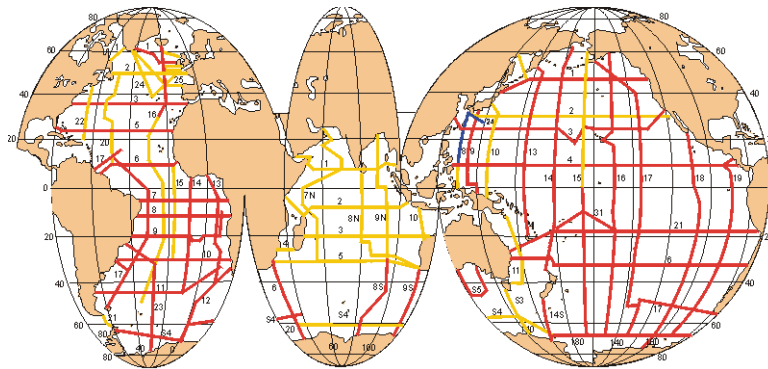


Figure 2.1: WOCE Hydrographic Programme One Time Survey. Adopted from <http://woce.nodc.noaa.gov/>

One of the major differences between these three climatologies is the scale they were smoothed over. For instance Lozier et al. (1995) analyzed North Atlantic with denser number of measurements than Levitus (1982) and smoothed the hydrography on much smaller scales (Myers et al., 2004) thus being able to retain sharp gradients in the hydrography (Marotzke and Willebrand, 1996).

In the following three data sets are used to obtain the velocity field of the North Atlantic and its associated properties. First we chose the WOA94 as the dataset used most widely in this context. Second, the Lozier et al. (1995) climatology was selected as it reproduces much finer scales and includes averaged fields of temperature and salinity for a set of 9 pentades (1950–1994). Finally we used the novel dataset by Gouretski and Koltermann (2004) which is the most recent one and became available to us in September 2004.

## 2.2 Reference level velocity

The large-scale circulation in the ocean is known to be approximately in geostrophic and hydrostatic balances expressed by the equations

$$-fv = -\frac{p_x}{\rho_0}, \quad (2.1)$$

$$fu = -\frac{p_y}{\rho_0}, \quad (2.2)$$

$$0 = -p_z - \rho g, \quad (2.3)$$

Here  $f$  is the Coriolis parameter,  $u, v$  are the components of the horizontal velocity,  $\rho$  and  $\rho_0$  are the density and a constant reference value, respectively,  $x, y, z$  denote Cartesian coordinates with  $z$  oriented upward (Cartesian coordinates will be used for simplicity of notation). The geostrophic and hydrostatic

relations could be combined to give the thermal wind equations

$$-fv_z = (g/\rho_0)\rho_x, \quad (2.4)$$

$$fu_z = (g/\rho_0)\rho_y. \quad (2.5)$$

Choosing the coordinate  $x$  be along the given hydrographic section and  $v$  be the cross-section velocity one can integrate (2.4) to obtain

$$v(\mathbf{x}, z) = v_0(\mathbf{x}) - \frac{g}{\rho_0 f} \int_{z_0}^z \rho_x(\mathbf{x}, \zeta) d\zeta, \quad (2.6)$$

or simply

$$v(\mathbf{x}, z) = v_0(\mathbf{x}) + v'(\mathbf{x}, z) \quad (2.7)$$

where  $v_0$  is the horizontal velocity at depth  $z_0$  (reference velocity). Since information on  $\rho$  is retrieved from hydrographic data, the only parameter which remains unknown is  $v_0$ . There is no obvious way of estimating it directly. The simplest choice is to assume the existence of a "level of no motion" where one can set  $v_0 = 0$ . While appropriate for some regions (in particular, for a part of the North Atlantic where it would be close to 2000 m), it could be very poor in other places of the ocean.

Wunsch (1977) (see also Wunsch (1996)) suggested combining the thermal wind equations with additional information in a least squares sense in order to constrain the reference velocity. As additional information, he uses the balance of tracers and mass in separate layers in the section. His approach came to be known as a Wunsch's method and was originally applied to a sector of the ocean close to the Florida coast (see Fig. 2.2). Many other models were formulated since then based on similar principles but exploiting different geometry and sets of constraints, and also differing in the set of control parameters. They could be broadly classified into section models and box models depending on the geometry.

## 2.3 Models for single sections

Here we only mention the recent inverse section models by Nechaev and Yaremchuk (1995) and Losch et al. (2002) that were motivating us in designing the FEMSECT. The important feature introduced by them is allowing for a misfit between the model temperature and salinity and the hydrography data and adding temperature and salinity to the list of control parameters. This increases the number of the degrees of freedom yet accounts for the fact that the hydrography data could contain errors. This approach is adopted by us in the FEMSECT. The set of constraints included in the cost function in the section models could be rather broad in the general case. For example, besides the deviations of the model state from the data, which are hydrography, current

meters and sea surface elevation Losch et al. (2002) penalize the imbalances of the vorticity equation via the boundary condition for the vertical velocity at the surface and at the bottom. Additionally, they penalize terms neglected in the tracer conservation equation. In order to estimate imbalances for the vorticity equation and be able to account for the tracer conservation equation Losch et al. (2002) make use of a staggered model grid suggested in Nechaev and Yaremchuk (1995)

The section models are based on finite difference grids which results in stepwise representation of the bottom topography. Correspondingly, the transport through the bottom triangles presents a problem for such models (solving it would require a kind of data extrapolation). The FEMSECT inverse model described in section 3 solves this problem in a natural way by employing the finite element discretization. The FEMSECT enables one to approximate bottom in a smooth (as opposed to stepwise) way and uses least squares technique to combine hydrography and mooring data.

## 2.4 Models for closed domains (Wunsch's method)

Wunsch (1977) showed that the reference velocities could be estimated around a closed path of the ocean (Fig.2.2) by using tracer conservation constraints. He divided the water column everywhere in between two stations into a number of layers of different temperature ranges. Let there be  $M$  layers of different temperature ranges occupying the total water column. Denote the thermal wind estimate by  $v'_n(z)$ , and the unknown bottom velocities between the  $n$ th station pair by  $v_{n0}$ , where  $1 \leq n \leq N$ . Let  $\bar{v}'_{mn}$  denote the mean value of  $v'_n$  in the  $m$ th layer of water column, where  $1 \leq m \leq M$ .

The assumption made by Wunsch is that the tracer (temperature in his case) is conserved within each layer

$$\sum_{n=1}^N (\bar{v}'_{mn} + v_{n0}) \Delta z_{mn} \Delta x_n = 0, (1 \leq m \leq M), \quad (2.8)$$

where property  $m$  occupies a depth range  $\Delta z_{mn}$  at the station pair  $n$  and  $\Delta x_n$  denote the separation of the  $n$ th station pair respectively (Wunsch, 1977). With respect to the reference level velocity  $v_{n0}$ ,  $1 \leq n \leq N$ , (2.8) might be rewritten in the matrix form

$$\mathbf{A} \mathbf{v}_0 = \mathbf{b}, \quad (2.9)$$

where  $\mathbf{v}_0 = \{v_{n0}, 1 \leq n \leq N\}$ , the matrix  $\mathbf{A}$  has a dimension of  $(M \ N)$ .

This way there are  $M$  constraints for  $N$  unknowns. Since usually  $M \leq N$  system (2.9) appears to be underdetermined. Wunsch chooses the Moore-Penrose inverse  $\mathbf{A}^{-1} = \mathbf{A}^T (\mathbf{A} \mathbf{A}^T)^{-1}$  to construct a solution

$$\mathbf{v}_0 = \mathbf{A}^T (\mathbf{A} \mathbf{A}^T)^{-1} \mathbf{b}. \quad (2.10)$$

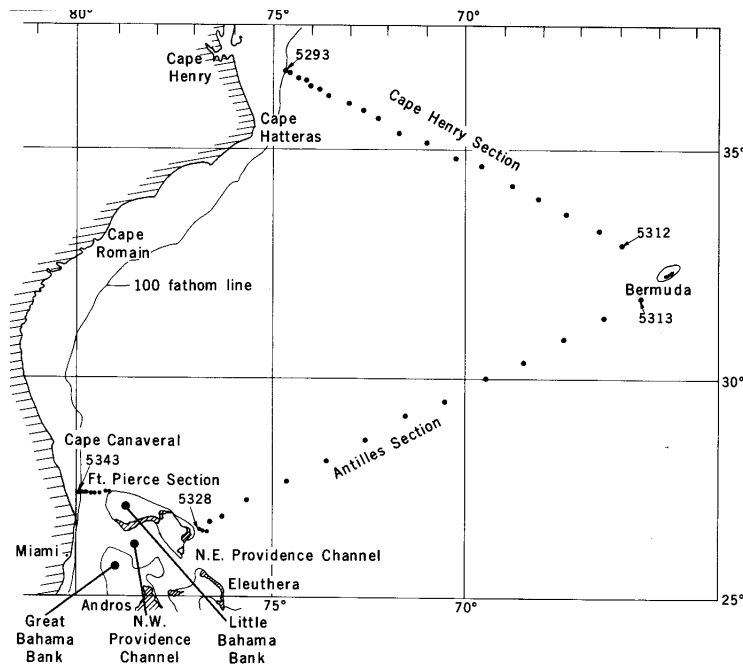


Figure 2.2: Locations of Atlantis 215 stations used by Wunsch. They nearly confine a volume of ocean including the Gulf Stream, after Wunsch (1977).

Several modifications of this procedure are also suggested. The first one involves weighting the unknowns and another derives from recognizing that there are errors in the measurements. Wunsch applied this technique to the closed path in the Western North Atlantic shown in Fig.2.2 and obtained estimates of total transports and transports in four temperature classes. The consequence of introducing errors is that the tracer is not conserved within each layer, and globally.

## 2.5 Box Inverse models

Box models are descendants of the Wunsch's method. They usually operate with multiple layers of water with distinct properties and constraint balances within each layer in a box. They are relatively numerous and better fitted to derive the pattern of transport and overturning in the ocean than the section models. The box inverse models by Roemmich and Wunsch (1985), Rintoul and Wunsch (1991), Macdonald (1995), Macdonald (1998), Ganachaud and Wunsch (2000), Ganachaud and Wunsch (2003) and Lumpkin and Speer (2003) contributed essentially into the current picture of ocean mass and heat fluxes in the North Atlantic or the global ocean. The work by Lumpkin and Speer (2003) gives a short summary of previous efforts and suggest the most complete inversion of hydrography data in the North Atlantic known to us. Fig. 2.3

and 2.4 present, respectively, the geometry of sections used for the inversion and definition of the boxes, and results of the inversion for the circulation in the thermocline and deep ocean. The neutral density surface  $\gamma^n = 27.6$  is used to separate between the upper and deep transports. Fig. 2.4 also displays in panels the net meridional overturning trough separate sections. The inversion results agree well with earlier estimates from global inversions by Ganachaud and Wunsch (2000) ( $14 \pm 2$  and  $16 \pm 2$  through sections A2 and A5 respectively) yet differ in detail for separate transports. The biggest difference with respect to estimates of other authors occurs for the estimates of the transport of the North Atlantic Current through section A2 (we present them in table 5.2 in chapter 5).

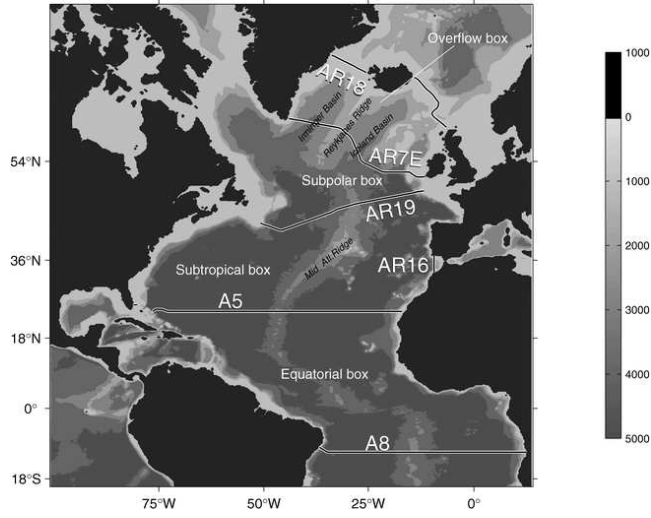


Figure 2.3: Geometry of the box inverse model of Lumpkin and Speer (2003), superimposed on the bathymetry. Five hydrographic sections are used to divide the North Atlantic into four boxes. After Lumpkin and Speer (2003).

The set of constraints used in Lumpkin and Speer (2003) accounts for the sink/sources, diapycnal fluxes, mixing and flux through the outcropping areas of property  $C$ . These constraints take the form

$$\sum_{j=1}^N \left[ \Delta x_j \int_i C_j (v'_j + v_{0j}) dz + (1 + e^*) \Psi_{EK,ij} C_{j,10m} \right] + \bar{C}_{i-1} A_{i-1} - \bar{C}_i A_i + F_{c,i} + F_{c,i}^* + (\partial_\rho D_c)_{i-1} - (\partial_\rho D_c)_i \approx 0, \quad (2.11)$$

where  $i$  is the layer number,  $C_j(z)$  is the pair averaged profile of property  $C$ ,  $e^*$  is a fractional adjustment to each section's Ekman transport  $\Psi_{EK}$ ,  $\bar{C}_i$  is the interface-averaged value of  $C$  within the box,  $F^*$  is an adjustment to the air-sea input of  $C$ ,  $A_i$  is the diapycnal advection and  $\partial_\rho D_c$  is the diffusion.

If  $C = \rho$  (potential density) then  $F_c = \rho_{fw} F_{fw}$ , and  $\partial_\rho D_c = 0$ , where  $F_{fw}$  is the fresh water flux ( $P - E$ ) integrated over the layer's outcrop area. Lumpkin

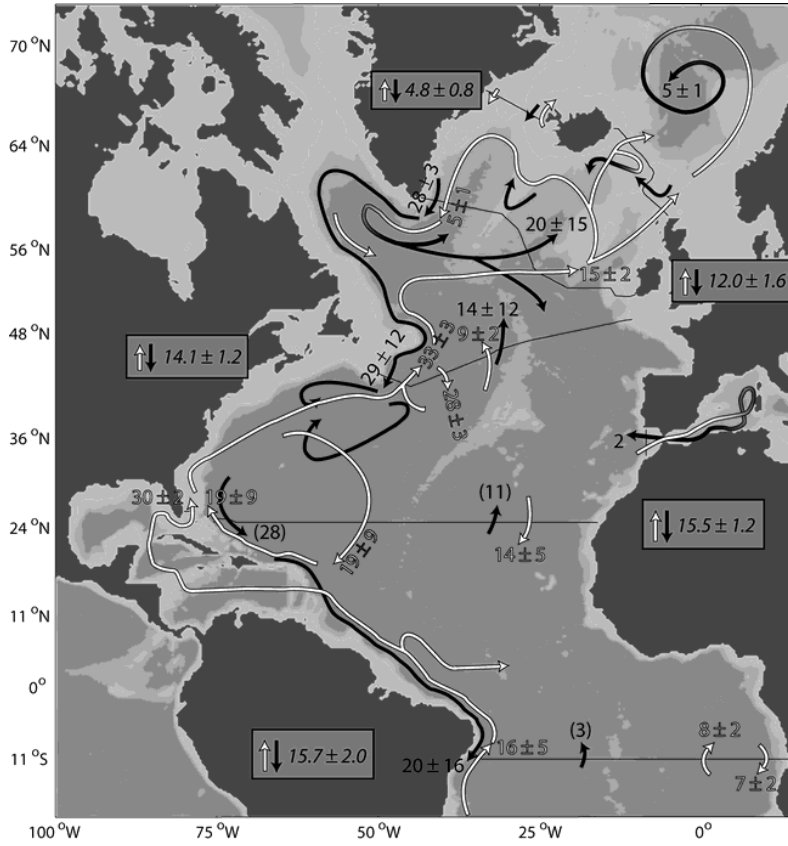


Figure 2.4: Circulation of thermocline (white arrows;  $\gamma^n < 27.6$ ) and deep (black arrows;  $\gamma^n > 27.6$ ) water in the inverse solution. Numbers indicate transport (Sv) where currents cross the hydrographic sections; values in parentheses are not well-determined in the solution. The strength of the net overturning exchange between these layers is given in the small panels. After Lumpkin and Speer (2003).

and Speer (2003) use Gauss-Markov estimation (Wunsch, 1996) to solve for the unknowns:  $v_0$  for each station pair,  $e^*$  for each hydrographic section,  $F$ ,  $F^*$  for outcropping layers in each box and  $\partial_\rho D_c$  across each interface within each box. We will compare our inversion to those of Lumpkin and Speer (2003) in chapter 5.

The common feature of box models is using ‘large-scale’ balances to constrain the circulation in the ocean. Indeed, the balances are applied to large volumes of water masses within a box. In reality, they are observed on a local level. Therefore, although the box models are successful and valuable in supplying us with estimates of the ocean circulation there is need for inverse models that impose constraints on a local level. These models are generally much more involved in terms of the problem size and CPU time required for inversion.

A special class of such models is exemplified by those based on the  $\beta$ -spiral method. The detailed discussion of the method and the estimate of circulation and diffusivity coefficients in the North Atlantic derived from the Levitus 1982 data set at resolution of  $1^\circ$  can be found in the paper by Olbers et al. (1985). It also contains a brief overview of earlier works using this method. A short explanation of the  $\beta$ -spiral method could also be found in Bennett (2002) and Wunsch (1996). Its essential feature is that the inversion is done locally and involves only information in a set of vertically aligned nodes. Solving 3D boundary-value problems to compute the velocity field is not needed. This is simultaneously the advantage and disadvantage of the method: it reduces the CPU requirements on the one hand, but does not observe the mass (volume) balance on the other which would have required solving a global problem. Wenzel (1986) recovered the mass balance for the solution of Olbers et al. (1985) by introducing a potential for the velocity field.

Two other models suggested by Martel and Wunsch (1993) and Mercier and Ollitrault (1993) consider continuity and tracer balance equations on local level, yet they only estimate, and not solve them, by including them as weak constraints in their cost functions. Correspondingly, mass is not conserved in their solutions, and by their structure they remain very close to the box models. Both introduce geostrophic velocities with respect to some reference level and include reference velocity in the set of control parameters. Martel and Wunsch (1993) solve the minimization problem for the reference velocities and diffusivity coefficients. The continuity and stationary tracer equations are discretized on a  $1^\circ$  mesh. The objective function penalizes residuals of the equations and the norm of solution. However, to reduce the size of the problem, its grid is treated as a nested one, and equations are integrated over combinations of small cells reducing the number of unknowns about to 29000.

The model of Mercier and Ollitrault (1993) uses a coarser grid than the previous one, with spacing  $2^\circ$  in latitude and  $2.5^\circ$  in longitude. In addition to reference velocities, it also looks for the density field EOF coefficients thus allowing errors in the density field. Mass, heat and salt conservation is imposed in a weak sense for every vertical column, and an additional constraint at the reference level is the planetary vorticity balance. The total number of unknowns is about 5000.

The model by Schlitzer (1993) (see also Schlitzer (1995)) is different from the models mentioned above in several important aspects. First, the model uses finite volume principles to discretize mass, heat and salt balances. Second, the balances are solved exactly, while dynamical balances (the thermal wind and linear vorticity balances) are included as soft constraints. The other soft constraints penalize smoothness of the model field and deviations from the data. The model solves for horizontal velocity, surface heat fluxes and parameters defining the horizontal and vertical diffusivities. Its horizontal resolution varies between  $2.5$ - $10^\circ$ , and the dimension of the system of equations characterizing the traces budgets reaches several thousand. The data include

a set of more than 9000 stations collected over different data sets and cover the area of Atlantic ocean.

## 2.6 GCM-based inverse models

Prognostic ocean general circulation models (GCMs) have been intensively developed over the past two decades and are now able to reproduce basic large-scale circulation features of the velocity field, temperature and salinity representative of today's climate state. However, they are still not able to reproduce details and could exhibit trends in long-term runs deviating from the observational data. Generally, there are two reasons for that. First, the physical laws which describe the large scale ocean circulation are highly nonlinear, and part of physical processes is parameterized instead of being resolved, which is partly responsible for model deficiencies. Second, the complex topography of the ocean bottom demands high resolution of the model domain that might often go beyond the computational abilities.

Given these considerations, there are several objectives of assimilating data into prognostic models. First, it is using the data in order to improve the ocean model parameterizations of subgrid processes, boundary conditions etc. The second objective is to reproduce the four dimensional picture of the ocean flow (that is spatial distribution plus time evolution) which is consistent with the observations and with the dynamical equations. Finally, the third objective is to provide initial conditions for the forecasting of the ocean circulation. This challenging set of objectives is pursued by Wenzel et al. (2001) and a series of papers from the ECCO consortium Stammer et al. (2002) and Stammer et al. (2003) that suggest the view on the global ocean circulation.

More modest objective is finding a 3D picture of the stationary ocean circulation that would correspond to a compromise between an ocean general circulation model and a given set of data within a least-squares framework. In most cases, the representative data sets assume some averaging which in turn suggests obtaining a quasi-stationary picture of the circulation. This objective served as motivation for most of the early applications and here we mention the works by Tziperman et al. (1992a), Tziperman et al. (1992b), Marotzke and Wunsch (1993), Schiller and Willebrand (1995), Schiller (1995), Yu and Malanotte-Rizzoli (1996). On the practical side, all they deal with estimating the circulation in the North Atlantic.

Since the IFEOM presented in chapters 4, 5 follows the same ideology we will review these works in some detail.

One of the first implementations of stationary inverse models was done by Tziperman et al. (1992a) where they tested a general circulation model (GCM) based on simplified momentum equations in several experiments in order to examine the feasibility of solving inverse problem, constructing adjoint to GCMs and to understand how the optimization uses various data to calculate model

parameters desired. In the general case, their cost function penalized the deviation of the model solution from the steady state (time derivatives in the equations for the potential temperature and salinity) together with deviation of temperature, salinity, air-sea fluxes of heat and fresh water and the wind stress from their observed values. The simplified momentum equations neglect the time derivative and momentum advection, parameterize viscous forces via the Rayleigh friction, and consider the wind stress as a "body force" which is different from zero only within the first model layer. The computational mesh consist of 3000 3D nodes, which sets the largest number of unknowns to approximately 7000. Tziperman et al. (1992a) carry a set of experiments with different combinations of data (they use a synthetic set produced in a forward run of their model), constraints and control parameters. They pay attention to the fact that generally the inverse problem is ill conditioned yet a solution for optimal hydrography to improve the possibly noisy hydrography data is feasible. Some particular problem like determining surface momentum fluxes by known hydrography could be very difficult to solve (which corresponds to a large number of iterations in the minimization algorithm) without information on surface velocity. Determining surface heat and freshwater fluxes is accurate but problems arise when noise is added to the hydrography.

This work was followed by another paper by (Tziperman et al., 1992b) which estimates the steady state circulation in the North Atlantic using  $2^\circ \times 3^\circ$  resolution grid which amounts to about 30000 unknowns. The paper points onto two difficulties — the existence of local minima of the cost function preventing the convergence of the optimization and ill conditioning of the inverse problem manifested in the cost function being flat in some directions. Both they partly linked to enforcing steadiness of the model temperature equations. Tziperman et al. (1992b) examine the conditioning of steady penalties based on one-step approach or on longer integration and suggest to penalize the sum of squares of the differences between the initial temperature and the temperature at several different times between the initial and final state (within a period of one to two years).

The model by Marotzke and Wunsch (1993) further develops the work by Tziperman et al. (1992a) and Tziperman et al. (1992b), and uses the momentum equation simplified in the same way (except for omission of wind forcing). Its grid covers the North Atlantic from  $9.5^\circ$  to  $59.5^\circ\text{N}$  and has resolution of  $1^\circ$  zonally and  $2^\circ$  meridionally. The objective function penalizes the model – data misfit and enforces stationarity by penalizing the squared difference between the model initial and final state. By using finite integration time it partly overcomes the problem of enforcing steadiness discussed by Tziperman et al. (1992a) and Tziperman et al. (1992b). The momentum, continuity and tracer equations on each time step are included into the Lagrangian via Lagrange multipliers. The model seeks for the initial state and surface forcing in tracer equations that make the Lagrangian stationary. The standard experiment begins from a 250 day forward run (initialized by observed hydrology)

which is followed by 15 conjugate gradient steps of the minimization algorithm each comprising runs of the forward and adjoint model over 100 days. Then the integration time is increased to 500 days and 21 additional steps are performed. The model solution shows an overturning cell with maximum of about 20 Sv strongly displaced to the northern wall of the domain. The optimized surface temperature and salinity are rather noisy compared to climatology, yet the residuals in the steadiness constraint are reasonably small. The initial step of 250 day integration is essential. Without it, the model converges to a solution which corresponds to an overturning cell of only 6 Sv. This shows sensitivity to the initialization and indicates once again that difficulties mentioned by Tziperman et al. (1992a) and Tziperman et al. (1992b) are not fully eliminated.

The models by Schiller and Willebrand (1995) and Yu and Malanotte-Rizzoli (1996) are similar to that used by Marotzke and Wunsch (1993). Schiller and Willebrand (1995) use full momentum equations and a simplified adjoint model in which the adjoint equations are only solved for tracers. The paper by Yu and Malanotte-Rizzoli (1996) makes one step further and uses the full adjoint model. Schiller (1995) presents a solution obtained with the model by Schiller and Willebrand (1995) by inverting Levitus 1982 climatology and hydrographic section data in the Atlantic Ocean. Experiments were started from observed temperature and salinity interpolated on the model grid, or Levitus 1982 data if observation data are lacking. The initial integration time is one year and as efficiency of minimization drops down, it is increased to 5 years. A total integration time is between 10 and 20 years. The model has horizontal resolution of  $2^\circ$  degrees in both horizontal directions, and only 12 vertical layers. Its solution gives a meridional overturning cell with maximum values between 16 and 23 Sv (depending on experiments).

The mesh of the model by Yu and Malanotte-Rizzoli (1996) covers the same area as in work by Marotzke and Wunsch (1993). Similarly, the guess values for the ocean state are taken from a 250-day spin up of the forward model. The integration time in the minimization phase is 180 days initially and increases to 250 and to 500 days if insufficient reduction in the cost value occurs. The data is Levitus 1982 climatology and climatology compiled by Fukumori and Wunsch (1991). The solutions show, however, systematic errors in the vertical — cooling of the upper ocean and warming in the deep ocean attributed by the authors to the steadiness assumption.

This problem was cured (see Yu and Malanotte-Rizzoli (1998)) by constraining the model additionally to monthly mean climatology of (Levitus et al., 1994; Levitus and Boyer, 1994) and using the wind stress forcing from Hellerman and Rosenstein (1983). The set of independent model parameters was augmented by including mixing coefficients. Since the difference between the first and 13th months of integration is penalized, the approach of Yu and Malanotte-Rizzoli (1998) is intermediate between the models attempting ‘steady’ inversion and real 4D VAR models mentioned at the beginning of this

section

An application of 4D VAR model to the global ocean is given in the work by Wenzel et al. (2001). The model is run on  $3.5^\circ$  resolution which makes possible using large number of iterations in order to approach the optimal solution and therefore getting closer to the optimal state compared to other models of higher resolution by Stammer et al. (2002, 2003).

An extensive use of a 4D VAR model is given in the work by Stammer et al. (2002) where they estimated the global ocean circulation for the period from 1992 to 1997 on  $2^\circ \times 2^\circ$  resolution. Data include monthly mean climatological fields, surface heat and freshwater fluxes, wind stress fields, altimetry anomalies and a geoid model.

The recent study of Stammer et al. (2003) uses  $1^\circ \times 1^\circ$  resolution and focuses on transports in the world ocean obtained by assimilating WOCE data.

In summary, most models imposing the steadiness constraint use time stepping and in this respect are very close to real 4D VAR models. Correspondingly, they could be rather expensive in terms of CPU time if run on grids of comparable resolution. The IFEOM described further in this thesis follows the ideology of Tziperman et al. (1992a) and Tziperman et al. (1992b). Its single iteration is cheap, however in problems of large size the number of iterations required to reach the convergence could be large (the inversions for the North Atlantic reported in chapter 5 are performed for 220,000 unknowns which is an order of magnitude more than in other models enforcing steadiness, it requires 5000 iterations to reach the steady solution). IFEOM overcomes the problems caused by enforcing steadiness by introducing some additional constraint explained in chapter 4.

## 2.7 Principles of Finite Elements method

Two model presented in the following chapters use the finite-element method (see, for example, Johnson (1990); Zienkiewicz and Taylor (2000a,b,c)) to discretize the model equations. It is not common in the ocean modeling community, and this section briefly introduces it. The principles of finite element technique could be easily explained using an example of a boundary value problem for the Poisson equation

$$\mathcal{A}u = f \quad \text{in} \quad \Omega, \quad (2.12)$$

where

$$\mathcal{A}u = \Delta u := \frac{\partial^2 u}{\partial x^2} + \frac{\partial^2 u}{\partial y^2}, \quad (2.13)$$

$f$  is a given function on  $\Omega$ , and  $u$  satisfies boundary conditions of von Neumann or Dirichlet types on the boundary  $\partial\Omega$ .

The ideology of finite elements assumes the following main steps:

1. Weak formulation of the given problem and transformation of the equations (if needed) to reduce the order of differential operators
2. Partitioning of the domain  $\Omega$  into elements and formulation of the weak equations on a finite dimensional subspace  $V_h$
3. Solving the problem

Let us begin with projecting (2.12) on a function  $\phi$  from some functional space  $\Phi$  such that projection is defined:

$$\int_{\Omega} \phi \mathcal{A}u d\Omega := (\phi, \mathcal{A}u) = \int_{\Omega} \phi f d\Omega, \quad (2.14)$$

The weak formulation is: Find  $u$  satisfying boundary conditions such that (2.14) holds for any  $\phi$  from  $\Phi$ . At this stage, the operator part could be integrated by parts to reduce the order of the differential operator acting on  $u$ :

$$\int_{\Omega} \nabla \phi \nabla u d\Omega = \int_{\partial\Omega} \phi \frac{\partial u}{\partial n} d\gamma - \int_{\Omega} f \phi d\Omega, \quad \forall \phi \quad \text{from} \quad \Phi \quad (2.15)$$

If the boundary condition is of Neumann type, it sets the boundary integral on the RHS of (2.15). For a Dirichlet boundary condition, the surface integral will be irrelevant as is demonstrated below.

Notice that (2.15) includes only first order derivatives of functions  $u$  and  $\phi$  so it could be solved for square integrable together with their derivatives functions  $u$  and  $\phi$ . This is illustrated below for the space of piece wise linear functions.

Let us make the triangulation of  $\Omega$  by the set of non-overlapping triangles  $T = \{T_i\}, i = 1, \dots, K$  like it is shown in Fig. 2.5. Let the subspace  $V_h$  be defined as the space of piece wise linear functions on  $T$ . The basis of  $V_h$  can be chosen as the set of linear within each triangle functions  $\phi_i, i = 1, \dots, N$  which take 1 at one node and 0 at other nodes (Fig. 2.5).

Using the basis functions  $\phi_i$ , one expands the unknown field  $u$  as

$$u = \sum_{i=1}^N u_i \phi_i. \quad (2.16)$$

Here,  $u_i$  is the magnitude of  $u$  at node  $i$ . The discretization (2.16) is continuous in  $\Omega$ , which should be compared to the case of finite differences where discrete values are defined only at nodes.

On substituting (2.16) into (2.15), the next step is to require (2.15) to hold true for  $\phi$  being any of  $\phi_i$ . This is the Galerkin procedure which ensures minimum of the norm of the residual. This results in the system of Galerkin's equations

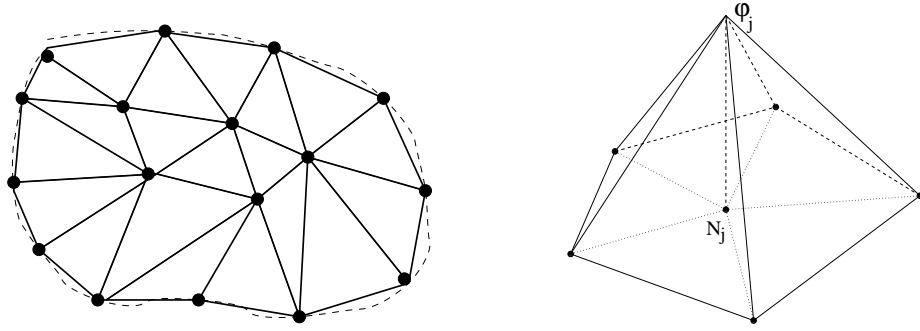


Figure 2.5: Triangulation of the domain  $\Omega$  (left panel). The dashed line shows the real boundary of  $\Omega$ . On the right panel the piece wise linear basis function  $\phi_j$  is shown. It gets 1 at node  $N_j$  and 0 at other nodes.

$$\left( \int_{\Omega} \sum_{j=1}^N \nabla \phi_i \nabla \phi_j d\Omega \right) u_j = \int_{\partial\Omega} \sum_{j=1}^N \phi_i q_j \phi_j d\gamma - \int_{\Omega} \sum_{j=1}^N f_j \phi_i \phi_j d\Omega, \quad i = 1, \dots, N, \quad (2.17)$$

where  $f_i$  and  $q_i$  are the nodal values of the given function  $f$  and normal derivative of  $u$  in the case of von Neumann boundary conditions. It could be rewritten in the matrix form

$$S_{ji} u_i = r_j,$$

where  $r_i$  is the full vector of RHS, and  $\mathbf{S}$  is the stiffness matrix whose elements are the expression in parentheses on the LHS of (2.17). If a Dirichlet boundary condition is imposed at a node  $k$  that belongs to the boundary of  $\Omega$ ,  $u_k = u_k^D$ , one sets  $S_{kj} = \delta_{kj}$  and  $r_k = u_k^D$ . This makes computing the contribution from the surface integral at such nodes unnecessary.

The last step is solving the system of equation written above. Iterative solvers are typically used for this purpose if the size of the problem is large (depends on the memory available). The stiffness matrix is usually sparse and is therefore assembled and stored in a sparse format.

The main advantages of finite element method as applied to ocean modeling could be summarized as follows.

1. Finite elements allow flexible computational grids. Concerning the ocean modeling it allows representation of the coastlines and bottom topography in a smooth way as opposite to finite difference method which suggest only stepwise representation.
2. Finite elements give the continuous representation of the solution to the model equations thereby allowing computing the model variables at the data locations without interpolation. Additionally, due to the flexibility in partitioning of the model domain, the data locations can be included

into the discretization by putting computational nodes at observational points.

3. Finite elements treat the boundary conditions of von Neumann type (which describe the ocean exchange with the atmosphere) in a natural way through the boundary integrals.

## Chapter 3

# Finite Element Inverse Section Model (FEMSECT)

Section models that are based on thermal wind balance are intensively used by oceanographers to estimate geostrophic transports through sections. The main motivation here is their simple structure and ease of use. If current meter data are available in addition to hydrography data the reference level velocity could be estimated thus making transport estimates much more reliable.

This chapter presents a new section model called FEMSECT that combines hydrography and current meter data in least squares sense to produce estimate of transports through the section. Its novel feature is using finite element method for discretization.

Recently, finite element methods (FEM) have received considerable attention in oceanography, because the triangular discretization that is typical to FEM allows the good resolution of irregular domains at comparatively low cost. The flexible discretization with triangles is attractive for a hydrographic section because the triangles naturally take care of smooth representation of bottom topography, where conventional finite difference methods are ambiguous (e.g., Wunsch, 1996). The second advantage stems from the explicitly defined interpolation rules that allow to map model variables naturally to the data locations, thus making the modeling system highly consistent. This is the consequence of the variables in FEM being not only defined at discrete grid nodes, but continuously over the whole domain by so-called basis functions (see section 2.7). Applications of finite elements in oceanography include regional studies (Dobrindt and Schröter, 2003; Myers, 1995; Myers et al., 2004), tidal models, both regional (Walters, 1987) and global (Le Provost et al., 1998), and recently even general circulation models (Nechaev et al., 2003, 2004; Danilov et al., 2004a,b).

Here, we will demonstrate, how an inverse section model that is based on the finite element method, can help to interpret current measurements in conjunction with hydrographic data. The model is described in Section 3.1; Section 3.2 discusses advantages and disadvantages of the finite element method.

Section 3.3 shows the performance of FEMSECT on a test example and its comparison with standard dynamical methods. Section 3.4 demonstrates in a realistic application the capabilities of the model and conclusions are drawn in Section 3.5.

The FEMSECT was developed together by M. Losch and the author of this thesis; application to the Fram Strait transport estimates and analysis were done by A. Beszczynska-Müller. The extended version of the material presented here is the subject of a paper in preparation (Losch et al., 2004).

### 3.1 Model Construction

The model uses the equation of state to determine the density and the thermal wind relation to determine the vertical shear of horizontal velocity across the section. The independent model variables are the hydrography ( $T$  and  $S$ ) and reference velocities to some depth. The cost function includes the deviation of independent model parameters from the data. At this point the advantage of finite elements is that the model variables are continuously represented and are given at the data locations. Besides that the model grid can be irregular and the data locations may be included into the discretization if needed.

We define the cost function as the following:

$$\begin{aligned} \mathcal{J} = & \frac{1}{2} (\mathbf{T}^* - \Phi_T \mathbf{T})^T \mathbf{W}_T (\mathbf{T}^* - \Phi_T \mathbf{T}) \\ & + \frac{1}{2} (\mathbf{S}^* - \Phi_S \mathbf{S})^T \mathbf{W}_S (\mathbf{S}^* - \Phi_S \mathbf{S}) \\ & + \frac{1}{2} (\mathbf{v}^* - \Phi_v \mathbf{v})^T \mathbf{W}_v (\mathbf{v}^* - \Phi_v \mathbf{v}) \\ & + \mathcal{R}. \end{aligned} \quad (3.1)$$

Here the matrixes  $\Phi_T$ ,  $\Phi_S$  and  $\Phi_v$  represent the projections of model vectors of temperature, salinity and velocities through the section denoted by  $\mathbf{T}$ ,  $\mathbf{S}$ , and  $\mathbf{v}$ , respectively, onto the locations of their actual measurements. Variables marked with stars represent the vectors of data.  $\mathbf{W}_T$ ,  $\mathbf{W}_S$  and  $\mathbf{W}_v$  are some positive definite weights which should be defined as the inverses of prior error covariances. The last term  $\mathcal{R}$  in the cost function represents the regularization,

$$\mathcal{R} = \frac{1}{2} \mathbf{v}_{ref}^T \mathbf{W}_{v_{ref}} \mathbf{v}_{ref} + \frac{1}{2} \mathbf{v}_x^T \mathbf{W}_r \mathbf{v}_x. \quad (3.2)$$

It is introduced to penalize the big values of the reference velocities  $\mathbf{v}_{ref}$  and to constrain the horizontal component of the velocity gradient  $\mathbf{v}_x$ .

The BFGS quasi-Newton algorithm (Nocedal, 1980; Gilbert and Lemaréchal, 1989; Liu and Nocedal, 1989) is used to find the minimum of the cost function. The implementation of this method in MATLAB routine was done by Kelley (1999). As input parameters this algorithm needs the value of the cost function and its gradient with respect to control variables.

At the end of the minimization we compute the Hessian matrix of second derivatives of  $\mathcal{J}$  which represents the inverse of error covariance matrix (Thacker, 1989). From the inverse Hessian we further compute error covariance which gives us the error bars of our model result.

## 3.2 Discretization of the Model Equations

In order to derive finite element formulation of the thermal wind equations we discretize the model domain with the triangular elements. It is done using Delaunay triangulation which is implemented in MATLAB (Barber et al., 1996). Fig. 3.1 shows the result of the triangulation for the section across the Fram Strait in the Arctic Ocean. The nodes of the grid represent the positions of CTD measurements (Fahrbach et al., 2001; Schauer et al., 2004).

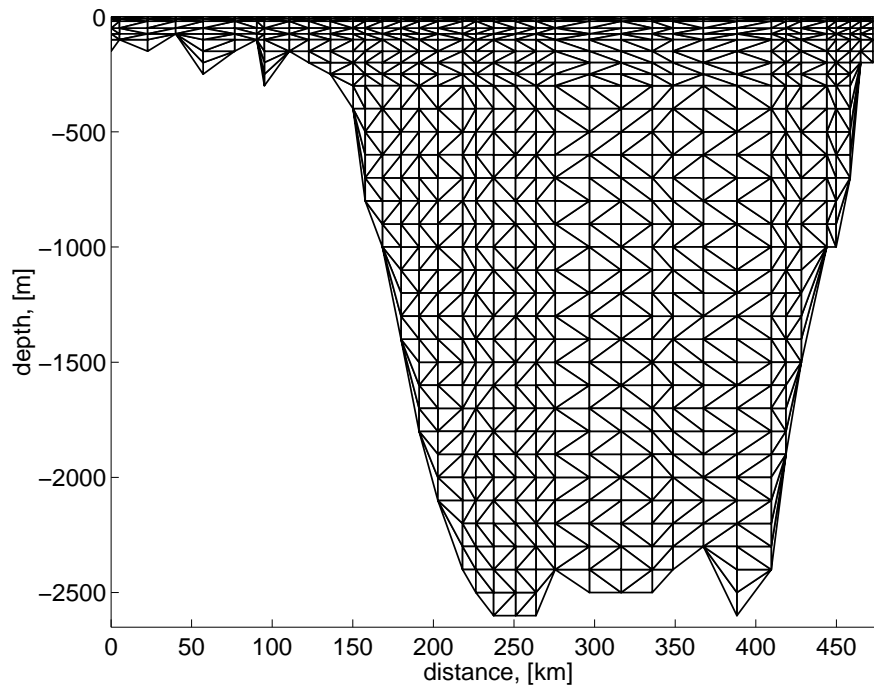


Figure 3.1: Finite Element grid produced by Delaunay triangulation method (Barber et al., 1996) for the section across Fram Strait at approximately  $79^\circ\text{N}$ . The grid nodes represent the positions of the CTD measurements (Fahrbach et al., 2001; Schauer et al., 2004).

### Piece wise linear representation of the velocity

We project the solution of thermal wind relation onto the space of piece wise linear basis functions (see 2.7). With the use of Galerkin's method described

in section 2.7 the thermal wind relation reads as follows

$$\sum_{i=1}^N v_i(\phi_j, \frac{\partial \phi_i}{\partial z}) = -\frac{g}{\rho_0 f} \sum_{i=1}^N \rho_i(\phi_j, \frac{\partial \phi_i}{\partial x}), \quad j = 1, \dots, N. \quad (3.3)$$

Here  $v_i$  and  $\rho_i$  are the values of the velocity through the section and of the density field at the grid nodes,  $\phi_i$  is the piece wise linear basis function which takes 1 at node  $i$ , 0 at neighboring nodes, and is zero outside the cluster of triangles having common node  $i$  (see section 2.7),  $j = 1, \dots, N$  and  $N$  is the number of grid nodes.

Equation (3.3) must hold for any  $\phi_j$ ,  $j = 1, \dots, N$ . Using the matrix notation the set of Galerkin's equations can be rewritten as follows

$$\mathbf{U}\mathbf{v} = \mathbf{R}\boldsymbol{\rho}, \text{ or } \mathbf{v} = \mathbf{U}^{-1}\mathbf{R}\boldsymbol{\rho}, \quad (3.4)$$

where

$$U_{ji} = (\phi_j, \frac{\partial \phi_i}{\partial z}) \quad (3.5)$$

$$R_{ji} = -\frac{g}{\rho_0 f} (\phi_j, \frac{\partial \phi_i}{\partial x}). \quad (3.6)$$

The Dirichlet boundary condition is implemented in the strong form. That is the rows of matrix  $\mathbf{U}$  which correspond to the boundary nodes are replaced with 1 on diagonal elements and zeros everywhere else and the corresponding elements in the right hand side are replaced with the boundary values.

We tested this approach to diagnose the velocity field through the section across Fram Strait (Fig. 3.1) given the temperature and salinity at the grid nodes and using the assumption of the level of no motion at the bottom. The result was surprising. Figure (3.2) shows the zero contour intervals of the velocity field which correspond to the result of this diagnostic. The finite element solution appears to be noisy. The averaging of the values on two triangles which form a rectangular removes this noise (Fig. 3.2). In finite elements, all of the nodes which belong to the stencil of a particular grid point contribute to the derivative at this grid point. Consequently, the inverse of a finite element operator distributes information to all nodes of the stencil. If the operator is elliptic, the norm of the gradient is bounded (see, e.g., Johnson, 1990, page 24). But our problem is not elliptic and the norm of the gradient of the velocity field is unconstrained. As the result the inversion of the finite element operator in (3.4) leads to a numerical mode which is visible as noise in the left hand panel of Figure 3.2. This noise, however, has zero mean on each cluster (computational stencil) of elements. In addition, the finite element operator corresponding to the first order differential problem has zeros on the diagonal and iterative solvers are very inefficient in doing it.

Hence, the integral properties of the solution, for example, the total volume transport through the section as it is shown below, are not affected by the noise

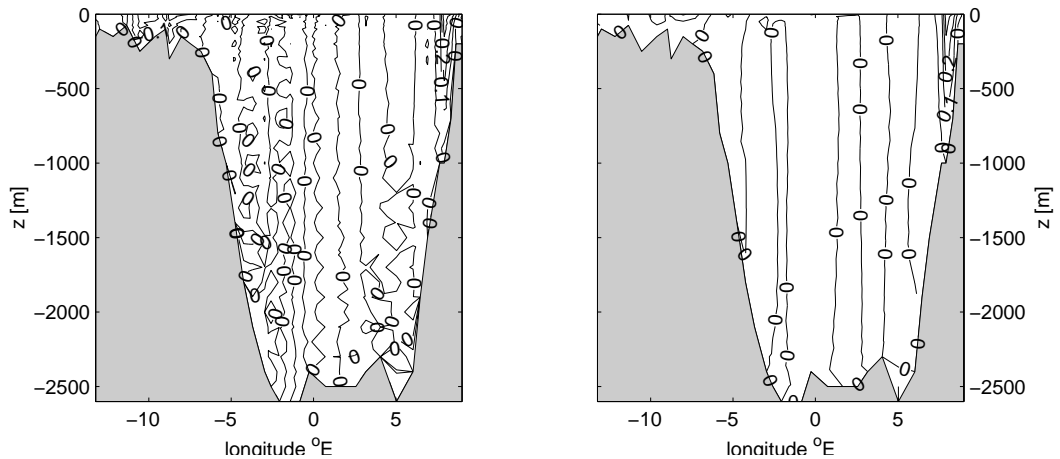


Figure 3.2: Thermal wind in Fram Strait with respect to vanishing velocity at the bottom of the domain. Only the zero-contour is drawn. Left hand figure: The finite element solution with piece wise linear basis functions is noisy. Right hand figure: The values on two triangles that form a rectangle have been averaged to remove the spurious degree of freedom of the finite element solution. After Losch et al. (2004).

in the velocity field. In fact, the integral formulation of the finite element method ensures, that conservation laws are satisfied exactly in the numerical realization of the equations.

### Piece wise constant representation of the velocity

In order to remove the degree of freedom in the finite element solution we modify the Galerkin's equations. First of all we formulate the thermal wind relations in the form of potential. That is we modify equations and seek for a finite element solution to a second order problem. This can be easily done by replacing  $u$  with a potential  $V$  such that

$$v = \frac{\partial V}{\partial z}. \quad (3.7)$$

The Galerkin's equation for the potential formulation will be modified as follows

$$\sum_{i=1}^N V_i \left( \frac{\partial \phi_j}{\partial z}, \frac{\partial \phi_i}{\partial z} \right) - \sum_{i=1}^N v_i \int_{\partial\Omega} \phi_j \phi_i n_z d\gamma = \frac{g}{\rho_0 f} \sum_{i=1}^N \rho_i \left( \phi_j, \frac{\partial \phi_i}{\partial x} \right), \quad (3.8)$$

where the boundary integral is taken along the boundaries at the surface and at the bottom of the domain,  $n_z$  is the  $z$  component of the normal to the boundary and  $V_i$  are the values of the potential  $V$  at the grid nodes. As it was the case for the linear basis functions the relation (3.8) must hold for all

$\phi_j$ ,  $j = 1, \dots, N$ . The resulting second order problem for the new unknown variable  $V$  requires two boundary conditions: one is the reference velocity and the other is an arbitrary constant that does not affect the velocity  $v$ . The piecewise constant velocity can be recovered from the potential using 3.7

### 3.3 Testing the Discretized Thermal Wind Equations in Idealized Geometry: Triangular Domain

In a first test of the finite element discretization, we compute velocities from thermal wind relative to the bottom through an idealized domain: a triangle (Figure 3.3). We assume a density field that is a linear function of the horizontal coordinate and constant with depth ( $\rho = \rho_0 + ax$ ), so that we can integrate thermal wind equation analytically. For our choice of density and a domain that is 3800 km wide and has a maximum depth of 3800 m, we obtain a transport of  $-2.4$  Sv.

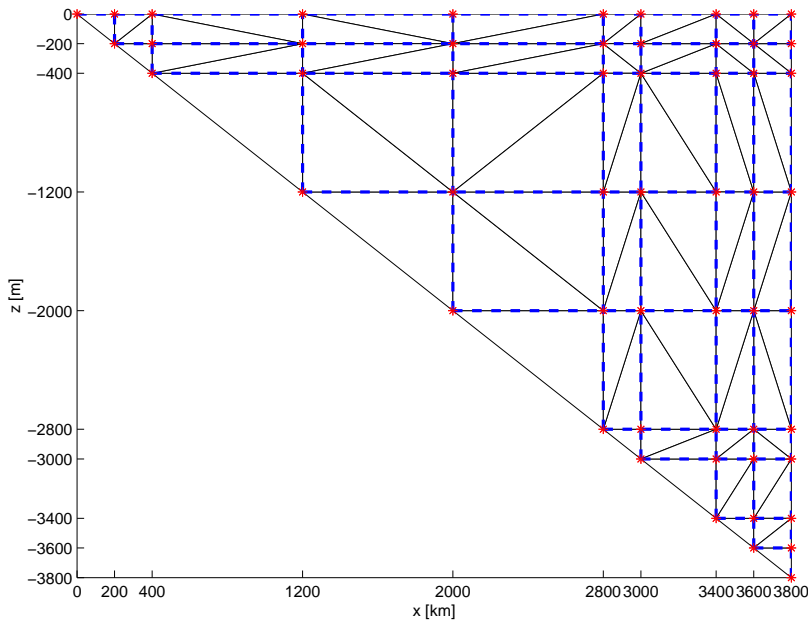


Figure 3.3: Triangular domain with hypothetical measurement points (stars). Solid thin lines mark the finite element triangular grid, the thick dashed lines correspond to the finite difference grid of the dynamic method. After Losch et al. (2004)

A standard dynamical method, for example, as implemented in the MATLAB routines of the CSIRO sea water library (Morgan, 1994), computes geopotential height anomalies at the location of vertical casts of temperature and salinity. Velocities are then calculated between station pairs and therefore,

the method is accurate to first order. Without special treatment of bottom triangles the dynamic method gives a transport of  $-2.33$  Sv.

Our finite element discretization is based on piece-wise linear basis functions for density (or temperature and salinity) and either piece-wise linear or constant basis functions for velocity. In both cases the computed transport is exactly that of the analytical integration. Only because the density field was chosen to vary linearly between stations, its approximation by piece-wise linear basis functions gives a perfect result.

Therefore, we now assume a density field that is a quadratic function of the horizontal coordinate, but still constant with depth:  $\rho = \rho_0 + bx^2$ . In this case, the exact transport is  $-3.6$  Sv. The dynamic method deviates by  $0.1$  Sv, the finite element method with piece-wise linear basis function for velocity by  $-0.02$  Sv, and for piece-wise constant basis functions for velocity we get a results that is  $0.03$  Sv bigger than the exact transport. We note, that also in the case of a non-linearly varying density field the finite element methods are more accurate than the dynamic method by almost one order of magnitude.

### 3.4 A First Application: Fram Strait

Fram Strait is the only deep passage between the Arctic Ocean and Nordic Seas. The variability of oceanic fluxes through Fram Strait has been monitored by an array of moorings since 1997 (Fahrback et al., 2001; Schauer et al., 2004). There were basically 14 moorings from 1997 to 1999 covering the section from the eastern Greenland shelf break to the western shelf break off the coast of Spitsbergen. For the period from 1999 to 2000, 3 of these moorings in the central part of the strait were not deployed. In 2002 the array was augmented with two additional moorings in the recirculation area and one mooring at the Greenland shelf. Each year during the redeployment of the array in summer or autumn, hydrographic measurements at CTD stations along the mooring line were carried out with high spatial resolution.

Time series of temperature and velocity from moored instruments provide estimates of heat and volume fluxes with excellent temporal resolution but the spatial structure of the flow is underresolved. This is the main source of uncertainties in the measured transport. With our new finite element section inverse model FEMSECT we can overcome this problem and obtain better transport estimates by combining different types of data.

Below we discuss result obtained by applying the FEMSECT to estimate the transport across Fram Strait using the data from the mooring array and high spatial resolution CTD stations placed along the mooring line.

Figure 3.4 presents results of two reconstructions based on the full data set of August 2002. It plots the velocity field resulted from FEMSECT inverse (lower panel) and from interpolation of current measurements (upper panel). Both show an intensive northward flow of the West Spitsbergen Current. The

FEMSECT velocity field shows an additional shear at the lower boundary of the Atlantic water layer. On the opposite side of Fram Strait, we see the southern flow with a core over the Greenland shelf slope. It is caused by the strong density gradient in the upper layer and is much better reproduced by the FEMSECT inverse than by interpolated mooring data. FEMSECT result suggests that Atlantic water recirculates in the central Fram Strait with smaller spatial scales than the one produced by mooring array. Estimates of

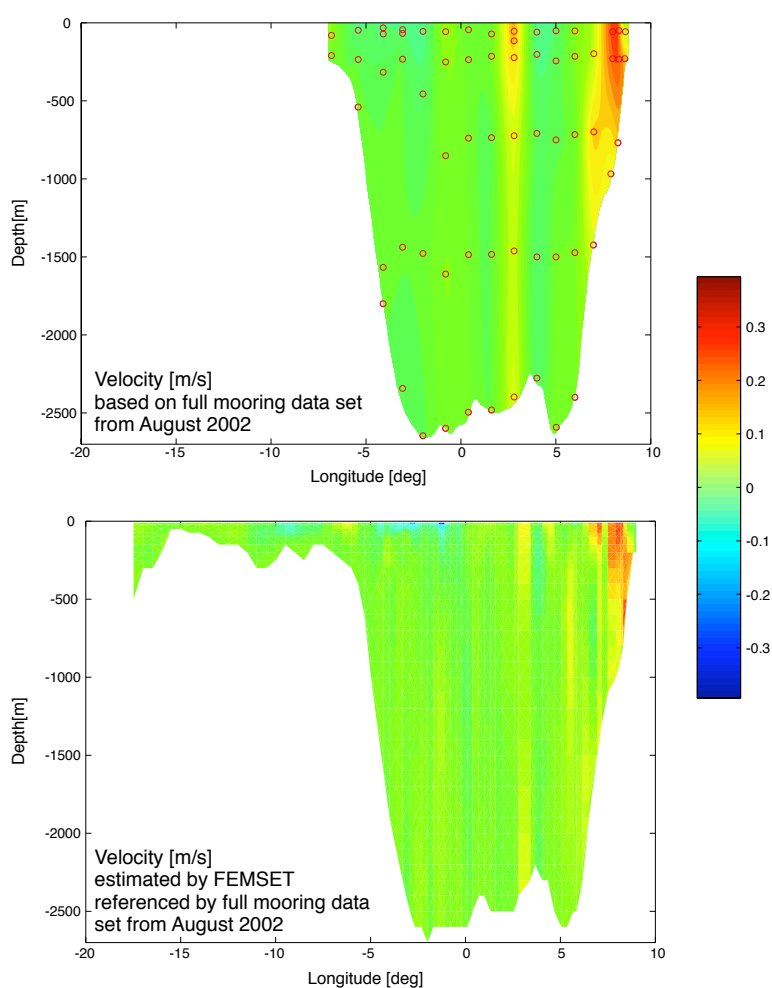


Figure 3.4: Velocity fields from interpolation of current measurements (upper panel) and from the FEMSECT inverse (lower panel). Positions of moorings are marked by circles. After Losch et al. (2004)

volume and heat transports through Fram Strait for period 1997-2002 from the mooring data and the FEMSECT solution which combines mooring data and CTD measurements are shown of Figure 3.5.

Almost all FEMSECT results give a northward net volume transport. Other

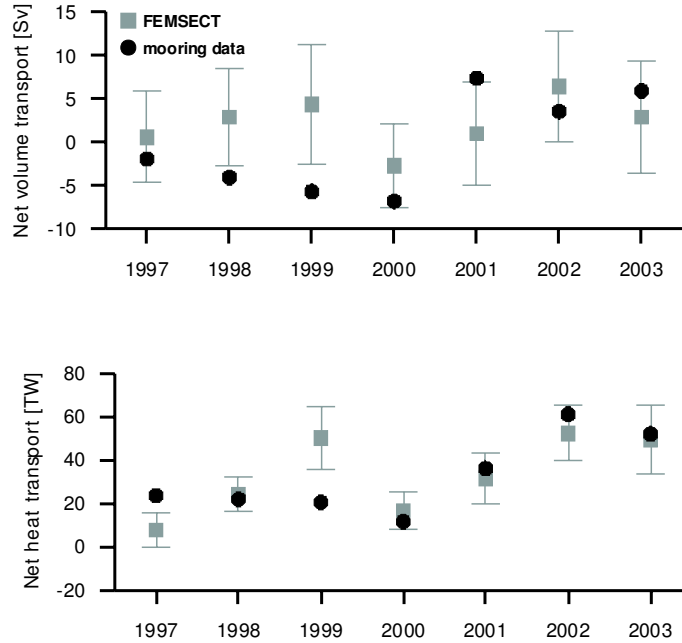


Figure 3.5: Time series of volume and heat transports through Fram Strait. Errorbars are plotted for the FEMSECT result. After Losch et al. (2004)

estimates by inverse models (Rudels et al., 1999; Schlichtholz and Houssais, 1999) suggest net southward flow through Fram Strait. However, their models assume there is no flow in the deep layers. This can apparently be the reason of disagreement between their and our results.

The biggest difference in net transports estimated from mooring data and FEMSECT between 1997 and 2001 comes from the gap in mooring array in the central part of the Fram Strait. In 1997-2000, at the both sides of the gap a dominating southward flow was registered. The interpolation between two sides of the gap resulted in enormous southward net transport. In 2001, the northward flow was registered by the mooring at the edge of the gap and interpolation over the gap resulted in the strongly overestimated northward volume transport which also led to the net transport to the north. Addition of two moorings in the recirculation area in 2002 and 2003 allowed much better representation of the central Fram Strait to be obtained and led to improved agreement between the transport estimates based on the mooring array and FEMSECT inverse model. One can that assume that FEMSECT being constrained by CTD data "fills" the gap in the moorings data in some consistent way.

Most estimates of net heat transport from moorings fit within the error range (obtained from the directly computed Hessian matrix of second derivatives of  $\mathcal{J}$ ) of FEMSECT estimates (Fig.3.5).

To investigate how does the spatial resolution of measured velocities influ-

ence the estimation of velocity field and volume and heat transport we made two numerical experiments. To initialize the experiments we choose two data sets from August 2002 and September 2003 with increased spatial coverage by moorings in the central Fram Strait. Next we compute the velocity fields from interpolation of the moored instruments data and FEMSECT inversion twice. First we compute it for full data sets and next for data sets with removed two central moorings.

Differences in velocity fields estimated with “full” and “gappy” mooring data are shown in Fig. 3.6 for August 2002. Table 3.1 shows values of volume and heat transports, estimated for these experiments.

The results computed by interpolating the mooring data with two central moorings removed show a strong increase in the northward net volume transport: it increases by a factor of 3 in 2002 and by factor 2 in 2003, compared to full mooring data interpolation.

At the same time, difference between net volume transport estimates by FEMSECT, based on a “full” and “gappy” set of referencing velocities were respectively 0.5 Sv and 0.3 Sv for 2002 and 2003 what makes less than 10% in both cases. Differences in estimated heat transports are also of an order of magnitude bigger in case of estimates based on mooring data alone as compared to FEMSECT results.

Experiment	Volume net [Sv]	Heat net [TW]
Moorings Sept. 2003	5.9	52.1
Moorings Sept. 2003 with gap	12.2	56.6
FEMSECT Sept. 2003	2.9	49.7
FEMSECT Sept. 2003 with gap	3.2	48.5
Moorings Aug. 2002	3.6	61.2
Moorings Aug. 2002 with gap	15.5	70.4
FEMSECT Aug. 2002	6.4	52.4
FEMSECT Aug. 2002 with gap	6.9	52.5

Table 3.1: Volume and heat transport estimates. After Losch et al. (2004)

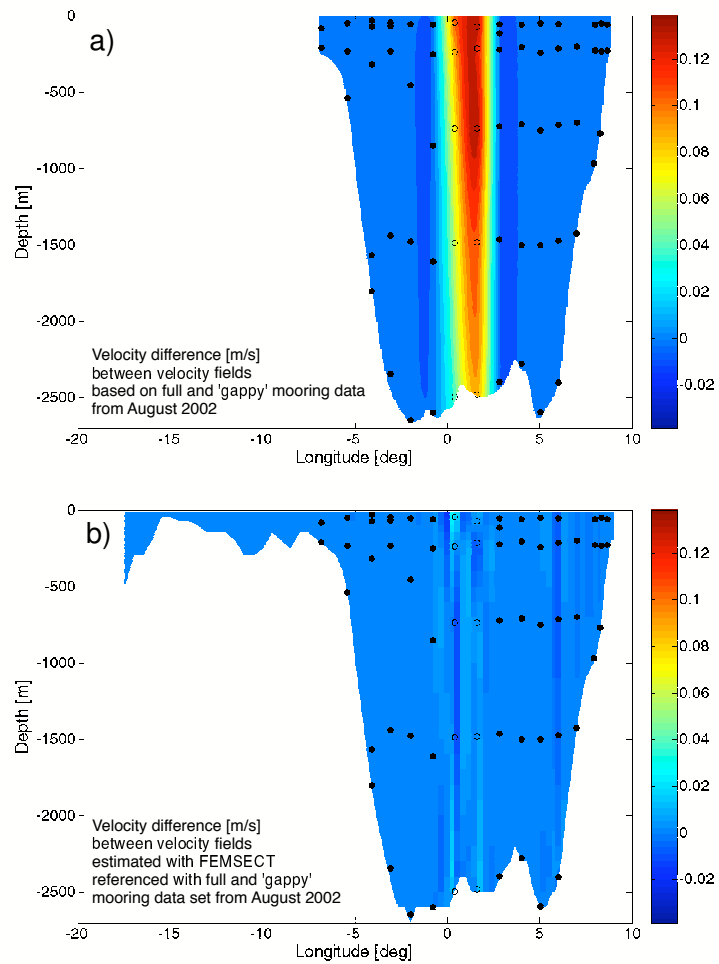


Figure 3.6: Differences in velocity fields estimated with “full” and “gappy” mooring data. The upper panel corresponds to the estimates from mooring data alone, and the lower panel represents the difference between the two FEMSECT results. After Losch et al. (2004)

## 3.5 Conclusion

Application of FEMSECT to the Fram Strait transports estimates demonstrates that inverse methods and finite elements are a perfect combination for analyzing irregularly spaced section data in oceanography. With the help of inverse methods, data of different type and resolution can be combined with dynamical balances to yield a best fit between all available data that is dynamically consistent. Finite elements provide an elegant way to account for irregularly spaced data with a triangular grid. Also, the finite element method requires the numerical formulation of the dynamical equations in matrix form, which in turn makes the formulation of the adjoint model trivial: the adjoint of a matrix operator is simply its transpose.

# Chapter 4

## Inverse Finite Element Ocean Model (IFEOM)

Obviously, the FEMSECT model described in the chapter 3 represents a too simplified approximation to the reality. It solves only for local estimates and that is why the next step of this thesis was chosen to develop a full 3D assimilation model.

The aim of this chapter is to describe the Inverse Finite Element ocean model (IFEOM) which is developed by the author and is based on the steady-state version of FEOM (Danilov et al., 2004a,b). The IFEOM includes two main building blocks — the reduced version of FEOM and its adjoint — which are presented in some detail below. The distinct feature of FEOM is the use of unstructured meshes and matrix form of main equations. Due to the flexibility of the unstructured mesh discretization, the model is able to resolve complicated ocean boundaries (coast and bottom) in an accurate manner and locate computational nodes exactly at data sites (which could be of importance when hydrographic sections are assimilated). The matrix form, in turn, facilitates constructing the adjoint model.

The IFEOM considers ocean density as a control parameter. It could be augmented by open boundary velocities and the surface forcing, however all experiments described in chapter 5 use only density as control. By adjusting the control parameters, we search for a compromise between the data (hydrography) and residuals in the stationary advection–diffusion equation for potential density, and also additional constraints that reflect our a priori knowledge of the ocean circulation. The steady velocity entering the advection–diffusion equation is computed by solving the steady state primitive equations. This is the main advantage of the IFEOM over section models and FEMSECT in particular, because the velocity field found in IFEOM satisfies the continuity constraint.

Clearly, by construction, the IFEOM belongs to variational models and has analogs (Nechaev et al., 2003, 2004). The new element here comes from the set of constraints employed and applications. These details will be given in

chapter 5.

## 4.1 Finite Element Ocean Model (FEOM)

This section describes a reduced version of three-dimensional (3D) Finite-Element Ocean circulation Model (FEOM) used as a component of the Inverse Finite Element Model (IFEOM). The full FEOM solves the primitive equations in the dynamical part and the advection-diffusion equations for temperature and salinity in the thermodynamical part, and is designed for investigating the large-scale ocean circulation on time scales from years to decades (Danilov et al., 2004a,b). We will be using the stationary dynamical part of the model which allows computing velocity and sea surface elevation from given temperature and salinity (or density). The advection of momentum is neglected as it should be small for time mean solutions. For brevity, we will call the version of FEOM used by us as the forward model.

The 3D mesh of FEOM is composed of tetrahedra. It is based on an unstructured two-dimensional surface mesh with variable resolution and is stratified in the vertical direction. The model represents horizontal velocity and tracers as linear fields on tetrahedra, and surface sea elevation is linear on surface triangles. The vertical velocity field is element-wise constant. An important ingredient of the model is the Galerkin least-squares stabilization that allows stationary inversion of temperature and salinity fields for velocity and sea surface elevation.

### 4.1.1 Model equations

The forward model proceeds in a standard way by first computing the baroclinic pressure anomaly from the known density field and then solving vertically integrated momentum equations under the vertically integrated continuity constraint. It next determines 3D horizontal velocities using sea surface height and finally computes vertical velocity from known horizontal velocities. The second and third steps require a stabilization. It is explained by Danilov et al. (2004a) and is equivalent to modifying original equation in such a way that they become much easier to solve with iterative solvers. For the momentum equations, the stabilization is approximately equivalent to multiplying them with  $(1 + \mathbf{k} \times)$ . Here  $\mathbf{k}$  is a unit vertical orth. The modification of the continuity equation is more essential and is loosely equivalent to adding the divergence of the momentum equation (multiplied with some coefficient). The equations below are written in their original, non-stabilized form, but in reality the forward model (as well as FEOM) solves stabilized equations. We are not touching stabilization here as our goal is only to explain the structure of our forward model.

The vertically integrated steady momentum equations are

$$-fV - A_l \Delta U + gH \partial_x \zeta + \frac{1}{\rho_0} \int_{-H}^0 \partial_x p dz = \tau_x \quad (4.1)$$

$$fU - A_l \Delta V + gH \partial_y \zeta + \frac{1}{\rho_0} \int_{-H}^0 \partial_y p dz = \tau_y \quad (4.2)$$

$$\partial_x U + \partial_y V = 0 \quad (4.3)$$

$$\partial_z p = -g\rho. \quad (4.4)$$

Here  $(U, V)$  is the barotropic transport vector. For simplicity we will be using Cartesian coordinates in this chapter. In the model code, spherical coordinates are implemented. Indices  $x$  and  $y$  denote horizontal directions,  $\zeta$  is the sea surface elevation,  $\rho_0$ ,  $\rho$  are the mean sea water density and the deviation from the mean, respectively,  $p = \int_z^0 g\rho dz$  is the baroclinic pressure anomaly,  $f = f(y)$  is the Coriolis parameter,  $A_l$  is the lateral momentum diffusion coefficient,  $H = H(x, y)$  is the depth of the ocean bottom and  $\boldsymbol{\tau} = (\tau_x, \tau_y)$  is the vector of wind stress normalized by  $\rho_0$  applied to the ocean surface. We neglect bottom friction here.

Equations (4.1)–(4.3) are to be solved in a region  $\Gamma_1$  which is the surface of a 3D domain  $\Omega$ . The set of boundary conditions on  $(U, V)$  follows from boundary conditions on the 3D horizontal velocity. They include impermeability of lateral rigid walls

$$(U, V) = 0 \quad \text{on } \Gamma_1 \cap \Gamma_3. \quad (4.5)$$

At the open boundaries the barotropic transports are prescribed

$$(U, V) \cdot \vec{\mathbf{n}} = \mathbf{U}_{\text{OB}} \cdot \vec{\mathbf{n}} \quad \text{on } \Gamma_1 \cap \Gamma_4 \quad (4.6)$$

and tangential component of viscous stress is set to zero. Here  $\Gamma_3$  and  $\Gamma_4$  denote the lateral vertical rigid walls and open boundaries of the domain  $\Omega$  respectively,  $\mathbf{U}_{\text{OB}} \cdot \vec{\mathbf{n}}$  is the barotropic transport through the open boundary.

The 3D momentum equation is to be solved with  $\zeta$  already known:

$$f(\mathbf{k} \times \mathbf{u}) - \nabla \cdot A_l \nabla \mathbf{u} - \partial_z A_v \partial_z \mathbf{u} = -\frac{1}{\rho_0} \nabla p - g \nabla \zeta, \quad (4.7)$$

where  $(\mathbf{u}, w) \equiv (u, v, w)$  is the velocity vector,  $\mathbf{k}$  is the vertical unit vector  $A_v$  is the vertical diffusion coefficients.

The set of boundary conditions used for (4.7) includes the condition for the momentum flux on the ocean surface, the zero bottom-drag condition at the bottom (it is denoted by  $\Gamma_2$ ), no-slip boundary conditions on the vertical walls and the open-boundary condition:

$$A_v \partial_z \mathbf{u} = \boldsymbol{\tau} \quad \text{on } \Gamma_1 \quad (4.8)$$

$$A_v \partial_z \mathbf{u} + A_l (\nabla H \cdot \nabla) \mathbf{u} = 0 \quad \text{on } \Gamma_2 \quad (4.9)$$

$$\mathbf{u} = 0 \quad \text{on } \Gamma_3. \quad (4.10)$$

At the open boundary, the full viscous stress is set to zero. The vertical velocity is determined from the continuity equation subject to the rigid-lid boundary condition at the surface and impermeability condition at the bottom

$$\partial_z w = -\nabla \cdot \mathbf{u} \quad (4.11)$$

$$w = 0 \quad \text{on} \quad \Gamma_1 \quad (4.12)$$

$$w = -\nabla H \cdot \mathbf{u} \quad \text{on} \quad \Gamma_2. \quad (4.13)$$

Anyone of the two boundary conditions can be used. The other one will then be the consequence of the continuity constraint. We keep them, however, both here, as in reality due to finite accuracy of solution for horizontal velocity they are contradictory. To satisfy them, a solvability condition is imposed on the rhs of (4.11) in discretized version of equation (see below).

### 4.1.2 Finite element discretization

As already mentioned, FEOM uses tetrahedral elements and linear basis functions for all prognostic fields. The elements are obtained by first generating the surface triangular mesh, introducing vertical prisms built on surface triangles, cutting them by a set of horizontal surfaces into elementary prisms and finally into tetrahedra. This provides high flexibility for representation of irregular topography and local mesh refinement.

The piece-wise linear basis functions require only nodal values of respective fields and thus provide compact storage for the fields and the matrices associated with equations. The storage factor becomes restrictive when the size of the problem is increased.

Piecewise-linear basis functions are not twice differentiable and one needs to reformulate the problem (4.1)–(4.6), (4.7)–(4.10) in the weak sense. Once again, we are using non-stabilized equations here for the sake of brevity. Multiplying (4.1)–(4.3) by an arbitrary vector field  $(\tilde{U}, \tilde{V}, \tilde{\zeta})$  that does not depend on  $z$ , by making use of Green's formula and boundary conditions (4.5)–(4.6) we arrive at the equations:

$$\int_{\Gamma_1} \left[ (-fV + gH\partial_x\zeta)\tilde{U} + A_l\nabla U\nabla\tilde{U} \right] d\Omega = \int_{\Gamma_1} \left( \tau_x - \frac{1}{\rho_0} \int_{-H}^0 \partial_x p dz \right) \tilde{U} d\Gamma, \quad (4.14)$$

$$\int_{\Gamma_1} \left[ (fU + gH\partial_y\zeta)\tilde{V} + A_l\nabla V\nabla\tilde{V} \right] d\Omega = \int_{\Gamma_1} \left( \tau_y - \frac{1}{\rho_0} \int_{-H}^0 \partial_y p dz \right) \tilde{V} d\Gamma, \quad (4.15)$$

$$\int_{\Gamma_1} (U, V) \cdot \nabla\tilde{\zeta} d\Gamma = \int_{\Gamma_4} \mathbf{v}_{\text{OB}} \cdot \mathbf{n}_3 \tilde{\zeta} d\Gamma. \quad (4.16)$$

Expressing model variables as linear combinations of 2D and 3D piece-wise linear basis functions  $X_k$  and  $S_k$  defined on the tetrahedral partitioning (the

$k$ -th basis function is equal to 1 at the  $k$ -th node and linearly vanishes to 0 within a tetrahedron or triangle containing this node),

$$\mathbf{U} = \sum_{k=1}^{N_{2D}} \mathbf{U}_k S_k, \quad \zeta = \sum_{k=1}^{N_{2D}} \zeta_k S_k, \quad \mathbf{u} = \sum_{k=1}^{N_{3D}} \mathbf{u}_k X_k, \quad \rho_\theta = \sum_{k=1}^{N_{3D}} \rho_{\theta k} X_k \quad (4.17)$$

and replacing the test functions  $\tilde{\mathbf{U}}$  and  $\tilde{\zeta}$  with  $S_i$  one obtains the so-called Galerkin equations on  $\mathbf{U}_k$  and  $\zeta_k$  which are the nodal values of the barotropic transports and sea surface height. Here  $N_{3D}$  and  $N_{2D}$  are the total numbers of 3D and 2D nodes, respectively.

The weak formulation of the 3D momentum equation can be written in the same manner

$$\int_{\Omega} \left[ [f[\mathbf{k} \times \mathbf{u}] + g \nabla \zeta] \cdot \tilde{\mathbf{u}} + A_v \partial_z \mathbf{u} \cdot \partial_z \tilde{\mathbf{u}} + A_l \nabla \mathbf{u} \cdot \nabla \tilde{\mathbf{u}} \right] d\Omega = \quad (4.18)$$

$$\int_{\Gamma_1} \boldsymbol{\tau} \cdot \tilde{\mathbf{u}} d\Gamma - \int_{\Omega} \frac{1}{\rho_o} \tilde{\mathbf{u}} \cdot \nabla p d\Omega,$$

The pressure  $p$  is recovered from density  $\rho$  in the finite difference sense because using finite-element solution here would lead to unacceptably strong noise in horizontal derivatives (see Danilov et al. (2004a)). After obtaining nodal values  $p_k$ , the pressure is treated analogously to (4.17) as

$$p = \sum_{k=1}^{N_{3D}} p_k X_k \quad (4.19)$$

when its contribution into (4.14), (4.15), and (4.18) is computed.

As it is mentioned in chapter 3 a finite element operator corresponding to a first order differential problem has zeros on the diagonal. Iterative solvers are very inefficient in solving such problems especially when the problem becomes large. To solve the first order problem for  $w$  a vertical velocity potential  $\Phi$  is introduced such that  $w = \partial_z \Phi$ . The weak formulation of (4.11) and (4.13) can be written as

$$\int_{\Omega} \partial_z \Phi \partial_z \tilde{\Phi} d\Omega = - \int_{\Omega} \mathbf{u} \cdot \nabla \tilde{\Phi} d\Omega + \int_{\Gamma_4} \mathbf{v}_{OB} \cdot \mathbf{n}_3 \tilde{\Phi} d\Gamma_4 \quad (4.20)$$

$$\Phi = \sum_{k=1}^{N_{3D}} \Phi_k X_k \quad (4.21)$$

and must hold for any  $\tilde{\Phi} \in X$ . The vertical velocity computed in this way is an element-wise constant function. With this scheme of treating the continuity equation, the volume is conserved locally within a cluster of elements having

a node in common (weighted with the test function defined at this node), and globally.

Since both boundary conditions in this scheme are of the von Neumann type, the RHS of (4.20) must satisfy the solvability condition: it must be zero for test functions that do not depend on the vertical coordinate,  $\tilde{\Phi} = \tilde{\Phi}(\lambda, \theta)$ . As we have already mentioned, the latter is guaranteed by the continuity equation up to numerical errors. However, the iterative solver is very sensitive to minor deviations from solvability in the numerical realization of (4.20). This condition is therefore enforced before solving (4.20) by summing the rhs over vertical columns and subtracting small residuals from the upper layer.

### 4.1.3 Velocity correction

There is one particular aspect of using stabilization that needs to be explained. Because of stabilizing the continuity equation there is small inconsistency between the sea surface height  $\zeta$  and 3D horizontal velocities: their vertically integrated divergence is small but not exactly zero. The FEOM and our forward model eliminate this inconsistency by seeking for a 2D correction velocity that is to be subtracted from the  $u$  and  $v$  fields. The velocity correction is expressed as gradient of scalar potential  $\phi$  which is computed by solving

$$\Delta\phi = \nabla \cdot \int_{-H}^0 \mathbf{u} dz \quad \partial_n \phi = 0 \quad \text{on } \partial\Gamma_1. \quad (4.22)$$

This equation is treated in the weak sense in the space of piece-wise linear basis functions  $\phi = \sum \pi_k S_k$ . The overhead of doing velocity correction is minor as it involves solving only a 2D problem with a symmetric sign definite operator. Once  $\phi$  has been computed, the bias  $\nabla\phi$  is extracted from the horizontal velocity field

$$\mathbf{u} \rightarrow \mathbf{u} - H^{-1} \nabla\phi \quad (4.23)$$

The corrected velocity field is used for computing  $w$  in both FEOM and the forward model used by us.

### 4.1.4 Equation for the potential density

Although our forward model deals only with solving the momentum and continuity equations, the IFEOM penalizes the residuals in tracer equations written in the finite-element sense (as Galerkin equations). The discretization of tracer equations is taken from FEOM and that is why we give its description here.

In the frame of this work, a simplified approach is used to the tracer equations. In order to minimize the size of the control parameter vector in the

IFEOM, we are working with the advection–diffusion equation for the potential density (instead of two separate equations for temperature and salinity)

$$\nabla \cdot (\mathbf{u}\rho_\theta) + \partial_z(w\rho_\theta) - \nabla \cdot K_l \nabla \rho_\theta - \partial_z K_v \partial_z \rho_\theta = 0, \quad (4.24)$$

where  $\rho_\theta$  is the potential density,  $K_l$  and  $K_v$  are the lateral and vertical diffusion coefficients. The solution to equation (4.24) should satisfy the following boundary conditions:

$$\rho_\theta = \hat{\rho}_\theta \quad \text{on} \quad \Gamma_1 \quad (4.25)$$

$$(\nabla \rho_\theta, \partial_z \rho_\theta) \cdot \mathbf{n}_3 = 0 \quad \text{on} \quad \Gamma_2 \cup \Gamma_3 \cup \Gamma_4, \quad (4.26)$$

where  $\hat{\rho}_\theta$  is the potential density at the surface,  $\mathbf{n}_3$  is the 3D unit vector of outer normal to the boundaries. Here, the Dirichlet boundary condition is written for the surface which could be replaced by a flux boundary condition. In order to simplify the IFEOM we do not consider the tracer equation at the ocean surface, so the exact boundary condition is irrelevant. Clearly, the information on surface fluxes could be easily incorporated.

The weak form of the advection–diffusion equation for potential density is

$$\int_{\Omega} \left[ (\mathbf{u} \cdot \nabla + w \partial_z) \rho_\theta \tilde{\rho}_\theta + K_l \nabla \rho_\theta \cdot \nabla \tilde{\rho}_\theta + K_v \partial_z \rho_\theta \partial_z \tilde{\rho}_\theta \right] d\Omega = \int_{\Gamma_1} K_v \partial_z \rho_\theta \tilde{\rho}_\theta d\Gamma \quad (4.27)$$

One substitutes expansion for  $\rho_\theta$  in the form of (4.17) into this equation and takes  $\tilde{\rho}_\theta$  to be any of basis functions  $X_k$ . This leads to a system of Galerkin equations on nodal values of  $\rho_\theta$ .

### 4.1.5 Discrete formulation

The Galerkin equations produced by finite-element discretization are systems of linear equations which are solved using iterative solvers. The FEOM introduces and assembles only matrices for the operators (the lhs parts of equations) while the right hand sides of equations are computed in separate subroutines. This is impractical for the IFEOM and the forward model is reformulated in many places compared to FEOM. It introduces several additional matrices serving the purpose of computing the right hand sides, and also represents in matrix form all other operations (such as enforcing the solvability). Writing all steps as a set of matrix problems simplifies then building an adjoint model. Indeed, the matrices of the operators of the adjoint model are transpose of the matrices of forward operators.

Representing the model fields  $U, V, \zeta, u, v, \Phi, \phi, \rho$  by the vectors consisting of their nodal values we can write the finite element discretization of the model in the matrix form. It is summarized below. The notation  $E_{n_1} \dots E_{n_2}$  serves to number all equations ( $n_1$  and  $n_2$  denote the first and the last number).

Equations for the barotropic transports and SSH take the form

$$\begin{pmatrix} E_1 \\ \vdots \\ E_{3n2D} \end{pmatrix} = \mathbf{A}_1 \begin{pmatrix} U \\ V \\ \zeta \end{pmatrix} + \mathbf{R}_{2d,\rho}\rho + \Sigma_{2d} = 0. \quad (4.28)$$

Here the linear operator  $\mathbf{A}_1$  corresponds to the stiffness matrix of the barotropic subproblem of FEOM and has the dimension of  $(3N2D \times 3N2D)$ . The operator  $\mathbf{R}_{2d,\rho}$  of  $(3N2D \times N3D)$  size projects the in-situ density into the rhs vector, and  $\Sigma_{2d}$  is a column vector of size  $(3N2D \times 1)$  which represents the boundary conditions imposed on the problem.

Equations for the horizontal 3D velocity field are

$$\begin{pmatrix} E_{3n2D+1} \\ \vdots \\ E_{2n3D+3n2D} \end{pmatrix} = \mathbf{A}_2 \begin{pmatrix} u \\ v \end{pmatrix} + \mathbf{R}_{3d,\rho}\rho + \mathbf{R}_{3d,\zeta}\zeta + \Sigma_{3d} = 0. \quad (4.29)$$

Here  $\mathbf{A}_2$  is the stiffness matrix of 3D velocity subproblem of FEOM. It has the dimension of  $(2N3D \times 2N3D)$ . The other operators  $\mathbf{R}_{3d,\rho}$  and  $\mathbf{R}_{3d,\zeta}$  are of the size  $(2N3D \times N3D)$  and  $(2N3D \times N2D)$  and project the in-situ density and SSH, respectively, into the vector of rhs. The vector  $\Sigma_{3d}$  of  $(2N3D \times 1)$  size represents the boundary conditions.

Relations which define the potential of velocity correction are written as

$$\begin{pmatrix} E_{2n3D+3n2D+1} \\ \vdots \\ E_{2n3D+4n2D} \end{pmatrix} = \mathbf{A}_3\phi + \mathbf{R}_\phi(\mathbf{R}_1u + \mathbf{R}_2v) = 0, \quad (4.30)$$

where  $\mathbf{A}_3$  is the 2D Laplacian operator (with minus sign) of dimension  $(N2D \times N2D)$ , the operator  $R_\phi$  of size  $(N2D \times N3D)$  represents vertical integration, operators  $\mathbf{R}_1$  and  $\mathbf{R}_2$  of size  $(N3D \times N3D)$  give the divergence of the horizontal velocity vector field  $(u, v)$ .

Equations which define the vertical velocity are

$$\begin{pmatrix} E_{2n3D+4n2D+1} \\ \vdots \\ E_{3n3D+4n2D} \end{pmatrix} = \mathbf{A}_4\Phi + \mathbf{S}(\mathbf{R}_1u + \mathbf{R}_2v + \mathbf{R}_{\mathbf{u}_c}\mathbf{A}_{\mathbf{u}_c}\phi) = 0. \quad (4.31)$$

Here the linear operator  $\mathbf{A}_4$  is the vertical integration stiffness matrix of FEOM. It has the dimension of  $(N3D \times N3D)$ . The operator  $S$  of size  $(N3D \times N3D)$  enforces the solvability condition, the operator  $\mathbf{A}_{\mathbf{u}_c}$  of size  $(2elem2D \times N2D)$  is the 2D gradient operator that transforms the correction potential into the velocity correction, and  $\mathbf{R}_{\mathbf{u}_c}$  stands for the operator (of size  $(N3D \times 2elem2D)$ ) of 2D divergence of the velocity correction.

Finally, we write the relations which give residuals of the equation for the potential density

$$\begin{pmatrix} E_{3n3D+4n2D+1} \\ \vdots \\ E_{4n3D+4n2D} \end{pmatrix} = \mathbf{A}_5(\mathbf{u}, \phi)\rho_\theta = \epsilon. \quad (4.32)$$

Here the linear advection–diffusion operator  $\mathbf{A}_5$  has the dimension of  $(N3D \times N3D)$ , and  $\epsilon=(N3D \times 1)$  is a column vector which represents the residuals of the thermodynamical part.

Having solved the system system (4.28)–(4.31) one can compute the residual term  $\epsilon$  of the thermodynamic equation (4.32).

## 4.2 Constructing the IFEOM

This section gives the description of IFEOM, makes analysis of the adjoint model, and presents its discrete formulation.

### 4.2.1 Control and dependent variables

IFEOM is designed in a way that the density field, the wind stress, and the barotropic transports through the open boundaries can be used as the control parameters. The dependent model parameters are the barotropic transports  $\mathbf{U}$ , sea surface height  $\zeta$ , and full 3D velocity field  $(\mathbf{u}, w)$ .

### 4.2.2 Cost Function

The value of the cost function  $\mathcal{J}$  calculated from all independent and dependent model parameters represents the quality of the actual model state with respect to the data. The minimum of the cost function found with the use of the adjoint method corresponds to the optimal solution. We write the cost function as the following

$$\mathcal{J} = \frac{1}{2} \sum_i \mathbf{J}_i, \quad (4.33)$$

where the factor  $1/2$  is introduced for convenience and terms  $\mathbf{J}_i$  are defined below.

The first term penalizes residuals in the equation for the potential density

$$\mathbf{J}_1 = \int_{\Omega} \int_{\Omega} \epsilon W_{\epsilon}(x, y, z, x'y'z') \epsilon d\Omega d\Omega', \quad (4.34)$$

the second term penalizes displacement of model density from climatological fields projected on the model grid (4.24)

$$\mathbf{J}_2 = \int_{\Omega} \int_{\Omega} (\rho - \rho_{atl}) W_{atl}(x, y, z, x'y'z') (\rho - \rho_{atl}) d\Omega d\Omega'. \quad (4.35)$$

These are two main contributions to the cost function which will be used in all experiments described in chapter 5. The following terms are implemented in the model code. In case the data at sections is used it reads as

$$\mathbf{J}_3 = \sum_{i,j=1}^{N_{den}} (\rho(x_i, y_i, z_i) - \rho_{d_i}) W_{\rho_{d_i,j}} (\rho(x_j, y_j, z_j) - \rho_{d_j}), \quad (4.36)$$

for altimetry the contribution would be

$$\mathbf{J}_4 = \sum_{i,j=1}^{N_{\zeta}} (\zeta(x_i, y_i, z_i) - \zeta_{d_i}) W_{\zeta_{d_i,j}} (\zeta(x_j, y_j, z_j) - \zeta_{d_j}). \quad (4.37)$$

Similarly for the barotropic transport component normal to the open boundary  $\mathbf{U}_{OB} \cdot \vec{\mathbf{n}}$  (it is penalized by the first guess  $\mathbf{U}_{fg} \cdot \vec{\mathbf{n}}$ )

$$\mathbf{J}_5 = \int_{\Gamma_1 \cap \Gamma_4} \int_{\Gamma_1 \cap \Gamma_4} (\mathbf{U}_{OB} - \mathbf{U}_{fg}) \cdot \vec{\mathbf{n}} W_{OB}(x, y, x'y') (\mathbf{U}_{OB} - \mathbf{U}_{fg}) \cdot \vec{\mathbf{n}} dx dy dx' dy', \quad (4.38)$$

and the wind stress

$$\mathbf{J}_6 = \int_{\Gamma_1} \int_{\Gamma_1} (\tau - \tau_{fg}) W_{\tau}(x, y, x', y') (\tau - \tau_{fg}) dx dy dx' dy'. \quad (4.39)$$

The dynamical part of the primitive equations is considered as a strong constraint. The forward model computes  $\mathbf{U}$ ,  $(\mathbf{u}, w)$  and  $\zeta$  for a given set of control parameters. The thermodynamical part exemplified by the stationary advection–diffusion equation for the potential density is a weak constraint and the residual  $\epsilon$  (residual of relation (4.24)) is a measure of inconsistency. We do not solve the advection–diffusion equation for density but try to find the set of control parameters which brings less inconsistency into it.

The Lagrangian function of the problem includes the set of dynamical equations through Lagrangian multipliers (strong constraints) in addition to the cost function  $J$ .

### 4.2.3 Deriving the adjoint equations

We begin with deriving adjoint equations for the continuous equations (4.1–4.12), and discrete formulation will be given in the section 4.2.5. This helps to understand the model specifics which is not necessarily seen from the discrete formulation. For instance, the sea surface height given by the forward model is determined up to a constant because of using the rigid lid approximation. This makes the term  $(\zeta - \zeta_{alt})$  in the cost function  $\mathcal{J}$  undefined when the altimetry data is used: it may jump between iterations of minimizing procedure giving arbitrary increments to  $\mathcal{J}$ . Thus  $\zeta$  should be corrected before its contribution to the cost function is computed, and this correction follows from the solvability condition of the adjoint model. For simplicity, we replace the open boundary with rigid wall. In the IFEOM code, the presence of open boundary is taken into account.

### Adjoint barotropic transports

Assume, for simplicity, that the altimetry and climatology enter the cost function  $J$ , the diagonal weighing scheme (i.e.  $W(x, y, x', y')$  is non zero only if  $x = x'$  and  $y = y'$ ) is used, and that the density is the only control parameter.

The cost function is at its minimum if the variations of the Lagrangian function with respect to its variables are zero. The variables are the Lagrangian multipliers, the sets of dependent and control model parameters.

Consider first the part of the Lagrangian function which corresponds to the equations for the barotropic transports and the sea surface height

$$\begin{aligned} \mathcal{L} = \int_{\Gamma_1} \left[ \lambda_U \left( -fV - A_l \Delta U + gH \partial_x \zeta + \frac{1}{\rho_0} \int_{-H}^0 \partial_x P dz - \tau_x \right) \right. \\ \left. + \lambda_V \left( fU - A_l \Delta V + gH \partial_y \zeta + \frac{1}{\rho_0} \int_{-H}^0 \partial_y P dz - \tau_y \right) + \right. \\ \left. \lambda_\zeta (\partial_x U + \partial_y V) \right] d\Gamma_1 + \dots, \quad (4.40) \end{aligned}$$

where  $\lambda_U$ ,  $\lambda_V$  and  $\lambda_\zeta$  are the Lagrangian multipliers defined on  $\Gamma_1$ .

To derive equations on  $\lambda_U$ ,  $\lambda_V$  and  $\lambda_\zeta$  one computes variations of  $\mathcal{L}$  with respect to  $U$ ,  $V$  and  $\zeta$  and equates them to zero

$$\begin{aligned} \delta \mathcal{L}|_U = \int_{\Gamma_1} \left[ A_l \nabla \lambda_U \cdot \nabla \delta U + \lambda_V f \delta U - \partial_x \lambda_\zeta \delta U \right] d\Gamma \\ - \oint_{\partial \Gamma_1} A_l \lambda_U \nabla \delta U \cdot \vec{n} d\gamma + \oint_{\partial \Gamma_1} \lambda_\zeta \delta U n_x d\gamma = \\ = \int_{\Gamma_1} (-A_l \Delta \lambda_U + \lambda_V f - \partial_x \lambda_\zeta) \delta U d\Gamma - \oint_{\partial \Gamma_1} A_l \lambda_U \nabla \delta U \cdot \vec{n} d\gamma \\ + \oint_{\partial \Gamma_1} \lambda_\zeta \delta U n_x d\gamma + \oint_{\partial \Gamma_1} A_l \delta U \nabla \lambda_U \cdot \vec{n} d\gamma = 0. \quad (4.41) \end{aligned}$$

Here  $\vec{n}(x, y) = (n_x, n_y)$  is a unit normal vector to  $\partial \Gamma_1$ ,  $\delta U = U(x, y) - \tilde{U}(x, y)$  is variation of  $U$ ,  $U$  and  $\tilde{U}$  are arbitrary functions (they must be twice differentiable and square integrable together with their derivatives) which satisfy the boundary conditions for the barotropic transports imposed in the forward problem. It means that  $\delta U(x, y) = 0, \forall (x, y) \in \partial \Gamma_1$  and two last surface integrals in (4.41) vanish.

In order to fulfill  $\delta \mathcal{L}|_U = 0$  all integrals in (4.41) must become zero for arbitrary  $\delta U$  (satisfying boundary conditions). This gives the set of differential equations on  $\lambda_i, i = 1 \dots 3$ , together with boundary conditions:

$$\begin{aligned} A_l \Delta \lambda_U - \lambda_V f + \partial_x \lambda_\zeta &= 0, \\ \lambda_U|_{\partial \Gamma_1} &= 0. \end{aligned} \quad (4.42)$$

In a similar way,  $\delta L|_V = 0$  leads to

$$\begin{aligned} A_l \Delta \lambda_V + \lambda_U f + \partial_y \lambda_\zeta &= 0, \\ \lambda_V|_{\partial\Gamma_1} &= 0. \end{aligned} \quad (4.43)$$

### Adjoint sea surface height

To complete system (4.42), (4.43) we need to compute the variation of the Lagrangian with respect to  $\zeta$ . The part of the Lagrangian which includes  $\zeta$  is

$$\begin{aligned} \mathcal{L} &= \int_{\Gamma_1} gH (\lambda_U \partial_x \zeta + \lambda_V \partial_y \zeta) d\gamma + \int_{\Omega} g (\lambda_u \partial_x \zeta + \lambda_v \partial_y \zeta) d\Omega \\ &\quad + \int_{\Gamma_1} \frac{1}{2} \sum_i (\zeta - \zeta_i^{obs})^2 \delta(x_i, y_i) W_\zeta(x, y) d\gamma + \dots, \end{aligned} \quad (4.44)$$

where  $\delta(x_i, y_i) = \delta(x - x_i)\delta(y - y_i)$  is the delta function and  $\lambda_u$ ,  $\lambda_v$ , and  $\lambda_w$  will further denote the Lagrangian multipliers which correspond to the 3D velocity field. The last term in (4.44) comes from the cost function  $\mathcal{J}$ .

The variation of  $\mathcal{L}$  with respect to  $\zeta$  is

$$\begin{aligned} \delta\mathcal{L}|_\zeta &= \int_{\Gamma_1} gH (\lambda_U \partial_x \delta\zeta + \lambda_V \partial_y \delta\zeta) d\gamma + \int_{\Omega} g (\lambda_u \partial_x \delta\zeta + \lambda_v \partial_y \delta\zeta) d\Omega \\ &\quad + \int_{\Gamma_1} \sum_i (\zeta - \zeta_i^{obs}) \delta(x_i, y_i) W_\zeta(x, y) \delta\zeta d\gamma = \\ &= - \int_{\Gamma_1} g (\partial_x (H\lambda_U) + \partial_y (H\lambda_V)) \delta\zeta d\gamma - \int_{\Gamma_1} \delta\zeta \left[ \int_{-H(x,y)}^0 g (\partial_x \lambda_u + \partial_y \lambda_v) dz \right] d\gamma \\ &\quad + \int_{\Gamma_1} \sum_i (\zeta - \zeta_i^{obs}) \delta(x_i, y_i) W_\zeta(x, y) \delta\zeta d\gamma \\ &\quad + \oint_{\partial\Gamma_1} gH (\lambda_U, \lambda_V) \cdot \vec{n} \delta\zeta d\gamma + \int_{\partial\Omega} g (\lambda_u, \lambda_v) \cdot \vec{n} \delta\zeta d\Gamma, \end{aligned} \quad (4.45)$$

where  $\vec{n}$  is a unit normal vector to the corresponding integration domain.

Integral over  $\partial\Gamma_1$  vanishes since  $\lambda_U|_{\partial\Gamma_1} = 0$  and  $\lambda_V|_{\partial\Gamma_1} = 0$  in accordance to (4.42) and (4.43). From the condition that (4.45) must be zero at the optimal solution for any arbitrary  $\delta\zeta$  it follows that

$$\begin{aligned} \nabla \cdot (H\lambda_U, H\lambda_V) &= - \int_{-H(x,y)}^0 \nabla \cdot (\lambda_u, \lambda_v) dz \\ &\quad - \frac{1}{g} \sum_i (\zeta - \zeta_i^{obs}) \delta(x_i, y_i) W_\zeta(x, y), (x, y) \in \Gamma_1 \\ (\lambda_u, \lambda_v) \cdot \vec{n} &= 0, (x, y) \in \Gamma_2 \cup \Gamma_3 \cup \Gamma_4. \end{aligned} \quad (4.46)$$

This set completes the equations on  $\lambda_U$ ,  $\lambda_V$ ,  $\lambda_\zeta$ . It, however, involves  $\lambda_u$  and  $\lambda_v$  which are yet unknown.

If we integrate (4.46) over  $\Gamma_1$  and take into account that  $\lambda_U|_{\partial\Gamma_1} = 0$ ,  $\lambda_V|_{\partial\Gamma_1} = 0$ , we obtain the solvability condition for (4.46): the integral of the right hand side of (4.46) over  $\Gamma_1$  is zero. Below we will show that  $\lambda_u, \lambda_v$  vanish on  $\Gamma_3 \cup \Gamma_4$  and thus

$$\int_{\Gamma_1} \left[ \int_{-H(x,y)}^0 (\partial_x \lambda_u + \partial_y \lambda_v) dh \right] d\gamma = \int_{\Omega} \nabla \cdot (\lambda_u, \lambda_v) d\Omega = \int_{\Gamma_3 \cup \Gamma_4} (\lambda_u, \lambda_v) \vec{n} d\Gamma = 0.$$

It transforms the solvability condition into

$$\int_{\Gamma_1} \sum_i (\zeta - \zeta_i^{obs}) \delta(x_i, y_i) W_\zeta(x, y) \delta\zeta d\gamma = \sum_i (\zeta_i - \zeta_i^{obs}) W_i^\zeta = 0, \quad (4.47)$$

where  $\zeta_i = \zeta(x_i, y_i)$ ,  $W_i^\zeta = W_\zeta(x_i, y_i)$ . Relation (4.47) removes the freedom in the definition of  $\zeta$  in the rigid lid approximation, see section 4.2.4

### Adjoint 3D velocity field

Computing the variation of the Lagrangian with respect to velocity  $u$  gives

$$\begin{aligned} \delta\mathcal{L}|_u &= \int_{\Omega} \left[ \lambda_u (-\nabla \cdot A_l \nabla \delta u - \partial_z A_v \partial_z \delta u) + \lambda_v f \delta u + \lambda_w \partial_x \delta u + \epsilon W_\epsilon \partial_x \rho_\theta \delta u \right] d\Omega \\ &= \int_{\Omega} \left[ -\nabla \cdot A_l \nabla \lambda_u - \partial_z A_v \partial_z \lambda_u + \lambda_v f - \partial_x \lambda_w + \epsilon W_\epsilon \partial_x \rho_\theta \right] \delta u d\Omega \\ &\quad + \int_{\partial\Omega} A_l \nabla \lambda_u \delta u \vec{n} d\Gamma - \int_{\partial\Omega} \lambda_u A_l \nabla \delta u \vec{n} d\Gamma \\ &\quad + \int_{\partial\Omega} A_v \partial_z \lambda_u \delta u n_z d\Gamma - \int_{\partial\Omega} \lambda_u A_v \partial_z \delta u n_z d\Gamma \\ &\quad + \int_{\partial\Omega} \lambda_w \delta u n_x d\Gamma = 0. \quad (4.48) \end{aligned}$$

The term including  $\epsilon$  comes from the cost function  $\mathcal{J}$ . Some of surface integrals vanish because  $\delta u = 0$  on  $\Gamma_3$  and  $\Gamma_4$  due to boundary conditions of the forward problem. In order to guarantee that the remaining integrals also vanish the following set of differential equations is to be satisfied

$$\begin{aligned} -\nabla \cdot A_l \nabla \lambda_u - \partial_z A_v \partial_z \lambda_u + \lambda_v f - \partial_x \lambda_w - \epsilon W_\epsilon \partial_x \rho_\theta &= 0, (x, y, z) \in \Omega \\ A_v \partial_z \lambda_u &= 0, (x, y, z) \in \Gamma_1 \\ \lambda_w n_x + A_l (\nabla H \cdot \nabla) \lambda_u + A_v \partial_z \lambda_u &= 0, (x, y, z) \in \Gamma_2 \\ \lambda_u &= 0, (x, y, z) \in \Gamma_3, \Gamma_4. \end{aligned} \quad (4.49)$$

In a similar manner,  $\delta\mathcal{L}|_v = 0$  translates into

$$\begin{aligned}
-\nabla \cdot A_l \nabla \lambda_v - \partial_z A_v \partial_z \lambda_v - \lambda_u f - \partial_y \lambda_w - \epsilon W_\epsilon \partial_y \rho_\theta &= 0, (x, y, z) \in \Omega \\
A_v \partial_z \lambda_v &= 0, (x, y, z) \in \Gamma_1 \\
\lambda_w n_y + A_l (\nabla H \cdot \nabla) \lambda_v + A_v \partial_z \lambda_v &= 0, (x, y, z) \in \Gamma_2 \\
\lambda_v &= 0, (x, y, z) \in \Gamma_3, \Gamma_4.
\end{aligned} \tag{4.50}$$

Finally, varying  $\mathcal{L}$  with respect to  $w$  we write

$$\begin{aligned}
\delta\mathcal{L}|_w &= \int_{\Omega} \left[ \lambda_w (\partial_z \delta w) + \epsilon W_\epsilon \partial_z \rho_\theta \delta w \right] d\Omega = \\
&\int_{\Omega} \left[ -\partial_z \lambda_w + \epsilon W_\epsilon \partial_z \rho_\theta \right] \delta w d\Omega + \int_{\partial\Omega} \lambda_w \delta w n_z d\Gamma = 0. \tag{4.51}
\end{aligned}$$

It gives us the relation on  $\lambda_w$ .

$$\begin{aligned}
\partial_z \lambda_w - \epsilon W_\epsilon \partial_z \rho_\theta &= 0, (x, y, z) \in \Omega \\
\lambda_w &= 0, (x, y, z) \in \Gamma_2
\end{aligned} \tag{4.52}$$

Equations (4.42), (4.43), (4.46), (4.49), (4.50) and (4.52) complete the set of relations which define the Lagrangian multipliers. When they are known the variance of the Lagrangian by control parameter can be computed.

As a result of this computations we see that the inverse problem is well posed when the solvability condition (4.47) is satisfied.

#### 4.2.4 Sea surface height correction

Since the forward model uses the rigid lid approximation, the sea surface height  $\zeta$  is determined up to a constant. The idea (in case of using altimetry observations) is to redefine the difference  $\zeta(x_i, y_i) - \zeta_i^{obs}$  which enters the cost function by subtracting a constant from the computed  $\zeta$ . This would modify (4.47) as

$$\sum_i (\zeta_i - r - \zeta_i^{obs}) W_i^\zeta = 0$$

or

$$r = \frac{\sum_i (\zeta_i - \zeta_i^{obs}) W_i^\zeta}{\sum_i W_i^\zeta}. \tag{4.53}$$

The displacement  $r$  fixes the arbitrariness in  $\zeta$  in a way compatible with the cost function. However,  $r$  is the function of  $\zeta$  itself and the derivative of  $r$  with respect to  $\zeta$  is to be taken into account when varying the cost function.

Yet this derivative vanishes as is straightforward to show by verifying that the next relation holds

$$\int_{\Gamma_1} \sum_i (\zeta - r - \zeta_i^{obs}) \delta(x_i, y_i) W_\zeta(x, y) \delta\zeta d\gamma = \delta\mathcal{J}|_\zeta.$$

The term in the right hand side can be easily computed ( $\delta_{i,j}$  represents the Kroneker delta function)

$$\begin{aligned} \frac{\delta\mathcal{J}}{\delta\zeta_l} &= \sum_i \left[ W_i^\zeta (\zeta_i - r - \zeta_i^{obs}) \left( \delta_{i,l} - \frac{\sum_j W_j^\zeta \delta_{j,l}}{\sum_j W_j^\zeta} \right) \right] = \\ &= W_l^\zeta (\zeta_l - r - \zeta_l^{obs}) - \sum_i \left[ W_i^\zeta (\zeta_i - r - \zeta_i^{obs}) \frac{W_l^\zeta}{\sum_j W_j^\zeta} \right] = \\ &= W_l^\zeta (\zeta_l - \zeta_l^{obs}) - \sum_i \left[ W_i^\zeta (\zeta_i - \zeta_i^{obs}) \frac{W_l^\zeta}{\sum_j W_j^\zeta} \right] = \\ &= W_l^\zeta (\zeta_l - \zeta_l^{obs}) - W_l^\zeta \sum_i \left[ \frac{W_i^\zeta (\zeta_i - \zeta_i^{obs})}{\sum_j W_j^\zeta} \right] = W_l^\zeta (\zeta_l - r - \zeta_l^{obs}). \end{aligned} \quad (4.54)$$

It exactly coincides with the relation written above. Thus no changes are required in adjoint equations after  $r$  given by 4.53 is subtracted from  $\zeta$ .

## 4.2.5 Discrete formulation

The discrete formulation of IFEOM requires first rewriting the Cost Function (4.34)–(4.39) in the discrete form. We replace the weights and model variables by their discrete representation keeping the same notation as those used in (4.34)–(4.39). The cost function can be written in general as

$$\mathcal{J} = \frac{1}{2} \left[ \epsilon^T W_\epsilon \epsilon \right] \quad (4.55)$$

$$+ (\rho - \rho_{atl})^T W_{atl} (\rho - \rho_{atl}) \quad (4.56)$$

$$+ (K_{proj}\rho - \rho_d)^T W_{\rho d} (K_{proj}\rho - \rho_d) \quad (4.57)$$

$$+ (\zeta - \zeta_{di})^T W_\zeta (\zeta - \zeta_{dj}) \quad (4.58)$$

$$+ U_{OB} W_{OB} U_{OB} \quad (4.59)$$

$$+ (\tau - \tau_{fg}) W_\tau (\tau - \tau_{fg}), \quad (4.60)$$

where model variables now are vectors consisting of nodal values, weights  $W$  are positive definite matrices,  $K_{proj}$  is the operator that projects the model density onto the data points. The three last terms (4.58–4.60) are present in IFEOM, but will not be used in our experiments discussed in the following chapter.

Equations for the Lagrangian multipliers can be written in the discrete case as follows: for the Lagrangian multipliers for barotropic transports and sea surface height

$$\frac{\partial \mathcal{L}}{\partial(U, V, \zeta)} = \frac{\partial \mathcal{J}}{\partial(U, V, \zeta)} + \mathbf{A}_1^T \begin{pmatrix} \lambda_1 \\ \vdots \\ \lambda_{3n2D} \end{pmatrix} + \begin{pmatrix} 0 \\ 0 \\ \mathbf{R}_{3d, \zeta}^T \end{pmatrix} \begin{pmatrix} \lambda_{3n2D+1} \\ \vdots \\ \lambda_{2n3D+3n2D} \end{pmatrix} = 0, \quad (4.61)$$

for the Lagrangian multipliers for the full velocity field

$$\begin{aligned} \frac{\partial \mathcal{L}}{\partial(u, v)} = \frac{\partial \mathcal{J}}{\partial(u, v)} + \mathbf{A}_2^T \begin{pmatrix} \lambda_{3n2D+1} \\ \vdots \\ \lambda_{2n3D+3n2D} \end{pmatrix} + \begin{pmatrix} \mathbf{R}_1^T \mathbf{S}^T \\ \mathbf{R}_2^T \mathbf{S}^T \end{pmatrix} \begin{pmatrix} \lambda_{2n3D+4n2D+1} \\ \vdots \\ \lambda_{3n3D+4n2D} \end{pmatrix} \\ + \begin{pmatrix} \mathbf{R}_1^T \mathbf{R}_\Phi^T \\ \mathbf{R}_2^T \mathbf{R}_\Phi^T \end{pmatrix} \begin{pmatrix} \lambda_{2n3D+3n2D+1} \\ \vdots \\ \lambda_{2n3D+4n2D} \end{pmatrix} = 0, \end{aligned} \quad (4.62)$$

for the Lagrangian multipliers for the velocity correction

$$\frac{\partial \mathcal{L}}{\partial \phi} = \frac{\partial \mathcal{J}}{\partial \phi} + \mathbf{A}_3^T \begin{pmatrix} \lambda_{2n3D+3n2D+1} \\ \vdots \\ \lambda_{2n3D+4n2D} \end{pmatrix} + \mathbf{A}_{\mathbf{u}_c}^T \mathbf{R}_{\mathbf{u}_c}^T \mathbf{S}^T \begin{pmatrix} \lambda_{2n3D+4n2D+1} \\ \vdots \\ \lambda_{3n3D+4n2D} \end{pmatrix} = 0, \quad (4.63)$$

and finally for the Lagrangian multipliers for the vertical velocity potential

$$\frac{\partial \mathcal{L}}{\partial \Phi} = \frac{\partial \mathcal{J}}{\partial \Phi} + \mathbf{A}_4^T \begin{pmatrix} \lambda_{2n3D+4n2D+1} \\ \vdots \\ \lambda_{3n3D+4n2D} \end{pmatrix} = 0. \quad (4.64)$$

With the use of Lagrangian multipliers it is straightforward to compute the gradient of the Lagrangian function with respect to the control parameters. The gradient of  $\mathcal{L}$  with respect to  $\rho$  is

$$\begin{aligned} \frac{\partial \mathcal{L}}{\partial \rho} = \mathbf{W}_{atl}(\rho - \rho_{atl}) + K_{proj}^T W_{pd}(K_{proj}\rho - \rho_d) + \mathbf{A}_5^T(\mathbf{u}, \phi) \mathbf{W}_{F_\rho} \mathbf{A}_5(\mathbf{u}, \phi) \rho \\ + \mathbf{R}_{3d, \rho}^T \begin{pmatrix} \lambda_{3n2D+1} \\ \vdots \\ \lambda_{2n3D+3n2D} \end{pmatrix} + \mathbf{R}_{2d, \rho}^T \begin{pmatrix} \lambda_1 \\ \vdots \\ \lambda_{3n2D} \end{pmatrix}. \end{aligned} \quad (4.65)$$

Gradients over other control parameters (if any) are computed in a similar manner. System (4.61)–(4.64) is solved in backward order. For the arbitrary

set of control parameters the dependent model variables are first computed from (4.28)–(4.32). This makes possible computing the value of the cost function  $\mathcal{J}$  and then the Lagrangian multipliers. From (4.64) we get the Lagrangian multipliers for the vertical velocity potential. Using them we compute the Lagrangian multipliers for the velocity correction from (4.63). Equations (4.62) and (4.61) define the rest of the Lagrangian multipliers. First we compute them for the full velocity, then for the barotropic transports and sea surface height. Finally, using the control and dependent parameters and Lagrangian multipliers we compute the gradient of the cost function with respect to the control variables (4.65). By construction, we have now transformed the constrained minimization of  $\mathcal{J}$  in the space of control variables into an unconstrained optimization problem in the space of control variables augmented by  $\lambda$ . This new problem is much larger but easier to solve (Dimet and Talagrand, 1986). We apply a limited memory quasi Newton method (BFGS) originally suggested by Nocedal (1980) and made available to the scientific community by Institut National de Recherche en Informatique et en Automatique (INRIA). Following their recommendations for large problems (we solve for 220,000 control parameters and about 1000,000 dependent variables) the 7 last gradient directions are used for approximation of the inverse of the local Hessian matrix. The routine M1QN3 (Gilbert and Lemaréchal, 1993) is used to update the control parameters so that the cost function  $\mathcal{J}$  is decreasing.

Schematically, IFEOM can be represented as the following

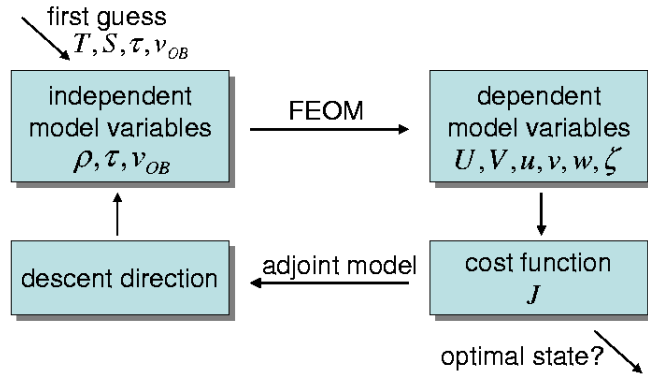


Figure 4.1: Scheme of the Inverse Finite Element Ocean model. The first guess of control parameters is passed to the forward model (FEOM). It produces the dependent model parameters. They are used to compute the value of the cost function  $\mathcal{J}$ . If it is more than some threshold value, gradient of  $\mathcal{J}$  is computed with the use of the adjoint model. It is used to construct the new set of control parameters which would reduce the cost function  $\mathcal{J}$ .



# Chapter 5

## North Atlantic circulation obtained by assimilating climatological data sets

This chapter deals with applications of the IFEOM described in the previous chapter to the North Atlantic. It presents estimates of the large-scale circulation based on assimilation of three data sets, the temperature and salinity of the World Ocean Atlas (Levitus et al., 1994; Levitus and Boyer, 1994), nine pentades of the Lozier climatology (Lozier et al. (1995)) and the novel dataset of Gouretski and Koltermann (2004). Although the full IFEOM could use wind forcing and transports at open boundaries as control parameters, here we are using a simplified approach with the control parameter including only the density.

The solution obtained by applying the variational method to estimating the stationary ocean circulation is sensitive to the starting point for the minimization and to constraints used to express our a priori knowledge about the ocean circulation. This problem was attributed by Tziperman et al. (1992b) to the general facts: First, the cost function has multiple local minima and the minimization could end at some local minimum which does not necessarily correspond to the global minimum of the cost function. Second, it is rather difficult to find an absolute minimum for the cost function given the large size of the minimization in particular when the problem is ill-posed.

The first section of this chapter describes the model setup for the North Atlantic. The IFEOM grid for the North Atlantic coincides with the grid used by Danilov et al. (2004b), and this choice was motivated by the fact that the FEOM produces an acceptable circulation on this grid.

It is followed by the section describing the stationary inverse of LEVITUS climatology (Levitus et al., 1994; Levitus and Boyer, 1994) with the mean wind stress from Trenberth et al. (1990) obtained by applying forward model of IFEOM. The circulation field obtained in this way looks acceptable in many places, however, its integral properties do not agree with numerous estimates

available. This shows the need to improve the solution, that is, for running the IFEOM.

The first question to be solved before running the inverse model is about the starting point for the minimization. Using the Levitus climatology as the starting point lead us generally to a circulation with inacceptably small integral transports (the meridional overturning and barotropic streamfunctions).

In order to overcome this difficulty we follow the approach which is similar to that suggested by Marotzke and Wunsch (1993) and after by Yu and Malanotte-Rizzoli (1996). They showed that taking the starting point from the full forward model lead to a much more realistic results with the meridional overturning being much closer to the accepted values. The third section briefly describes the solution produced by the FEOM.

The following section describes weights for different costs of the objective function and the results of the optimization runs starting from forward estimate. The results show that the suggestion of Marotzke and Wunsch (1993) could not eliminate problems in our case. We show that in order to force the optimal solution to keep the integral properties of the circulation it is necessary to use additional constraints.

The choice of these additional constraints plays a central role in making the IFEOM successful. After experimenting with many variants not described here we found that penalizing the deviation of the deep pressure gradient from that obtained in the FEOM forward run averaged over some period of time performs best. In section 5.6 we describe the deep pressure constraint, and section 5.7 presents results of assimilating the Levitus climatology using this additional constraint. The solution found in this way retains the integral properties of the FEOM solution, but corrects the local properties of the latter in many places. The optimized density field does not depend on the starting point for the minimizer and its deviation from the data ranges of climatological annual cycle.

As the next step we assimilate pentadal temperature and salinity data of Lozier et al. (1995) which represent the set of mean hydrography fields for five year periods from 1950 to 1994. Finally we assimilate the novel dataset by Gouretski and Koltermann (2004) which is the most recent one. The results are presented in section 5.8 and 5.10 respectively. They show that climatology of Gouretski and Koltermann (2004) reproduces some details of circulation better than other datasets. The comparison of transports of assimilated climatologies with estimates given by other models is given in section 5.11. This section shows that our estimates are close to those obtained by other authors. It also shows that assimilation of LEVITUS94 climatology tends to underestimate the transports across some sections. It is followed by presenting the interpentadal variability of the circulation in the North Atlantic. We present the changes in volume transports across some sections and variability in barotropic and overturning streamfunctions.

## 5.1 Model setup

The IFEOM results are presented for the North Atlantic setup. The computational mesh covers the region from  $7^\circ$  N to  $80^\circ$  N. It is based on a surface triangular mesh consisting of approximately 16000 surface nodes, and 23  $z$  levels in vertical direction (see Fig.5.1). Each surface triangle defines a vertical

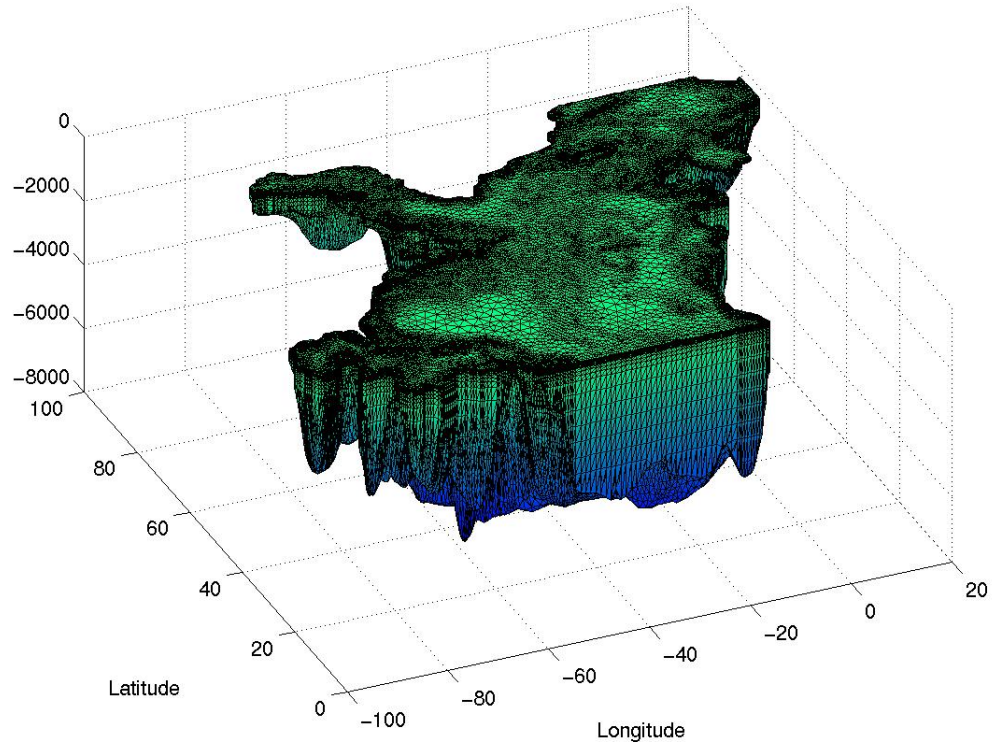


Figure 5.1: 3D mesh of the North Atlantic used with IFEOM.

prism which is subdivided by level surfaces into elementary prisms. The latter are split into tetrahedra. The surface mesh defines horizontal resolution, which varies from  $0.2$  to  $1.5^\circ$ , with mean of approximately  $0.5^\circ$ . The total number of 3D nodes is approximately 220000, and they form 1200000 tetrahedra. To solve the sets of model linear equations we use the PILUT solver by Karypis and Kumar (1998) (PILUT stands for Parallel Threshold-based ILU Factorization). Iterations are done with GMRES or BICGSTAB algorithms. The M1QN3 minimizer of Gilbert and Lemaréchal (1993) based on the quasi-Newton method is used to find the minimum of the cost function.

The current version of IFEOM uses prescribed values for the viscosity and diffusivities. They are the same in all experiments and have the following values:  $A_l=200 \text{ m}^2/\text{s}$ ,  $A_v = 0.02 \text{ m}^2/\text{s}$  for the horizontal and vertical viscosities, respectively, and  $K_l=200 \text{ m}^2/\text{s}$  and  $K_v = 0.02 \text{ m}^2/\text{s}$  for diffusivities. The

vertical diffusivities are higher than is accepted in ocean circulation models. Here, however, the tracer (density) equation is not solved, but only estimated, and the density field is constrained by data.

Although the IFEOM could include open boundary transports and wind stress into control parameters, only the density is used here. Correspondingly, the open boundaries are ‘closed’ and the wind forcing is not optimized in the presented results. We checked that using wind, open boundary velocities and density as control parameters does not lead to any serious advantages over using only density in the experiments considered here. The wind stress is taken from NCEP reanalysis (see e.g., Trenberth et al., 1990). In the case of pentades we are using the mean wind stress for the appropriate period of time.

## 5.2 Analysis of climatology data

Before performing the assimilation of climatology data it is instructive to analyze them. The analysis immediately shows why assimilation is needed. Our goal in this section is to discuss the velocity field which corresponds to the density taken from the World Ocean Atlas 1994 (Levitus et al., 1994; Levitus and Boyer, 1994). To compute the velocity field and sea surface height we first project the data onto the model grid and compute the right hand side of the forward model. Solving the dynamical equations one then finds the velocity field and sea surface height. The fields obtained in this way as well as their transports are shown in Fig. 5.2–5.5 which display the horizontal velocity field close to the surface (50 m) and at the depth (2000 m), the sea surface height and the meridional overturning streamfunction. At the first glance, velocities found by inverting the climatology data look acceptable given the smooth character of climatological fields.

The Western Boundary Current is continuous from Florida Strait to Cape Hatteras (Fig. 5.2). The highest velocities are found close to the coast and reach 0.4 m/s at 30 m depth. The Gulf Stream separation is at about 35 °N (the latitude of Cape Hatteras). The Gulf Stream turns northward at 48 °W and then eastward at 47 °N to enter the northeastern Atlantic as a broad, smooth current. The East and West Greenland Currents are well reproduced (not shown in Fig. 5.2). The Labrador Current follows along the continent and reaches 40°N where it turns eastward and merges into the Gulf Stream. However, there is no Azores Current as could be seen from the sea surface height pattern of Fig. 5.4. On the eastern coast, a spurious northward current exists between 7°N to the 45°N. It might be the consequence of smoothing the topography along the eastern coast. In the deep ocean, starting from 900 m depth the Deep Western Boundary Current could be observed going from eastern Greenland (64°N) and following along the continent up to the open boundaries (Fig. 5.3). However, it shows strong artificial recirculation at around 30°N.

The sea surface height (Fig. 5.4) is characterized, as expected, by weak gradients. Its magnitude is within 0.8 m.

The subtropical gyre in the barotropic streamfunction (not shown here) is shifted to the western coast. This is probably caused by the artificial northward current which occur at the eastern boundary. This current is mostly barotropic and contributes dramatically to the streamfunction and strongly modifies the meridional overturning.

The overturning streamfunction shows several cells and has extremely weak basinwide overturning pattern with a maximum of only 6.5 Sv (Fig. 5.5). It presents the main problem of this solution and signals out that important balances are destroyed. A similar result was found by Marotzke and Wunsch (1993). They report a very weak meridional overturning of 6 Sv for the case when they used climatological data to initialize their inverse model. They attributed it to the lack of a geostrophic Gulf Stream in the climatology at about 30°N.

Thus, the stationary circulation, computed by climatological wind, temperature and salinity does not possess desirable integral features although it still could seem locally satisfactory in several places. The general problem here is inconsistency in the JEBAR (joint effect of baroclinicity and relief) term due to different smoothing of data and topography. JEBAR term appears in the vorticity balance for the barotropic flow and involves product of gradients of the vertically integrated potential energy and the depth. In some cases this term can become dominant in the vorticity balance for the depth-averaged flows (see, e.g., Olbers and Eden, 2003). Therefore it requires adjusting the density field so that it realizes a compromise between being close to the data and dynamically consistent.

Figure 5.6 shows the standard deviation (STD) of the Levitus climatological data (Levitus et al., 1994; Levitus and Boyer, 1994) for density at depths of 50, 500 and 1500 m, respectively. It is computed from the set of monthly mean values for temperature and salinity and will be used further for estimates of the quality of our solutions. In some cases (presented below), we derive our weights based on the STD of density presented in these figures (see sections 5.4 and 5.5).

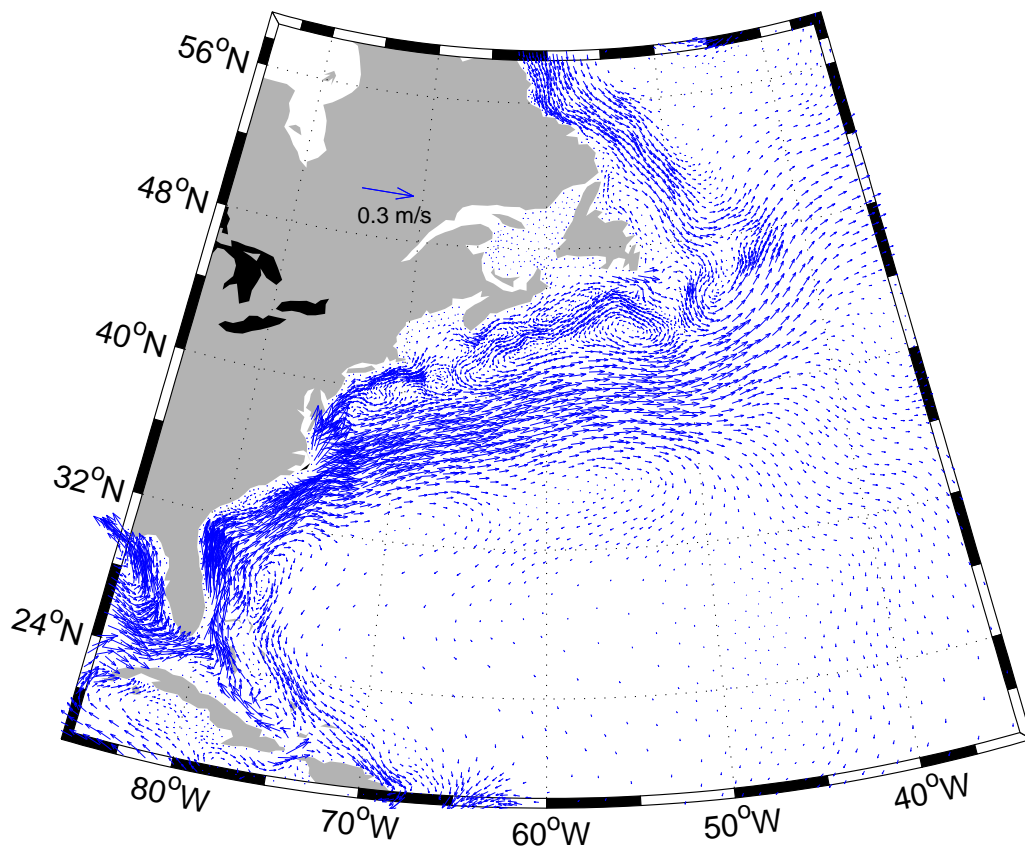


Figure 5.2: Velocity at 50 m depth corresponding to climatological data of Levitus et al. (1994); Levitus and Boyer (1994).

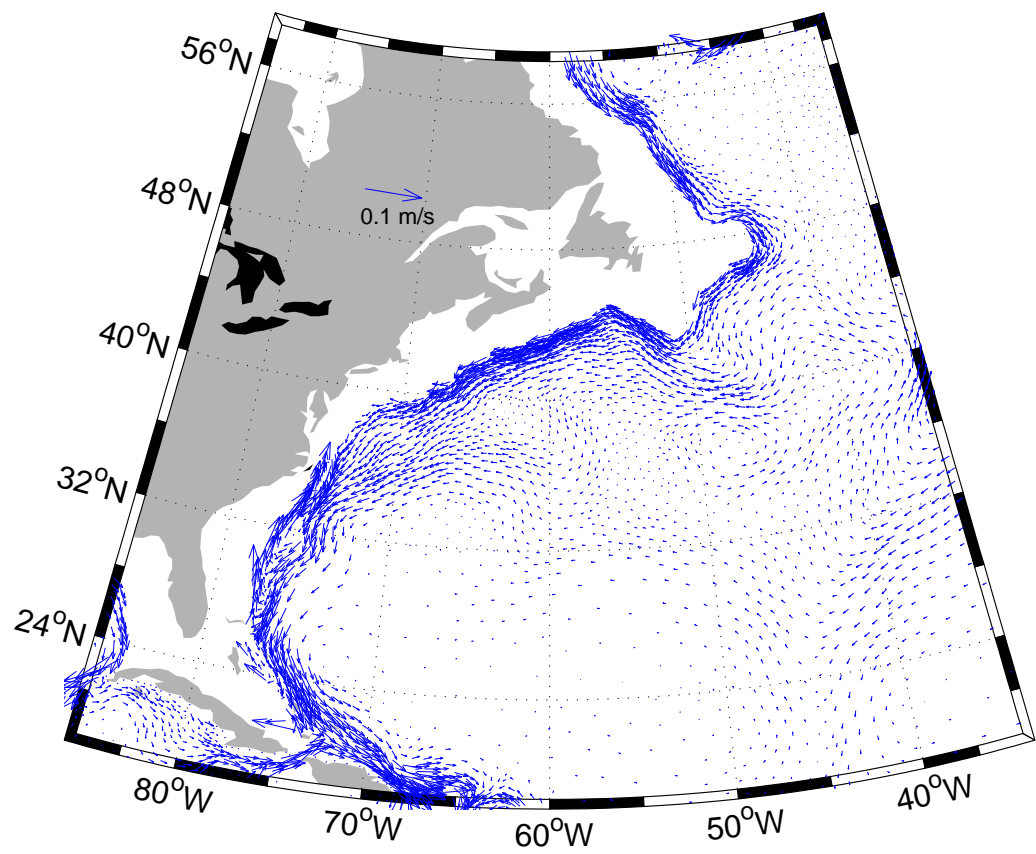


Figure 5.3: Same as in Fig. 5.2 but at 2000 m depth. The Deep Western Boundary Current shows strong artificial recirculation at around 30°N.

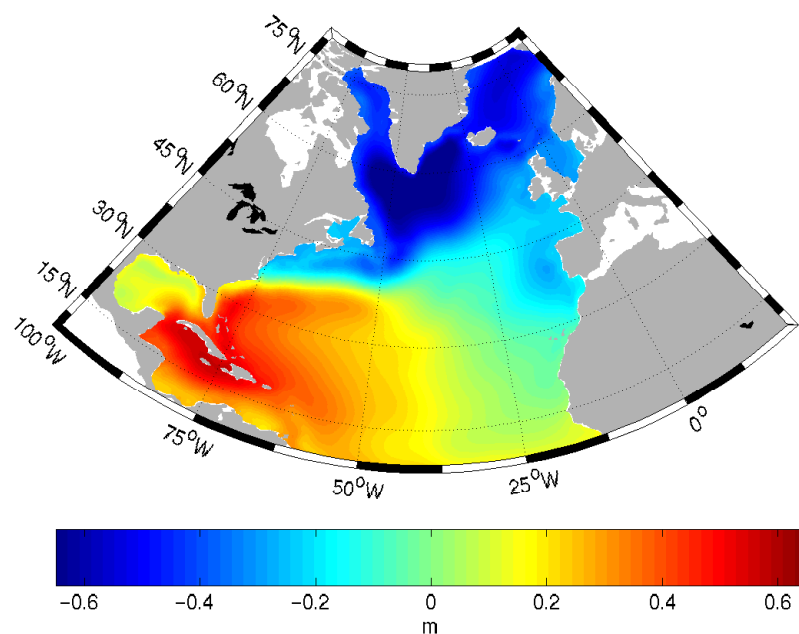


Figure 5.4: Sea surface height corresponding to climatological data of Levitus et al. (1994); Levitus and Boyer (1994). The SSH field is too smooth reflecting the smoothness of the data.

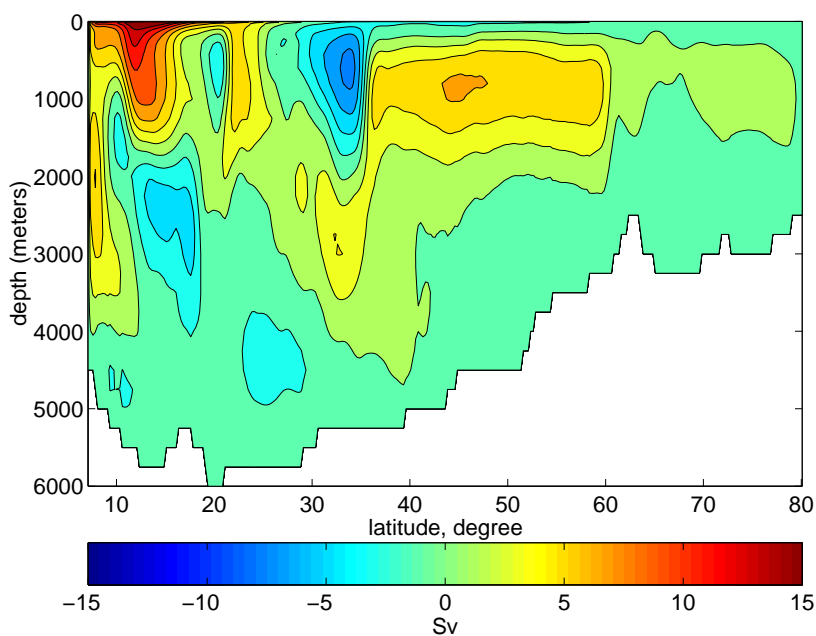


Figure 5.5: Meridional overturning streamfunction computed for climatological data (Levitus et al., 1994; Levitus and Boyer, 1994) analysis. It consist of multiple cells, and basinwide overturning pattern has a maximum of 6.5 Sv. Contour interval is 2 Sv.

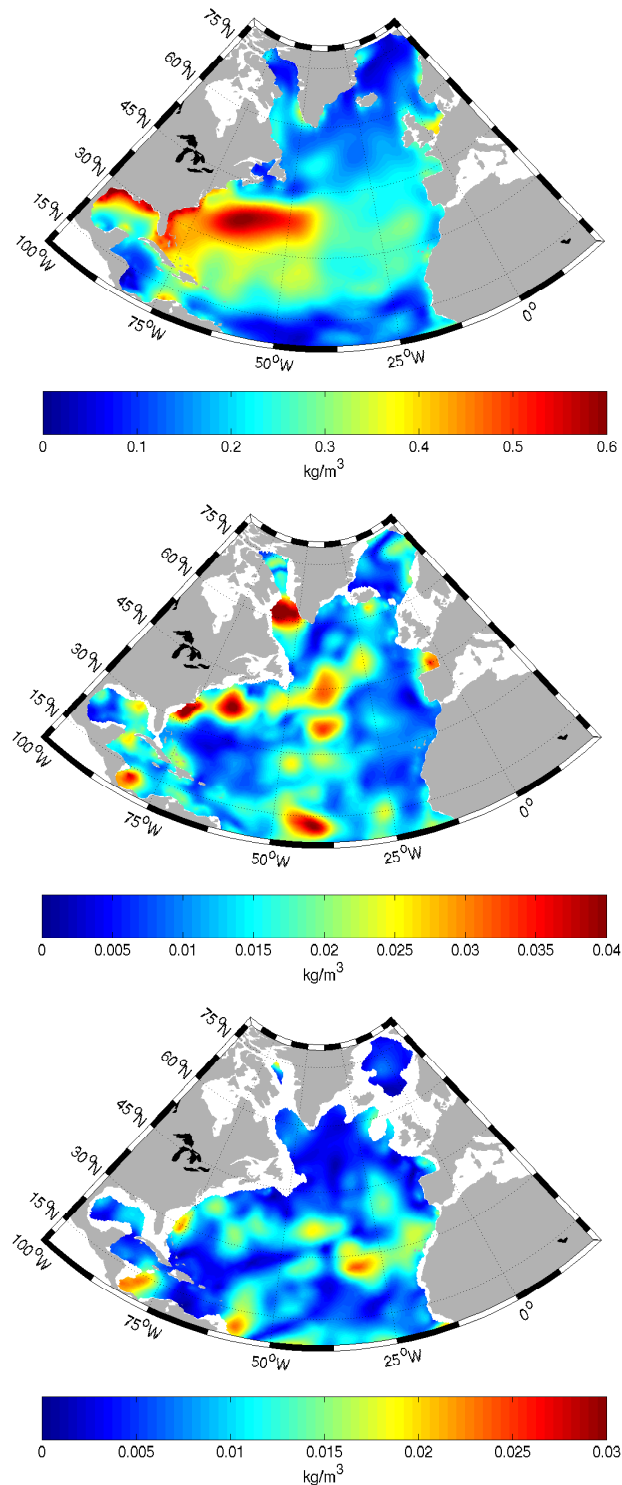


Figure 5.6: Estimated standard deviations for the density field (from the annual cycle of WOA94 climatology) at different depth levels. At 50 m depth on the upper panel, at 500 m on the middle panel and at 1500 m on the lower panel in  $\text{kg/m}^3$ .

### 5.3 Forward estimate

Similarly to the results of Marotzke and Wunsch (1993) it turns out that in our case, assimilation of climatology data instead of simple analysis of them (see section 5.5) does not help if the initial state is taken to be close to climatology and if only the deviation from data and residuals in potential density equation are penalized. We can successfully decrease the residuals in the equation for the potential density and approach sufficiently close to the data. Yet the artificial currents on the eastern coast will not disappear and both, the barotropic and the meridional overturning streamfunctions will be very far from the expected patterns. This indicates that the inverse model has several oceanic states all consistent with what is known (the cost function  $\mathcal{J}$  has several minimas) and we are moving to a particular one which corresponds to weak circulation if no additional constraints are invoked and an initial guess is too close to climatology data.

To overcome the initialization problem Marotzke and Wunsch (1993) run the full forward model, forced by the observed surface fluxes for 250 days and use the final state of this "spin-up" as the starting point for their minimization. At the end of the spin up they obtained the overturning cell of 12 Sv.

We follow a similar approach and use the mean temperature and salinity from output of the FEOM forced by the observed surface fluxes in time-stepping mode for ten years. Alone or in combination with climatology it serves as the first guess to initialize the minimization problem. The mean FEOM solution will be called the forward estimate.

The mean horizontal velocity field of the forward estimate shows Deep Western Boundary Current with stronger velocities (see Fig. 5.7) than in the case of analysis of Levitus climatology (see Fig. 5.3), does not contain the artificial current at the eastern boundary and results in the overturning cell of 19 Sv (Fig.5.8).

The barotropic streamfunction which corresponds to the forward estimate (Fig. 5.9) has small magnitudes in the subtropical gyre. This happens because of the big part of the Gulf Stream follows the coastline further north from  $35^\circ$  N and matches horizontal position of the Deep Western Boundary current in the vertical profile.

Although such a behavior of the Gulf Stream is a common feature of non eddy-resolving models, in our particular case it could be also triggered by too deep topography along the western coast and oversmoothed continental slope which affects the circulation in the upper ocean.

There are noticeable differences between the forward estimate of the density field and the density computed from the Levitus Climatology especially in the upper ocean. At 50 m depth, the difference could reach more than  $0.5 \text{ kg/m}^3$  at some places. However, this is within the estimate of standard deviation for density (see upper panels on Fig. 5.10 and Fig. 5.6) at the same depth. At already 500 m depth the difference is much smaller. The maximum amplitude

slightly exceeds  $0.2 \text{ kg/m}^3$ . It is however much bigger than the estimate of standard deviation at the same depth (middle panels on Fig. 5.10 and Fig. 5.6). In the deep ocean at 1500m (lower panels on Fig. 5.10 and Fig. 5.6), the difference in density does not exceed  $0.07 \text{ kg/m}^3$ . It indicates that the deep ocean is not changing dramatically within 10 years of the model run. At the depth more than 2000m, the differences are in agreement with the standard deviations.

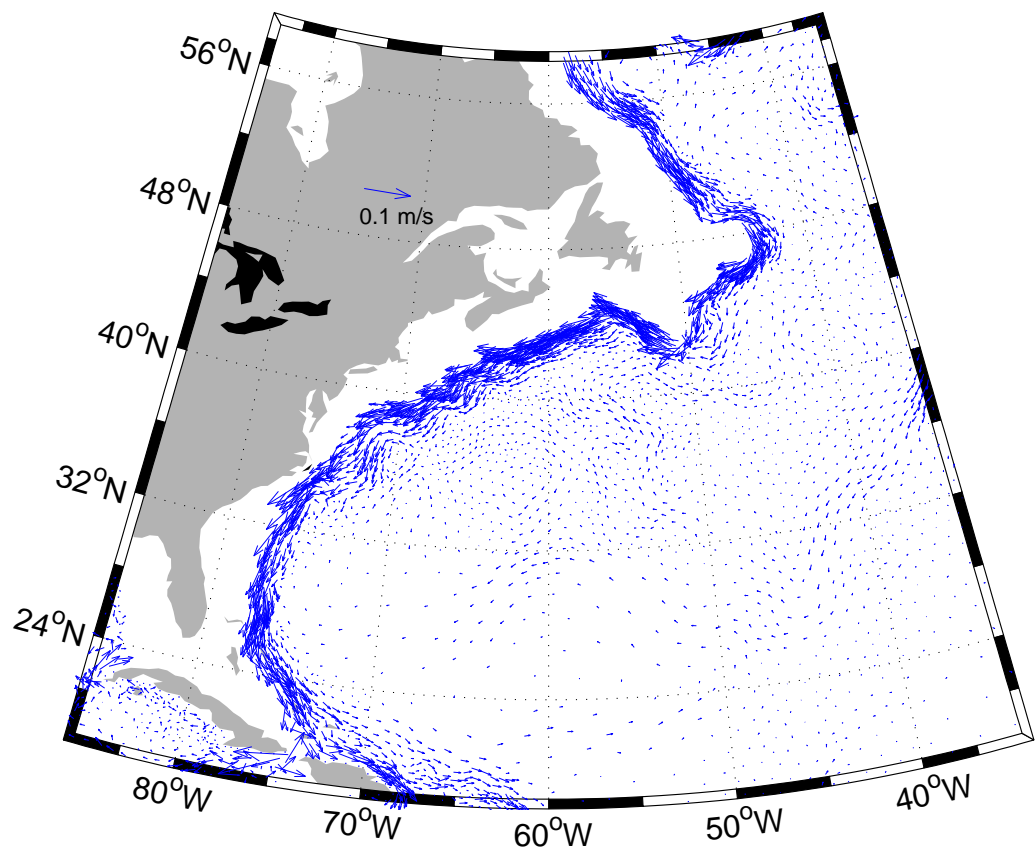


Figure 5.7: Velocities at 2000 m depth corresponding to the forward estimate. They are stronger while the Deep Western Boundary Current is more localized than in the case shown in Fig.5.3

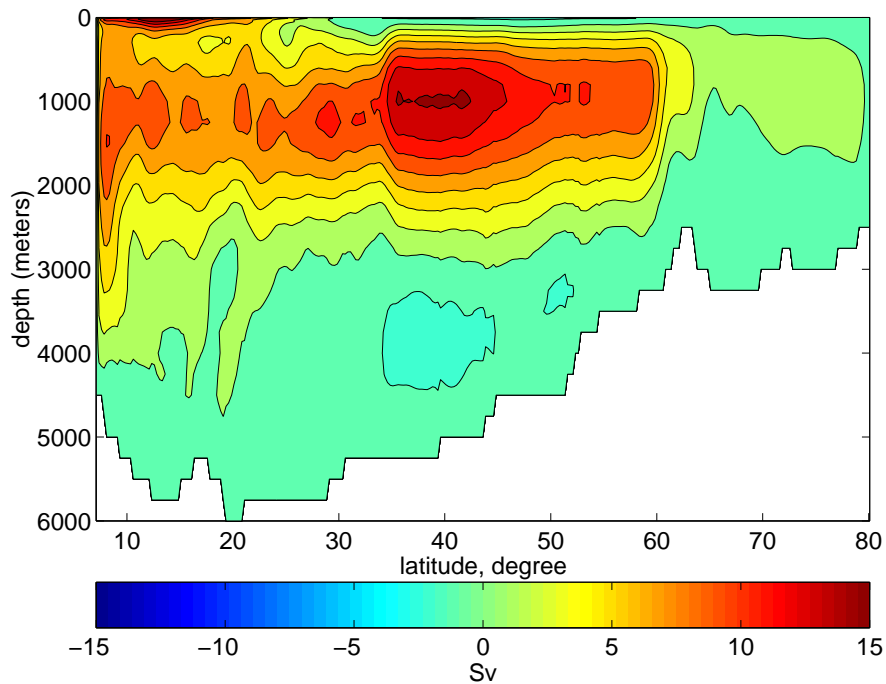


Figure 5.8: Meridional overturning streamfunction corresponding to the forward estimate. It shows basinwide overturning pattern with a maximum of 19 Sv. Contour interval is 2 Sv.

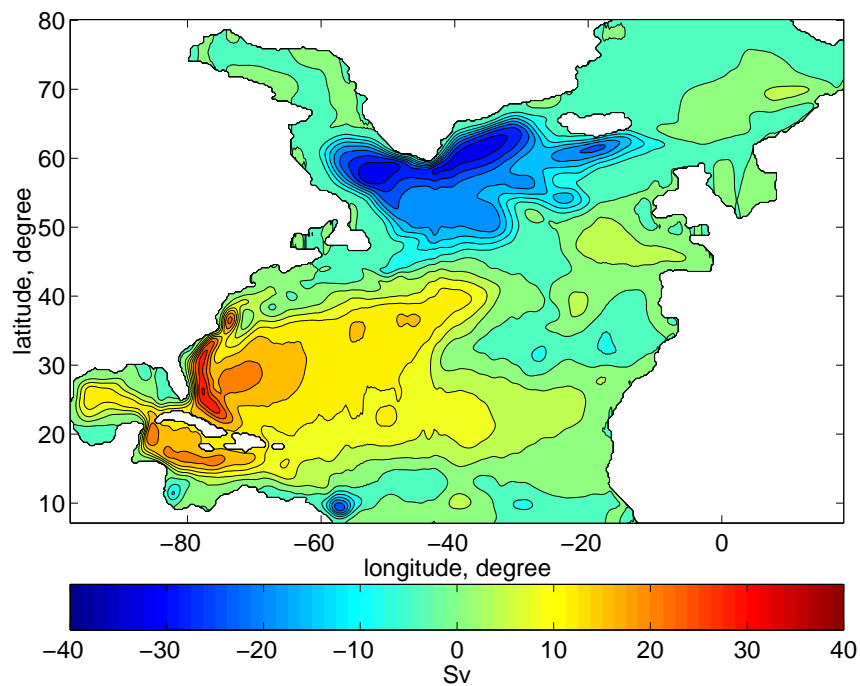


Figure 5.9: Barotropic streamfunction corresponding to the forward estimate. Contour interval is 4 Sv.

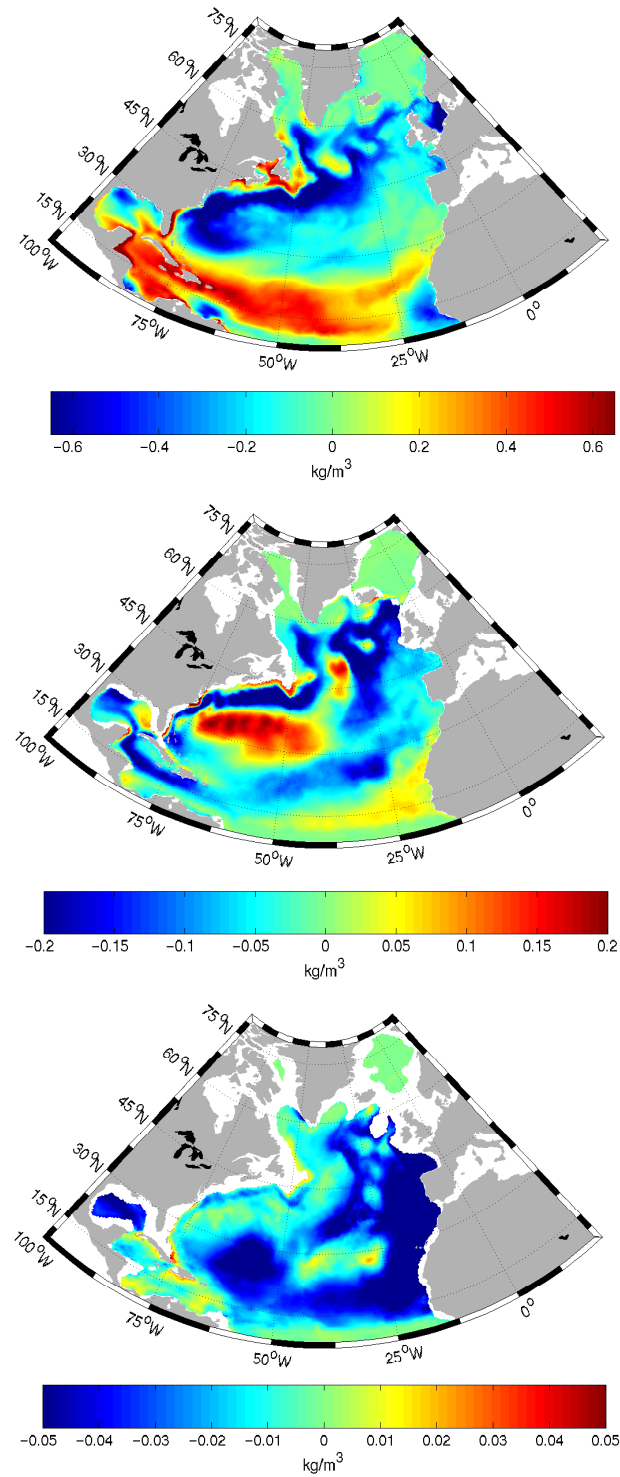


Figure 5.10: Difference between the forward estimate of the density field and the density computed from Levitus climatology at different depth layers. At 50 m depth on the upper panel, at 500 m on the middle panel and at 1500 m on the lower panel in kg/m<sup>3</sup>

## 5.4 Choosing weights

Choosing weights employed in the Cost Function (see section 4.2.2) is the key issue for the efficiency of the assimilation procedure, and this section discusses the weights used to construct the cost function in some detail. Although there are spatial correlations between residuals and data misfits at close locations, they are hardly known to us. Therefore in all our experiments we use a diagonal weighting scheme which requires only information on variances of the residuals and data misfits at a particular location. Correspondingly, for an element of any of the weight matrices  $\mathbf{W}$  introduced above we write

$$W_{ij} = \frac{V}{\sigma_i^2} \delta_{ij}.$$

No summation over repeating indices is implied here. In this expression,  $\sigma^2$  stands for variance of the particular quantity, and  $V$  is a ‘geometrical’ factor. There are two general ways of interpreting terms in the cost function, or equivalently choosing  $V$ : They can be treated as nodal quantities ( $V = 1$ , see, e.g., Yu and Malanotte-Rizzoli (1996)) or as volume-weighted quantities ( $V = \Delta V$ , where  $\Delta V$  is the volume of a cell associated to a node, see, e.g., Tziperman et al. (1992a,b)).

Due to the irregular grid structure of the IFEOM, the volume-weighted definition seems to be preferable to the nodal definition. However, the finite-element way of writing the model equations requires some attention here. As it was explained in section 4.1.2 (see formula (4.27)), the residuals in matrix equations are already defined as values weighted with the test function on clusters, which implies integration over the volume of the cluster. For instance, if residuals of the potential density equation were piece-wise constant on elements, the LHS vector of relation (4.32)  $\epsilon$  could be computed as

$$\epsilon_k = \frac{1}{3} \sum_{i=1}^{e_k} (r_i Vol_i), \quad (5.1)$$

where the factor of  $1/3$  comes from the integral of the test function over the volume, values  $e_k$  and  $Vol_i$ ,  $i = 1, \dots, e_k$  are the number of 3D elements which contain the node  $k$ , and their volumes respectively,  $r_i$ ,  $i = 1, \dots, e_k$  are the values of residuals of potential density equation on elements. Similar result will follow if the later residuals are linear on elements yet it will involve nodal values of residuals.

Thus we take the geometrical factor as the volume of cluster of elements having common node  $k$ . The variance of  $\epsilon_k$  scales as  $\sigma_{\epsilon_k}^2 \sim (\Delta V)^2 \sigma_{r_k}^2$  where  $\Delta V$  is the cluster volume and  $\sigma_{r_k}^2$  is the variance of the nodal density tendency.

This still leaves the question of choosing variances of the potential density tendency at nodes (see, e.g., the procedure of Tziperman et al. (1992b)). We expect that these variances are larger in the upper ocean and smaller in the

deep ocean, and also we assume that the larger the volume spanned by a cluster the smaller is uncertainty in  $r_k$ . The motivation here is rather simple. First, the vertical distance between the nodes is larger in the deeper ocean which results in larger cluster volumes. Second, the horizontal resolution of our grid is such that triangles are of small size in dynamically important regions where most changes are expected to happen, and uncertainties are the largest. This leads to the following plausible assumption  $\sigma_{r_k}^2 = \sigma_0^2 \Delta V_0 / \Delta V$ , with  $\Delta V_0$  some reference volume, and  $\sigma_0^2$  the constant value of variance estimated from a ten-year run of the FEOM at intermediate depths, and adjusted experimentally. The reference volume is irrelevant and is factored out of the cost function. The weighting scheme is then equivalent to weighting with squared volumes.

It is worth mentioning that the question how to correctly estimate the variance  $\sigma_{r_k}$  remains to a large extent open. A straightforward interpretation of  $\sigma_{r_k}$  as a measure for tendency in the density field at the particular point for a ‘hypothetical’ stationary ocean would require to take it much smaller than the interseasonal tendency. However, such interpretation could hardly be correct because the fluxes due to correlated fluctuations in density and velocity fields are discarded in our stationary model while they exist and play an essential role in reality.

The squared volume weighting introduced for the density tendency dictates the weighting scheme for the data term.

Generally, data is given at fixed locations which do not necessarily coincide with the grid points. The following strategy is adopted with respect to the data weighting.

If the model grid node coincides with the data point we form the weight to the difference between the data and model field by multiplying the inverse of data variance with the squared volume of cluster which corresponds to the grid point

$$W_{\rho_k} = \frac{1}{\sigma_{\rho_k}^2} \left( \sum_{i=1}^{e_k} Vol_i \right)^2. \quad (5.2)$$

If the data point is inside an element of the grid we first compute the model field at the data locations. It is easy to do since our model fields are piecewise linear functions on elements. Next, we follow the scheme of (5.2) using either the squared mean volume of all neighboring 3D elements or squared volume of the element containing the data point. We tried both schemes.

For the inversion of the Levitus climatology, the variance  $\sigma_{\rho_k}^2$  of  $\rho_k$  was estimated by the annual variability of the Levitus data (Levitus et al., 1994; Levitus and Boyer, 1994) in the upper layers and was set constant below some depth. In other cases, we used only  $z$ -dependent variance whose profile consist of linear part from the surface to 1000 m depth, and is constant in deep layers. We choose  $\sigma_{\rho_k} = 0.5 \text{ kg/m}^3$  at the surface and  $0.05 \text{ kg/m}^3$  at 1000 m and below. Our way of estimating variances departs from that used by Olbers et al. (1985); Tziperman et al. (1992b) who employed estimates of error variance of averaged

temperature and salinity (which lead to much smaller density errors close to the surface, but to comparable errors around 1000 m depth).

## 5.5 Experiment: Assimilation of Levitus Climatology

In the first experiment, we assimilate the in situ density computed from the Levitus atlas (Levitus et al., 1994; Levitus and Boyer, 1994). In the cost function, we keep only the terms which penalize the residuals in the equation for the potential density and constrain the model solution by the density data computed from the climatological temperature and salinity. The forward estimate described in section 5.3 is chosen as the first guess to start the optimization cycle. We use the mean wind stress for the period of 1950–99 as surface forcing.

The density field is computed as mean of the annual cycle and thus includes seasonal variations of hydrographic fields. Therefore the variance of climatological density entering the weights to the data term is estimated from the Levitus annual cycle. Since the climatological data are projected onto the model grid we employ the volume weighting in accordance with (5.2).

We should mention that we penalize separately the contributions from the diffusive and advective part in the residual term of potential density equation. This allows us to judge on the relative roles of both parts in the assimilation. Sometimes we increase the weight to the diffusive part so that it is comparable with data contributions. It is done for the regularization when the data are not smooth enough. This is not required for the Levitus data which are sufficiently smooth.

Fig. 5.11 shows the behavior of different contributions into the cost function during the optimization. They include the advection term of the equation for the potential density, the diffusion term and the data misfit (see the legend to the figure). The data term is decreasing most. It is obviously overweighted, however, this was needed to find a solution which approaches the data within standard deviation for density. The residual term is one order of magnitude smaller for the initial state than it was for the climatology analysis. After the minimization, it decreases almost one order of magnitude while the data misfit decreases almost two orders of magnitude. However, the integral properties of the optimized solution are not satisfactory and exhibit deficiencies similar to those of the analyzed velocity field, so we are not plotting them here. The meridional overturning streamfunction has the maximum cell of only 5 Sv. The subtropical gyre of the barotropic streamfunction is strongly displaced to the western coast while the horizontal velocity field of the optimal solution shows an artificial current along the eastern boundary going northward. This current starts at approximately 500 m depth and has a barotropic structure from this depth to the bottom.

We need to reject this solution. Changing the weights we were not able

to improve it significantly. In all runs with modified weighting the above mentioned features of the circulation developed already after several iterations of the minimizer. We conclude that using proper initialization cannot alone make assimilation of climatology successful. Some additional constraints are required.

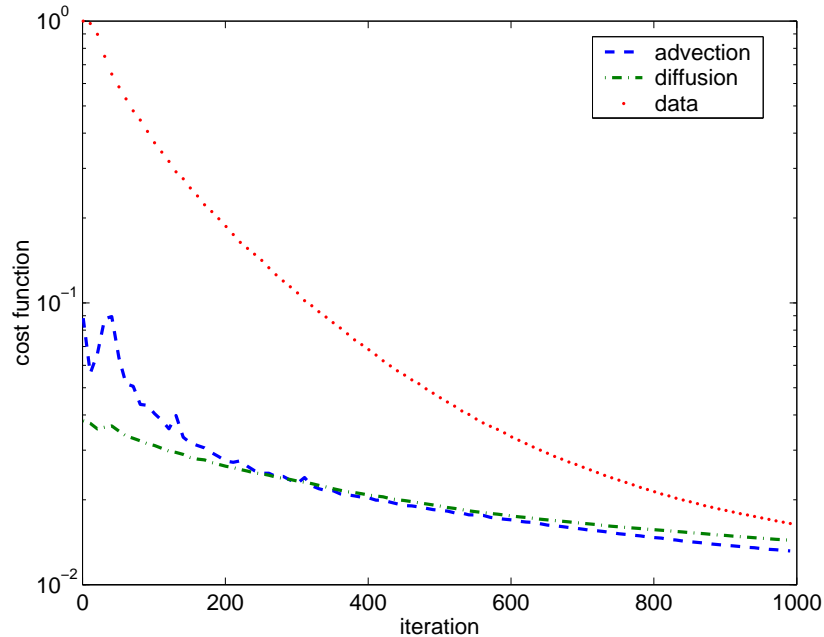


Figure 5.11: Evolution of contributions into the cost function in assimilation of WOA94 climatology starting from the forward estimate. The dot, dashed and dash-dot lines show the contributions from the departure of the model density from climatological density, the advection and the diffusion parts of the equation for the potential density, respectively.

## 5.6 Constraint on the deep pressure gradient

The inability to get a reasonable circulation pattern by applying the stationary inversion procedure is perhaps not surprising in the light of conclusions made by Tziperman et al. (1992b) and the indication of multiple local equilibria that follows from the results presented by Marotzke and Wunsch (1993). The question is, however, how to proceed. The recommendation of Marotzke (1992) and then by Tziperman et al. (1992a,b) is to impose the steadiness constraint by penalizing differences between the initial and final state separated by some *finite* interval of time. This is not a very cheap way to proceed as time intervals used for this purpose are from about half a year to five years, and many such time intervals are to be integrated with both forward and adjoint model in the process of minimization. The idea, therefore is, to try to understand what

is the difference between optimized Levitus and forward estimate circulations and design an additional constraint that would direct the solution in a ‘proper’ way.

To begin, let us return to the estimate of the circulation obtained from the forward model. Its circulation in the upper ocean does not fully match our a priori knowledge about the circulation in the North Atlantic. One of the examples is the Gulf Stream going far to the north, which is a feature shared with many other models of similar or even better resolution. Therefore we would not like to simply penalize the misfit between velocities of the forward and optimized solution. However we are satisfied with the integral properties of the forward estimate and with its deep ocean circulation showing a well-formed Deep Western Boundary Current. The deep circulation is driven by deep pressure gradients, and this suggests to compare the pattern of deep pressure anomalies in solutions discussed thus far. Figure 5.12 presents, from top to bottom, pressure anomalies at the depth 2000 m in the Levitus analyzed, Levitus optimized and the forward solutions. First we note that while the analyzed and optimized pressures differ slightly in the position and the strength of the DWBC, they share the common wrong feature close to the eastern coast. Both demonstrate the presence of northward current there, and optimization only strengthens it.

Further analysis shows that the minimization procedure is mostly acting through the changes in the barotropic velocity close to the eastern coast. Namely this destroys the integral properties of the circulation.

The deep pressure anomaly in the forward run (see the bottom panel of Fig. 5.12) differs essentially from analyzed and optimized pressures. It shows the noticeably narrower DWBC, and more important, there is no northward current along the eastern coast.

One would be interested in minimization that leaves deep ocean circulation intact while changing it (by adjusting density) in the upper ocean. The motivation here comes from recognizing the fact that the density field and, hence, the pressure field are dynamically consistent (with the velocity field) in the forward estimate (obtained by running FEOM over 10 years starting from the Levitus climatology) while they are not necessarily consistent in the analyzed and optimized *stationary* solutions.

In order to keep deep ocean pressure close to the forward estimate we introduce a constraint on the deep pressure gradient. We want the gradient of full pressure of the optimal solution be close to the one of the forward estimate over some range of depths

$$\nabla P + g\rho_0\nabla\zeta \rightarrow \nabla P_{fe} + g\rho_0\nabla\zeta_{fe}, \quad (5.3)$$

where  $P_{fe}$  and  $\zeta_{fe}$  are the hydrostatic pressure and sea surface height given by the forward estimate, respectively, and  $P$  and  $\zeta$  are those of the optimal solution,  $\rho_0$  is the mean density.

We use this weak constraint below 2000 m depth by adding a new term to the cost function  $\mathcal{J}$ :

$$\mathbf{J}_7 = \int_{\Omega} \int_{\Omega} (\nabla P + g\rho_0 \nabla \zeta - \nabla P_{fg} - g\rho_0 \nabla \zeta_{fg}) W_P(x, y, z, x'y'z') (\nabla P + g\rho_0 \nabla \zeta - \nabla P_{fg} - g\rho_0 \nabla \zeta_{fg}) d\Omega d\Omega' \quad (5.4)$$

The weights are set to zero above 2000 m. Thus we allow the upper ocean (above 2000 m) to change while keeping the lower ocean circulation close to the forward estimate.

In order to see how much we should displace the structure of the density field from the climatology in order to approach the forward estimate pressure we plot in Fig.5.13 the difference

$$\frac{(P_{fe} + g\rho_0 \zeta_{fe} - P_L - g\rho_0 \zeta_L)}{g\rho_0}, \quad (5.5)$$

at the depth of 2000 m. Here  $P_L$  is the hydrostatic pressure computed from the Levitus climatology,  $\zeta_L$  is the sea surface height elevation which corresponds to Levitus climatology analysis (see section 5.2).

Figure 5.13 shows that along the DWBC the change in  $\zeta_L$  of approximately 0.1 m is required in order to have pressure gradient equal to the forward estimate at 2000 m depth. This corresponds to approximately 0.05 kg/m<sup>3</sup> change in the density over upper 2000 m or 1 kg/m<sup>3</sup> if the change in density occurs only in the upper 100 m. Obviously, those changes are pretty big and would not always let us approach the data within standard deviations.

We should mention that the gradient of pressure is computed in finite element sense, i.e. its values at nodes are weighted with the test function over element clusters

$$\nabla P + g\rho_0 \nabla \zeta \rightarrow \int_{\Omega} (\nabla P + g\rho_0 \nabla \zeta) \tilde{\mathbf{u}} d\Omega. \quad (5.6)$$

This form of defining the pressure gradient is consistent with the definition of other terms which are included into the cost function (see section 5.4). Similar to weighting the residuals of potential density equation, we assume that volume weighting is sufficient to mask information on variance of the deep pressure gradient at all locations when defining its weights and take the same variance everywhere. Its magnitude is estimated by evaluating gradients of the difference shown in Fig. 5.13.

In the following chapters we conduct assimilation of different climatologies using constraint on the deep pressure gradient (see table 5.1).

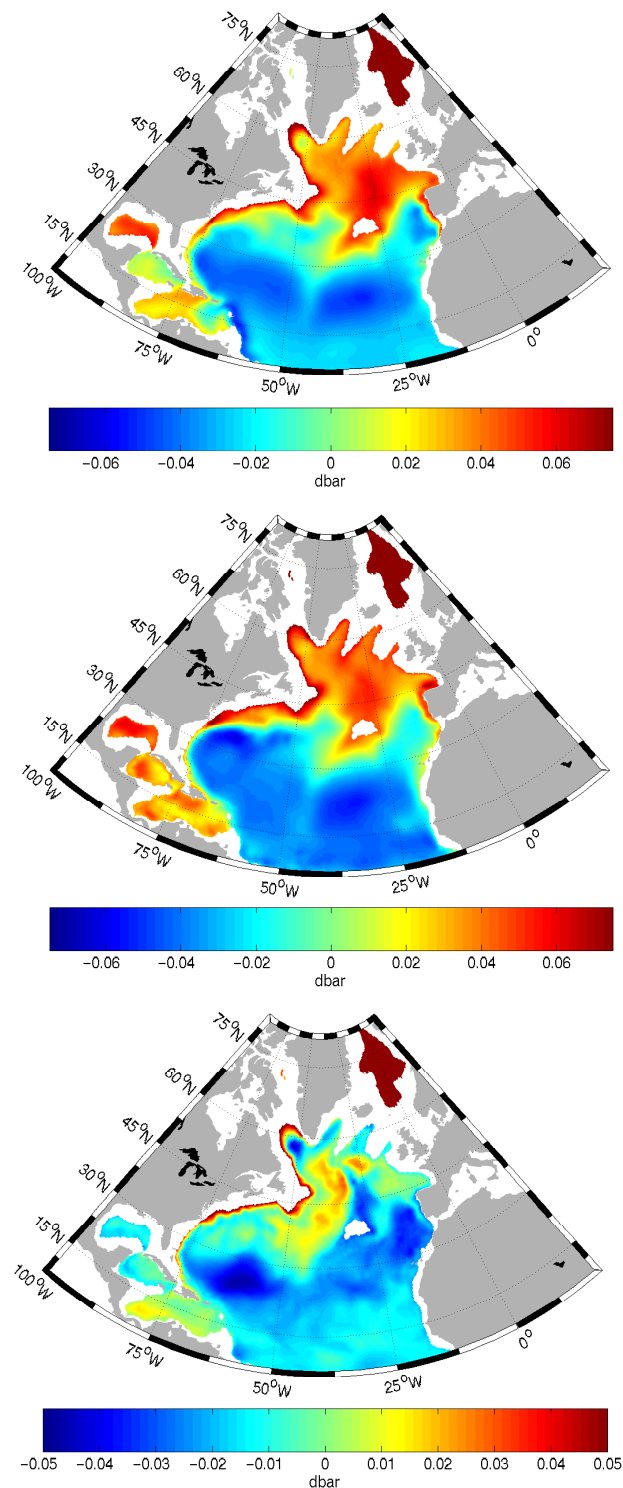


Figure 5.12: Pressure anomalies at 2000 m depth corresponding to the diagnostic of the Levitus climatology (upper panel), to the optimized solution based on Levitus data (section 5.5 (second panel) and to the forward estimate (lower panel).

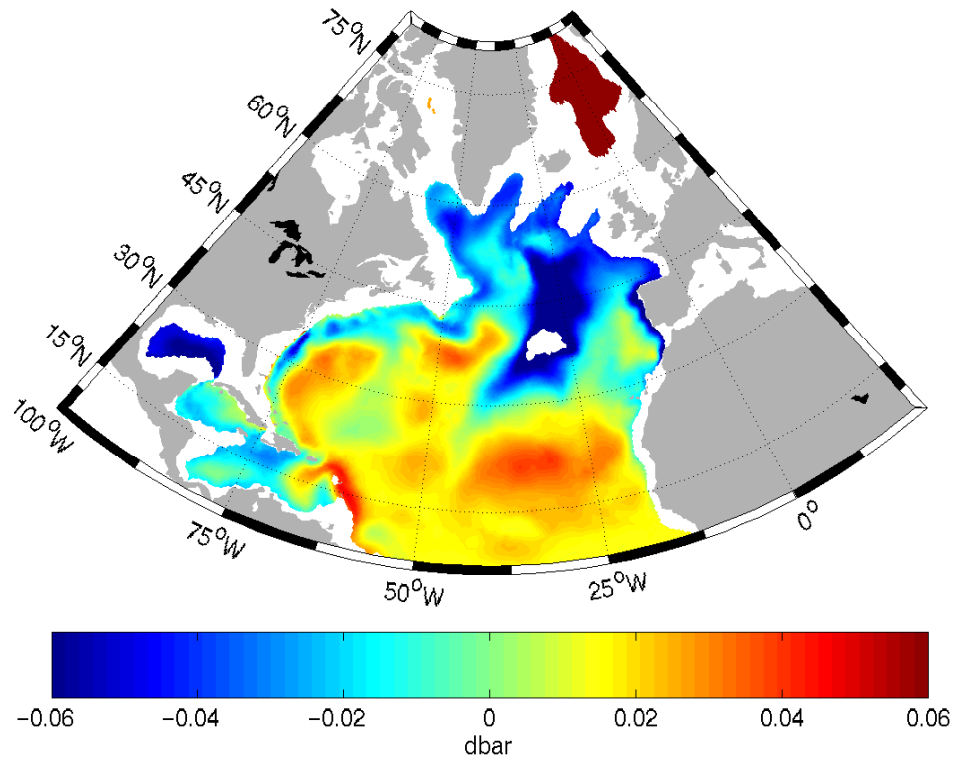


Figure 5.13: The residual SSH which must be added to  $\zeta_{lev}$  in order to have the full pressure at 2000 m depth equal to one from the forward estimate.

## 5.7 Experiment: LEV

In the next experiment we assimilate climatological fields using the deep pressure gradient constraint. As a starting point for minimization we take a synthetic density field which is combined from the forward estimate and Levitus climatology  $\rho = (\rho_{fe} + \rho_{atl})/2$ . This gives non zero values to the costs of the deep pressure gradient and data at the first iteration and decreases the number of iterations needed to find the optimal solution compared to starting from the forward estimate or climatology. However, opposite to the previous case, we see very little difference in the solutions when starting from different initial states (provided the number of iterations of the minimization procedure is sufficiently high, i.e. more than 5000). This is a consequence of introducing the new constraint which strongly reduces the number of local minima of the cost function.

However, in order to resolve small scale features of the circulation we found that it was necessary to make large number of iterations. Typically, for the problem of the size considered here, it takes 5000 iterations to get a satisfactory solution. 4D VAR models of similar resolution cannot afford that large

Experiment	Data	Wind Stress (NCEP Reanalysis)
LEV	WOA94	mean for 1950–1994
LOZ	Lozier et al. (1995) mean for 1950–1994	mean for 1950–1994
LOZXX-XX	separate pentades	corresponding to the period of a pentade
GUR	Gouretski and Koltermann (2004)	mean for 1950–1994

Table 5.1: Experiment design

number of simulations and are often limited by the numbers below one hundred (Stammer et al., 2002).

It is worth mentioning that weighting the model–data misfits with volumes is crucial for making the assimilation consistent. Assimilation with the misfits defined at nodes would have led to the biggest changes in density occurring in the deep ocean because it reduces the deep pressure gradient cost most efficiently. This is a consequence of coarsening the vertical grid resolution with the depth. The change in density at any deep node affects the deep pressure more than the change of density at any of upper nodes.

The variance of the density estimated from the Levitus annual cycle is the largest in the region of Gulf Stream. This explains why the biggest changes occur there during the assimilation. These changes do not let details in neighboring regions which we know from the other models and observations be resolved. For instance, the Labrador current does not penetrate far enough to the south in the solution found. That is why we did one more run to assimilate the Levitus climatology where we took the same weights to all the costs except the data.

We assume that the variances of the data vary only in the vertical direction and decrease ten times with the depth from the surface to 1000m. The value at 1000m depth is continued further down to the bottom (see section 5.4). The weights to the data are taken as inverse of these variances multiplied with volumes of corresponding clusters (see section 5.4). Both experiments result in circulations with very similar integral properties with the difference between them in only small details.

The behavior of different parts of the cost function is shown in Fig. 5.14. Once again, the data term (the dotted line) dominates, and continues to slowly decrease after 2000 iterations. The advection term is also decreasing while the deep pressure gradient contribution is nearly stationary indicating that the deep part of the circulation remains nearly intact during assimilation.

The optimal solution matches our a priori knowledge about circulation in the North Atlantic. The Gulf Stream separates at about 35 °N and is not going that far to north as it does in a forward run solution, however the DWBC is similar to that of the forward model (Fig.5.7). The circulation results in the

meridional overturning cell of about 12 Sv (Fig.5.15). The barotropic stream-function shows big structures of subtropical and subpolar gyres (Fig.5.16) with the Gulf Stream taking away about 40 Sv of water from the western coast.

The differences between the optimal density and the climatological density are presented in Fig. 5.17 for depths of 50, 500 and 1500 m respectively. The difference is less than  $0.5 \text{ kg/m}^3$  at 50 m depth in the Gulf Stream region where standard deviations computed from the Levitus annual cycle are of about  $0.6 \text{ kg/m}^3$  (cf. Fig. 5.17, 5.6). The maximum difference at 500 m exceeds  $0.04 \text{ kg/m}^3$  and at 1500 m depth slightly exceeds the estimated standard deviations (cf. Fig. 5.17, 5.6).

From the differences between the optimized solution and the Levitus climatology we see that optimization tends to reduce the eastward component of the density gradient in the middle of the basin, however tends to localize it closer to the western coastline in order to resolve the DWBC similar to the forward estimate.

We accept this solution and will be using it for comparison further.

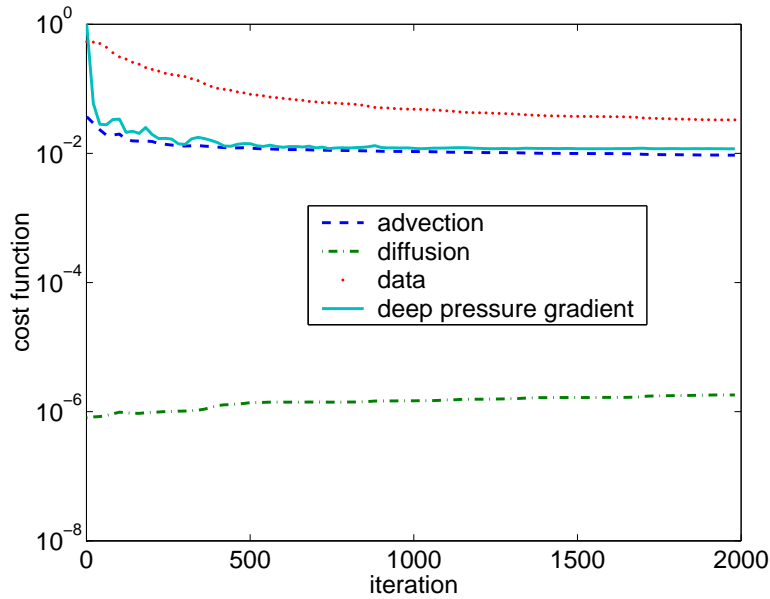


Figure 5.14: Evolution of contributions into the cost function **LEV**. The solid, dotted, dashed and dash-dotted lines show, respectively, the cost of the deep pressure gradient constraint, the misfit between the model density and climatological data, and the advection and diffusion parts of the equation for the potential density.

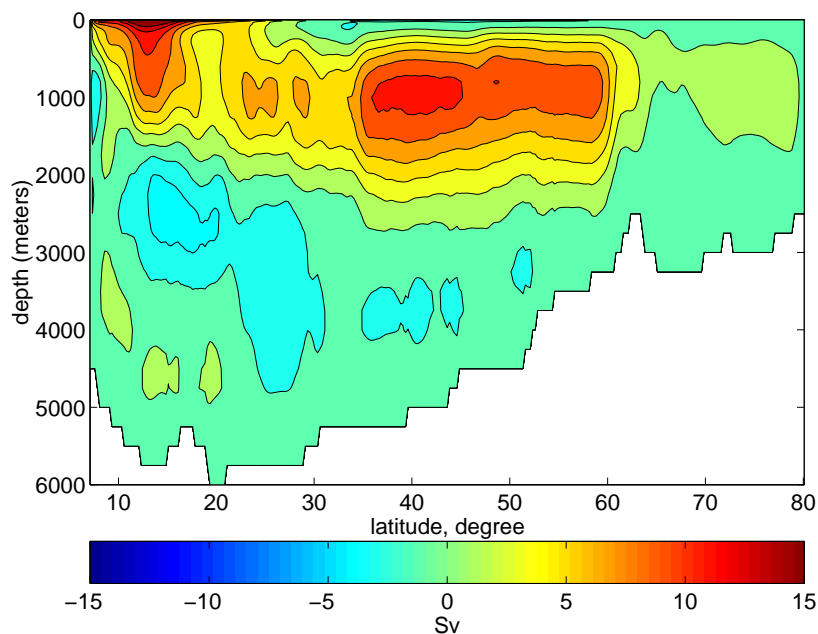


Figure 5.15: Meridional overturning streamfunction corresponding to **LEV** solution. Its main cell has a maximum of 12 Sv. Contour interval is 2 Sv.

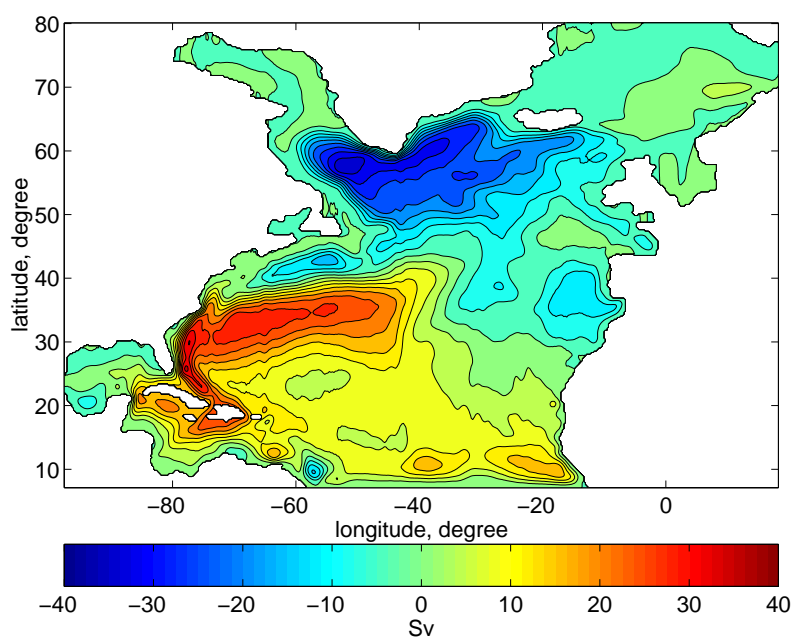


Figure 5.16: Barotropic streamfunction corresponding to **LEV** solution. Contour interval is 4 Sv.

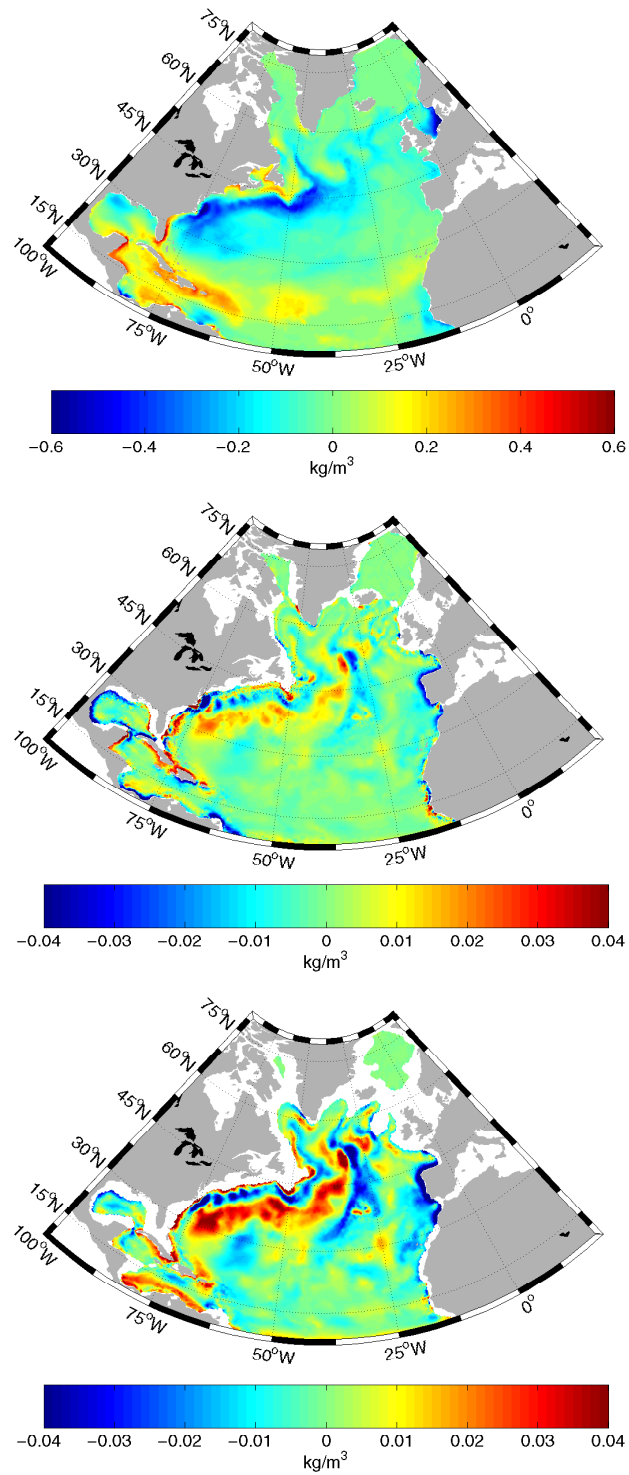


Figure 5.17: Difference between the **LEV** density and the density computed from WOA94 climatology at different depth levels. At 50 m depth on the upper panel, at 500 m on the middle panel and at 1500 m on the lower panel in kg/m<sup>3</sup>

## 5.8 Experiment: LOZ

In the following experiments we construct the set of inverse solutions for the nine pentades of Lozier data (Lozier et al., 1995) for 1950-1994. To start the assimilation we first project the data onto the model grid. This preprocessing extremely decreases the time needed for the optimization.

The data do not cover the whole model domain. For instance, they do not reach the western coast in the region of Gulf Stream and thus do not describe the tongue of cold water which flows along the U.S. coast after leaving the Labrador Sea. The data set is also not complete in the north, where we do not have the data north of  $70^\circ$ .

However, we do not extrapolate the data onto the model grid giving the possibility to the model to complete the data in a dynamically consistent way.

The cost function is constructed by analogy with the previous experiment (see section 5.7). We use the same constraints and the same weights to all contributions to the cost function.

First we assimilate the mean Lozier data for the period from 1950-1994. We start from the same starting point for the minimizer as in the previous experiment.

The circulation fields derived from the optimal solution for the mean Lozier data reproduce the most known features of the North Atlantic circulation (see Fig. 5.23). We see the continuation of the Labrador Current which goes to  $40^\circ\text{N}$  along the coast turning then south and merging the Gulf Stream. This is a very striking result (given the absence of data over this area) showing that the model ‘extrapolates’ the data in a dynamically consistent way (see Fig. 5.19). The corresponding sea surface height in this region is presented in Fig. 5.18. It shows a depression in the SSH which is a feature of circulation there.

The Gulf Stream leaves the western coast as a broad current and we see the strong North Atlantic current. The deep ocean circulation looks similar to the forward estimate. The circulation which corresponds to the mean Lozier hydrography results in the meridional overturning cell of about 14 Sv.

We approach the mean Lozier density within the standard deviation estimated from the interannual pentadal variability. The difference between the optimized model solution and data reaches  $0.5 \text{ kg/m}^3$  in the upper layers and decreases with the depth reaching  $0.03 \text{ kg/m}^3$  at 1500 m. In the deep ocean, it is even smaller. The differences between the optimized model solution for mean Lozier and data are shown for the depths of 50, 100 and 1500 m in Fig. 5.20.

The minimization tends to reduce the eastward component of the density gradient in the middle of the basin, similar to the previous experiment. Clearly, it reproduces this gradient along the continental break which results in the DWBC resolved by the model. However it is not visible at the western coast in the differences between the optimized density and Lozier data to the extent it is present in **LEV** experiment. This is due to the fact that the dataset is not

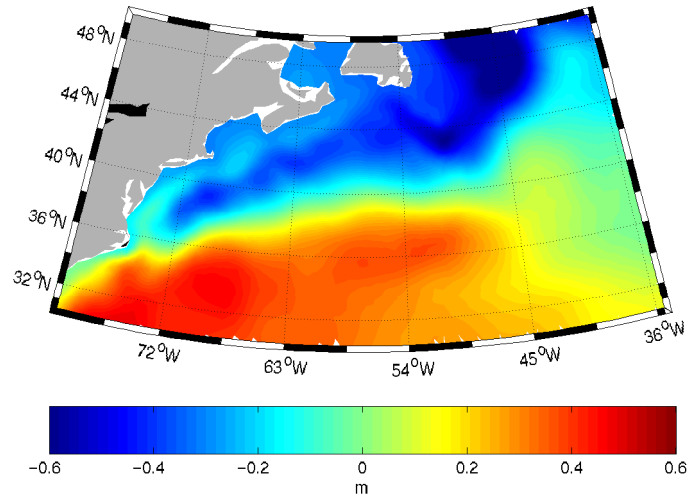


Figure 5.18: Sea surface height in the Gulf Stream region corresponding to the **LOZ** solution. The tongue close to the western coast corresponds to the Labrador water flowing in the south–west direction. The data are absent in this area. This demonstrates that optimizations completes the dataset in a dynamically consistent way.

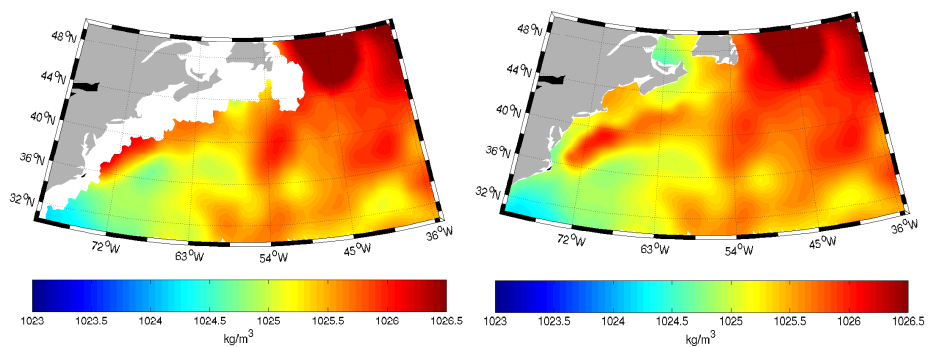


Figure 5.19: The density computed from the dataset of Lozier et al. (1995) as a mean of nine pentades (left panel) and the corresponding optimized solution of IFEOM (right panel) in the region of Gulf Stream at 10 meters depth.

complete in this region. Thus we may conclude once more that optimization extrapolates the data in a dynamically consistent way.

Having assimilated the mean Lozier data we assimilated each of the nine pentades separately. The forward model was forced by the mean wind stress for the period corresponding to a pentade if a pentade is assimilated. In order to speed up the assimilation, we use the assimilated mean Lozier data as the starting point for all nine pentades. The IFEOM is able to take into account differences between pentades even existing at relatively small scales. Figure 5.21 gives an example showing the skill of the IFEOM in reproducing the pentadal anomalies. Its left panel shows the difference in density data between the pentades 1990-1994 and 1985-1989. Its right panel shows the corresponding difference in the density between optimized solutions. The rows of Fig. 5.21 correspond to depths of 100, 500 and 1000 meters from top to bottom. The anomalies shown in left and right panels nearly coincide in shape and magnitude thus proving that we can study the variability of the North Atlantic circulation from the sequence of inverse solutions.

The variability derived from the pentades is discussed in section 5.12.

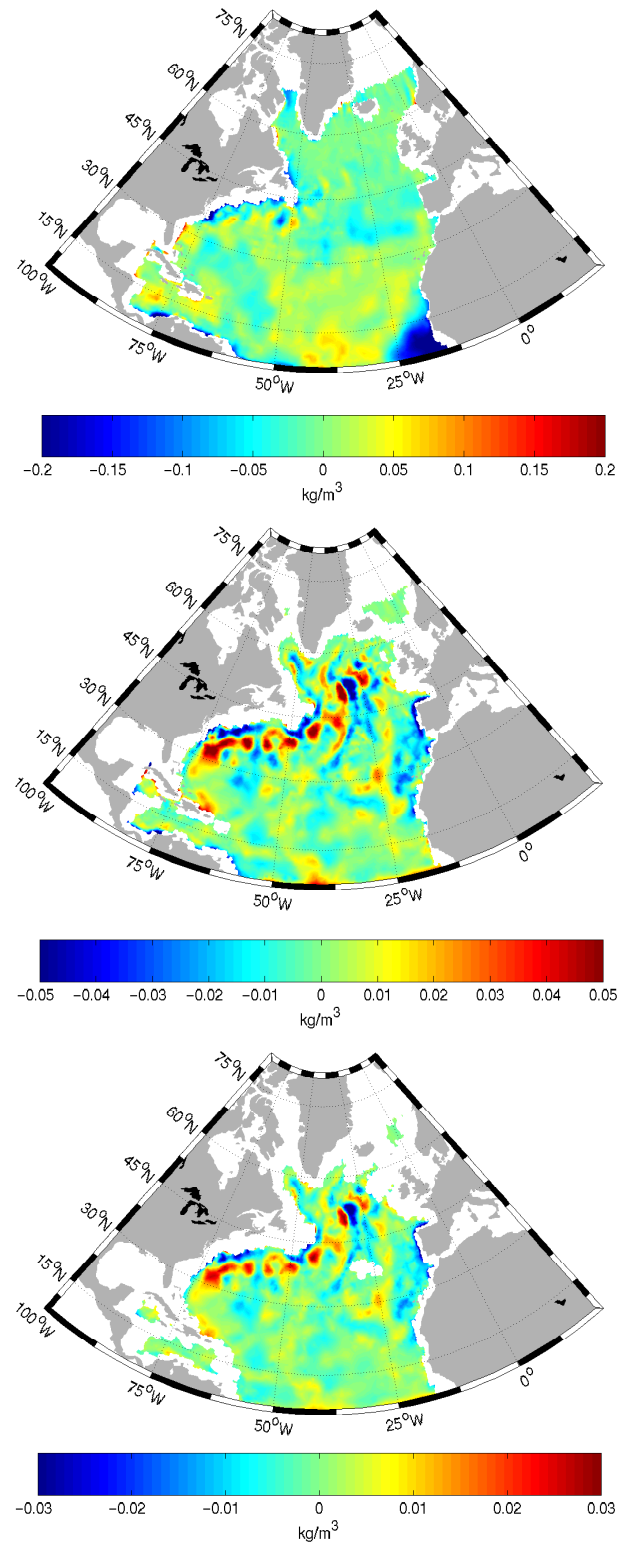


Figure 5.20: Difference between the density field which corresponds to **LOZ** solution and the density computed from the mean Lozier hydrography at different depth levels. At 50 m depth on the upper panel, at 500 m on the middle panel and at 1500 m on the lower panel in  $\text{kg/m}^3$

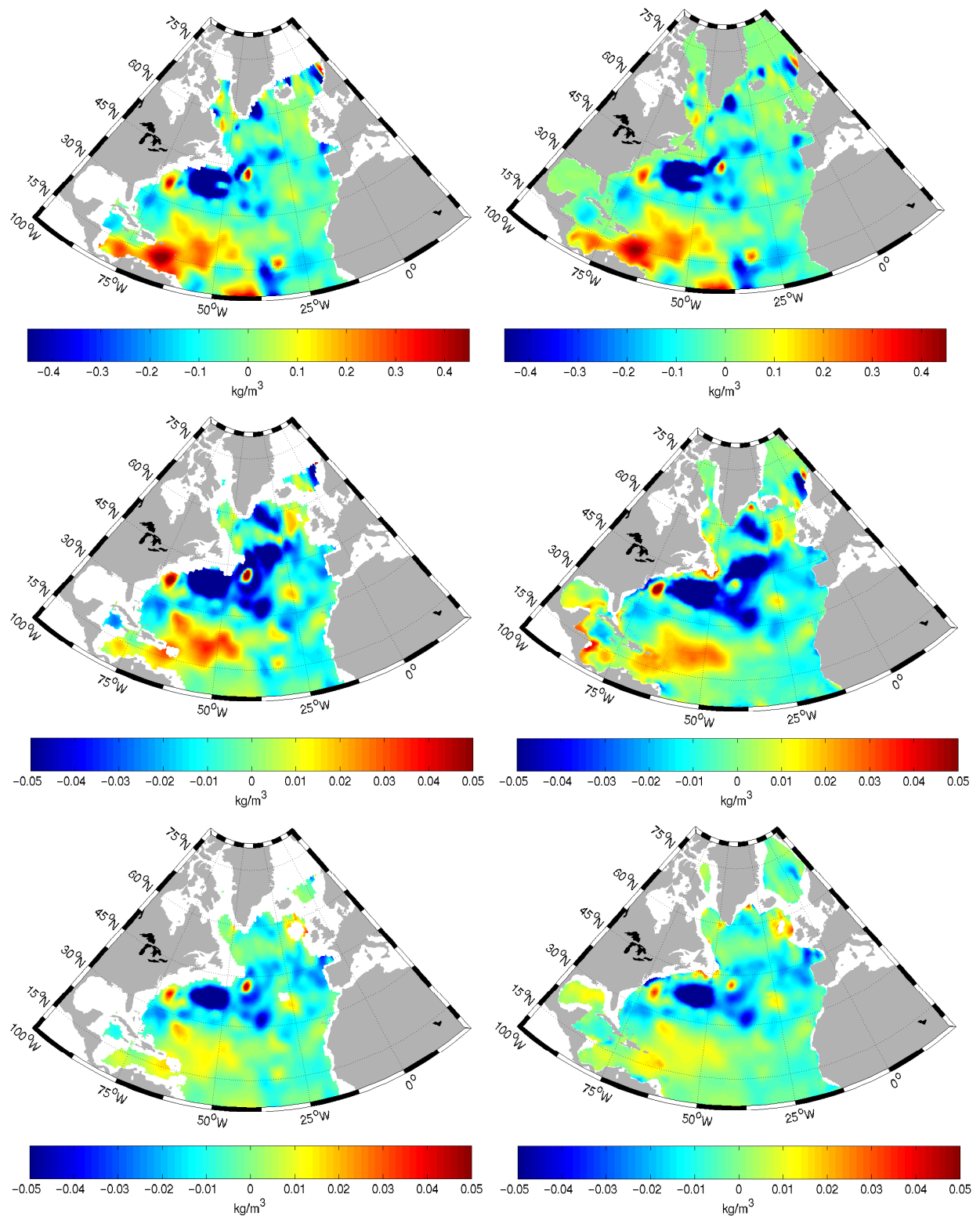


Figure 5.21: Density anomalies between the the data (left panels) and between the inverse solutions (right panel) for the last pentade (1990-1994) and the one before last (1985-1989). They are shown at different depth levels: at 100 m depth on the upper panels, at 500 m on the middle panels and at 1000 m on the lower panels in  $\text{kg/m}^3$

## 5.9 Remark on the velocity field

Before analyzing velocity fields which correspond to our optimal solutions we can make a brief comment on them. While their Gulf Stream is displaced seaward (consistent with data) compared to the forward estimate, they all still show a recirculation close to the western coast between about  $36^{\circ}N$  and  $40^{\circ}N$  (see Fig.5.23).

This is one of the most problematic regions for numerical models, and sometimes the error in presenting the bottom topography (among other factors) is blamed to cause the problems. The prognostic models at eddy permitting resolution usually shift the Gulf Stream to the western coast and it penetrates far to the north like in the FEOM forward run (see section 5.3). Assimilating data displaces the Gulf Stream to the appropriate location but makes it unrealistically broad because climatological data are excessively smooth.

Eden and Greatbatch (2003) used a semiprognostic model where they combined the model density with climatological density at each time step before computing pressure to improve the circulation in a number of locations including the Gulf Stream. This, however, ‘repairs’ the solution in a way similar to ours, as follows from Fig. 5.22 adopted from the paper by Eden and Greatbatch (2003). The semiprognostic solution is characterized by smooth and broad Gulf Stream yet retains some tendency to forming recirculation past Cape Hatteras.

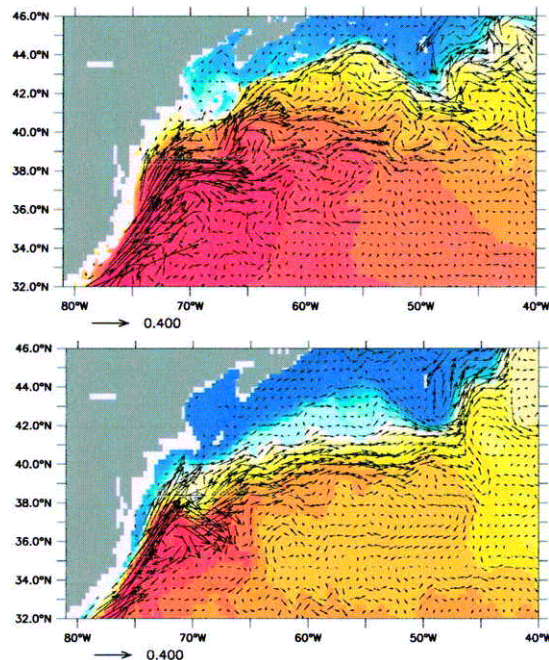


Figure 5.22: The three year mean velocity at 100 m depth for a prognostic  $1/12^{\circ}$  model (upper panel) and semiprognostic  $1/3^{\circ}$  model (lower panel). After Eden and Greatbatch (2003).

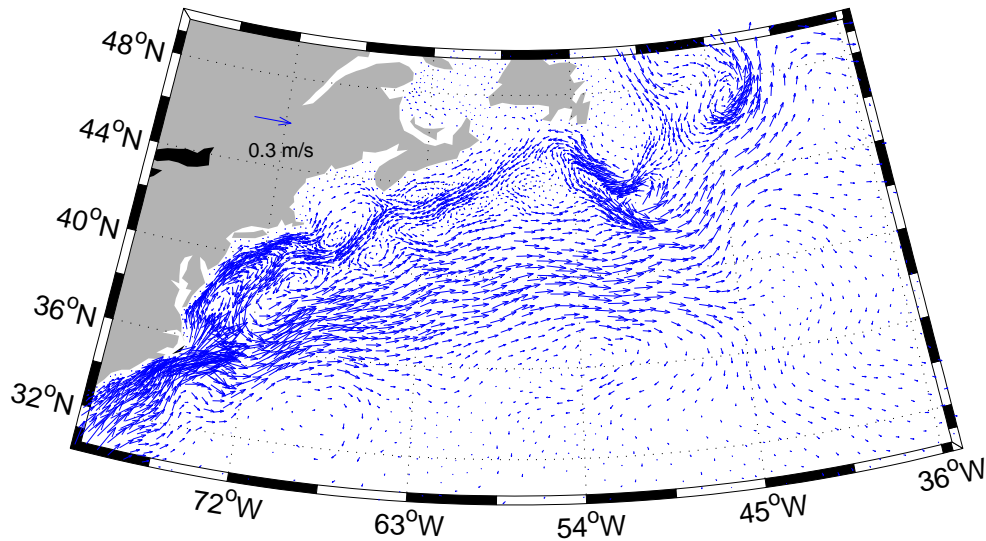


Figure 5.23: Velocity field corresponding to the optimized mean Lozier dataset at 100 m depth.

## 5.10 Experiment: GUR

In this experiment, we analyze climatological data of Gouretski and Koltermann (2004) described in section 2.1. To be consistent with previous experiments we choose the same weights for contributions in the cost function as in experiments **LEV** and **LOZ**. However, to reduce the number of iterations, the solution from **LOZ** experiment based on the mean Lozier data is taken as the starting point for the minimizer (the circulation that corresponds to this solution has acceptable integral properties). Yet, already in the first step of the minimization one finds that there is noticeable difference between the Lozier and Gouretski data because the data cost makes the biggest contribution into the cost function. The behavior of different parts of the cost function over first 3000 (from the total 5000) iterations is shown in Fig. 5.24. According to Fig. 5.24, the optimization tends to slightly increase the costs of the advection, diffusion and the deep pressure but simultaneously strongly reduces the cost of the data misfit (by more than one order of magnitude). Despite some increase in the deep pressure cost, the meridional overturning streamfunction shown on Fig. 5.27 reaches about 14.5 Sv at maximum which exceeds that of any of assimilated pentades of Lozier, and of Levitus datasets.

The difference between the optimized model solution and the data is shown in Fig. 5.26. It is small over the upper layers. At 50 m depth, it does not exceed  $0.2 \text{ kg/m}^3$  almost everywhere. However, the difference is relatively large to the north of Greenland. The data contain a big spot there with density being noticeably smaller than in the surrounding area. It cannot be dynam-

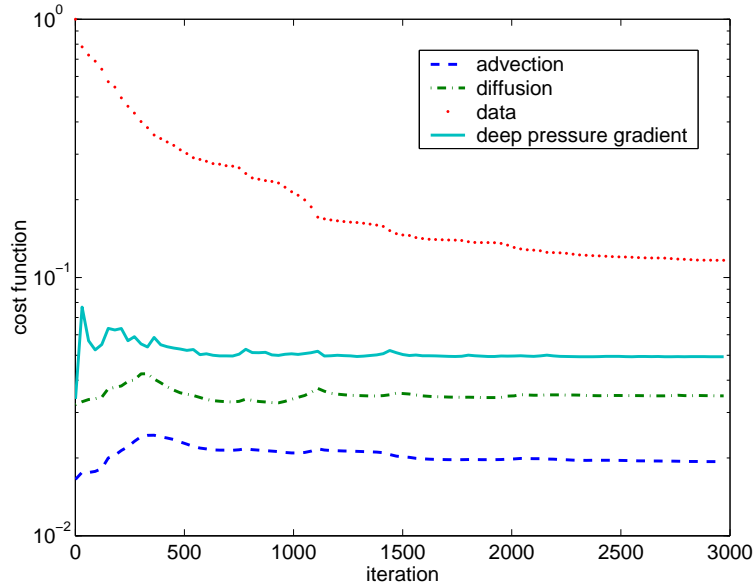


Figure 5.24: Evolution of contributions into the cost function in **GUR** experiment. The solid, dot, dashed and dash-dot lines show, respectively, the cost of the deep pressure gradient constraint, the misfit between the model density and climatological data, and the advection and diffusion parts of the equation for the potential density.

ically consistent and is not approached by the solution. In the deeper layers (around 500 m), the density difference decreases to  $0.04 \text{ kg/m}^3$  remaining, however, slightly larger than the differences over the same depths for the **LOZ** experiment. This tells us that the minimizer does not allow the deep pressure cost to increase by controlling the density in these layers rather than in the upper ocean. However, in the deep ocean the difference between the data and solution becomes small again. Already at 1500 m depth, it does not exceed  $0.04 \text{ kg/m}^3$  and appears to be even smaller than in the previous experiments.

As opposite to the **LOZ** experiment, the dataset of Gouretski and Koltermann (2004) covers the whole domain of the North Atlantic. It reproduces the tongue with increased density along the western US coast which we discussed in the previous section.

The IFEOM does not ‘extrapolate’ the density field in this case. The presence of the density tongue in the data enforces the same feature in the solution. The density tongue turns to be much sharper than in experiments discussed previously. This results in SSH with much sharper gradients than those of **LOZ** and **LOZ** solutions. The resulting SSH in the Gulf Stream region is shown in Fig. 5.25. Correspondingly, the Gulf Stream separation shown in Fig. 5.29 is at about  $35^\circ \text{N}$  (the latitude of Cape Hatteras) and we do not see the bias recirculation present in the other solutions in the region where the coastline turns westward past the separation point, see section 5.9.

This could be interpreted as the dataset of Gouretski and Koltermann (2004) being more complete and ‘dynamically’ consistent than other climatologies in the Gulf Stream region over upper layers. The absence of the artificial recirculation in **GUR** solution and its presence in both **LOZ** and **LEV** solutions is also the result of the fact that the solution in **GUR** experiment approaches the data in the upper layers much better than in the other runs.

The barotropic streamfunction computed for the solution of experiment **GUR** is plotted in Fig. 5.28. It shows better expressed subtropical and subpolar gyres than results of **LOZ** and **LEV** experiments.

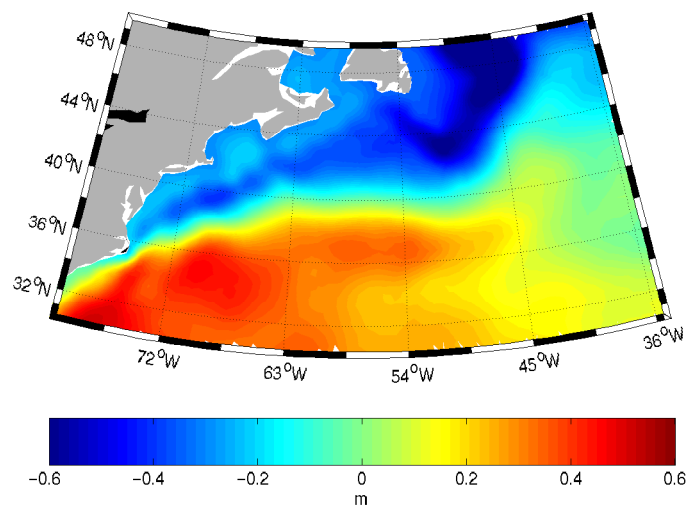


Figure 5.25: Sea surface height in the Gulf Stream region derived from **GUR** solution. The tongue with increased density close to the western coast corresponds to the Labrador water flowing in the south–west direction. It has sharper gradient than in **LOZ** and **LEV** experiments which projects into more realistic flow in the region of the Gulf Stream separation.

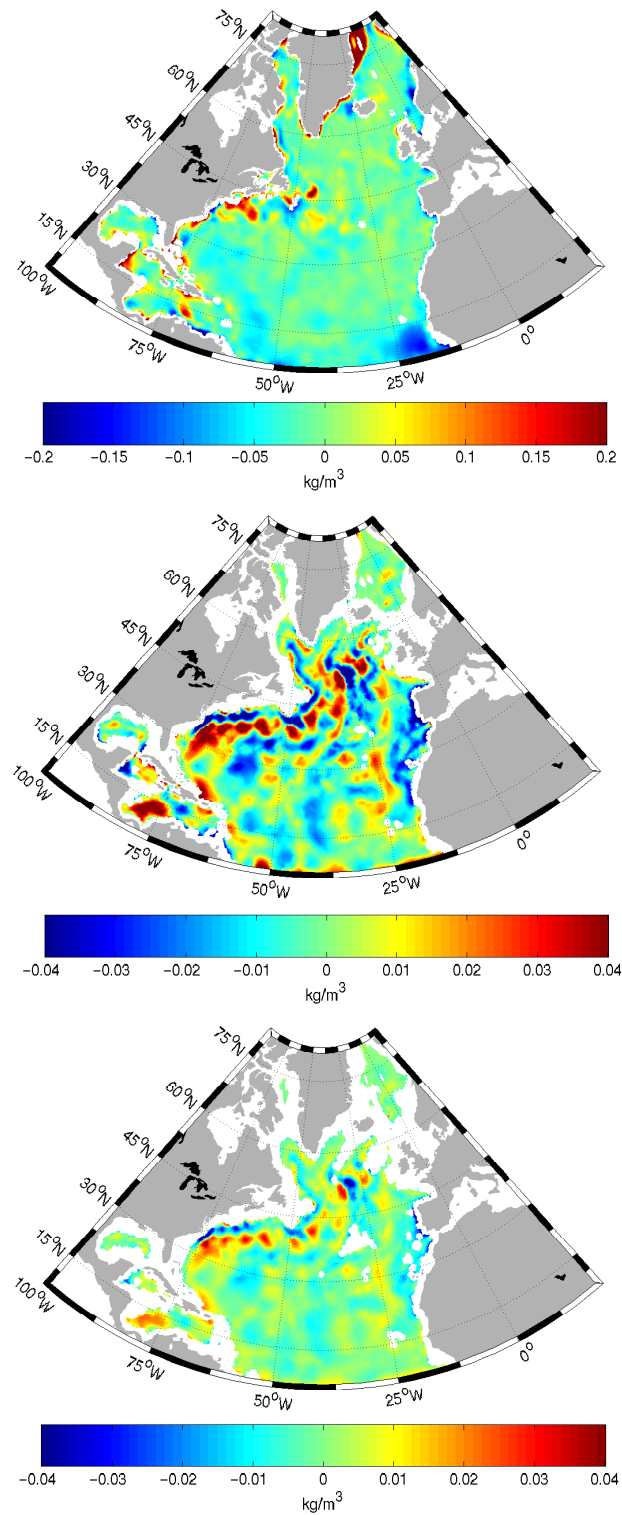


Figure 5.26: The difference between the densities of the **GUR** solution and climatology of Gouretski and Koltermann (2004) at 50 m depth (upper panel), 500 m (middle panel), and 1500 m (lower panel), in  $\text{kg/m}^3$ .

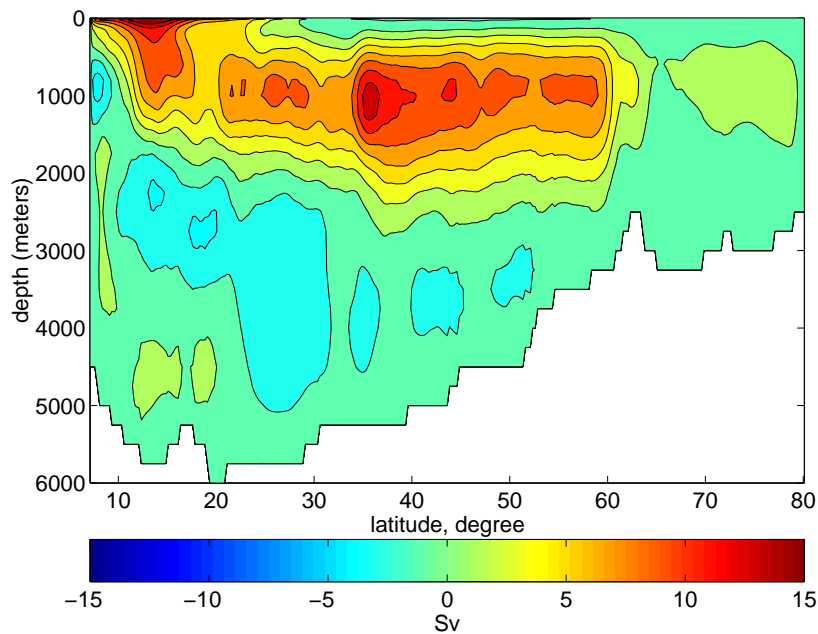


Figure 5.27: Meridional overturning streamfunction of the optimal solution from experiment **GUR**. Its main cell has a maximum of 14.5 Sv. Contour interval is 2 Sv.

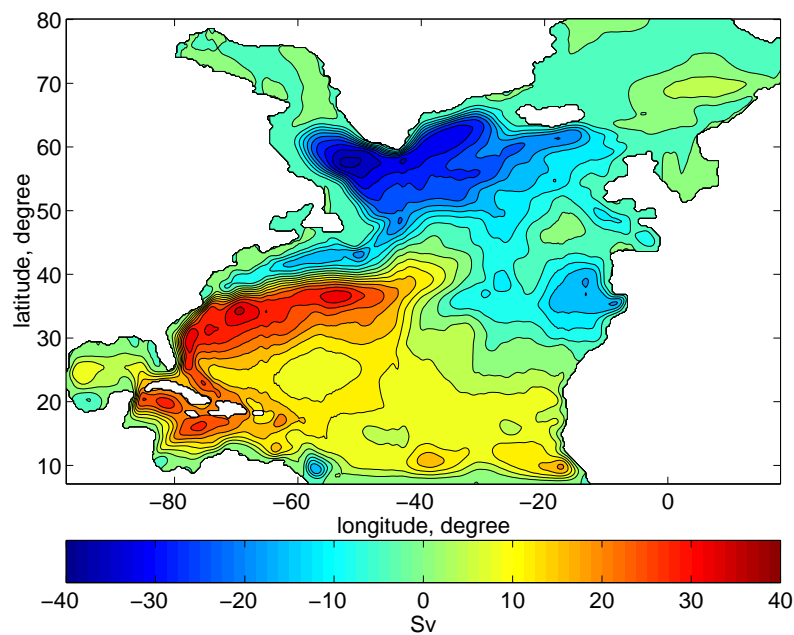


Figure 5.28: Barotropic streamfunction corresponding to the optimal solution from experiment **GUR**. Contour interval is 4 Sv.

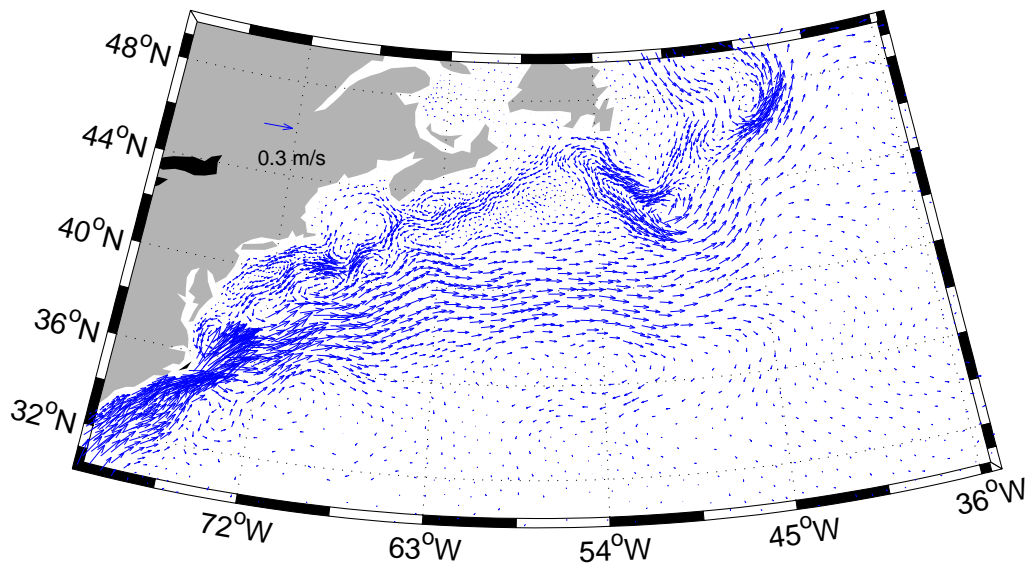


Figure 5.29: Velocity field corresponding to the optimized solution in experiment **GUR** at 100 m depth. It does not contain the recirculation west to the Gulf Stream separation zone. It proves that the dataset of Gouretski and Koltermann (2004) is more dynamically consistent in this area than those analyzed in **LOZ** and **LEV** experiments.

## 5.11 Transports

In order to validate the model performance we analyze several sections across the model domain shown in Fig. 5.30 and compare transports across them to other recent estimates available. These include the results presented by Lumpkin and Speer (2003) on the large-scale circulation in the North Atlantic, the work by Fischer et al. (2004) on the boundary circulation at the exit of the Labrador Sea, the results for the western exit of the subpolar North Atlantic by Schott et al. (2004), the work by Schiller (1995) on the mean circulation in the Atlantic Ocean and the DYNAMO intercomparison project of forward models of different types (Willebrand et al., 2001).

The transport estimates derived from both **LEV**, **LOZ** and **GUR** solutions are compared to these works in table 5.2. Generally, transports are computed for different classes of density (in between two isopycnals). Lumpkin and Speer (2003) use isopycnal  $\sigma = 27.7$  to distinguish between the upper and deep ocean waters while Schott et al. (2004) use  $\sigma = 27.68$  for the same purpose. In our case, due to oversmoothed bottom topography the currents are slightly shifted from their normal positions and we distinguish between the upper and deep waters only approximately by taking approximate position of the mean of isopycnals. However, our results agree with their estimates.

For the **LOZ** assimilation, we estimate that the Florida current brings 31 Sv of water north and 19 Sv is returned to the South by the DWBC across section A5 at 24° N. This perfectly agrees with the estimates given by Lumpkin and Speer (2003) and Schiller (1995). The estimates by Lumpkin and Speer (2003) across this section are  $30\pm 2$  and  $19\pm 9$  for the Florida current and DWBC respectively. Schiller (1995) gives estimates to the transport of DWBC 14.6–20.9 Sv depending on the dataset and parametrization of the diffusion.

We slightly underestimate these transports in **GUR** experiment in comparison to **LEV** and **LOZ** across A5. However, further north transport estimates from **GUR** experiment across AR1 get values in between **LEV** and **LOZ** solutions which are of about 33 Sv for the northward and about 14 Sv for the southward transports. This tells that velocity pattern corresponding to **GUR** solution shows stronger recirculation at this latitude.

The information on transports in section A2 is rather controversial (see table 5.2), yet our solutions are on the lower limit of these estimates for the upper northward transport which in our case is 36.4 Sv. Our value of the lower deep northward transport of 14 Sv agrees with other results.

We see that around 30 Sv leaves the Labrador Sea through M50 which is below than the estimate of 37.2 Sv given by Fischer et al. (2004). We also underestimate the southward transport across AR7E which is  $33\pm 4$  Sv in the result of Lumpkin and Speer (2003). In our case it is only about 25 Sv for the **LOZ** solution and 26 Sv for **GUR**.

The comparison of the transports computed from **LOZ**, **LEV** and **GUR** (table 5.2) solutions shows that the inverse of Levitus data tends to underestimate the northward and southward transports. This can be a consequence of Lozier and Gouretski having more data in the western part of the subpolar North Atlantic. As a result, these datasets are smoothed with smaller radius and reproduce sharper gradients compared with the Levitus data (Marotzke and Willebrand, 1996).

We also compare **LOZ** transports and velocities through AR1 section to the results of DYNAMO models (Willebrand et al., 2001). These are forward models of  $1/3^\circ$  resolution. They use  $z$ , sigma and isopycnal vertical discretizations. From Table 5.2 it can be seen that the IFEOM agrees well with the mean output of DYNAMO models. To illustrate the quality of our inverse solutions we plot the mean meridional velocity through AR1 section for DYNAMO models (Fig. 5.31) and compare it to **LOZ** velocity (Fig. 5.32). The maximum velocities in DWBC are of -13 cm/s, -7 cm/s, -15 cm/s for LEVEL, ISOPYCNIC and SIGMA models respectively. **LOZ** solution reproduces DWBC with a core velocity of -8 cm/s. The core of DWBC is located at about 2000m depth.

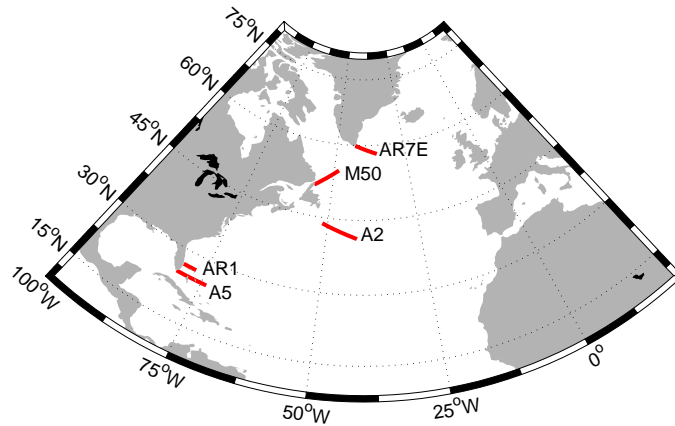


Figure 5.30: The map of sections through the North Atlantic where the transports of the inverse solutions are computed.

section	LEV	LOZ	GUR	others	
Upper A5 (North)	29.3	30.9	25.1	30±2	Lum
Deep A5 (South)	21.6	19.4	16.6	19±9 14.6–20.9	Lum Schi
Upper AR1 (North)	32.1	38.5	33.2	35 (LEVEL) 36 (SIGMA) 38 (ISOPYCNIC)	DYN
Deep AR1 (South)	14.1	15.9	14.2	17 (LEVEL) 16 (SIGMA) 11 (ISOPYCNIC)	DYN
Upper A2 (North)	20.8	36.4	34.3	33±3 81.2 (mean for 1993-2001) 65.8±25.0 (for 1993-1995) 39.4 (July 1999) 47.2 (May 2001)	Lum Sch
Deep A2 (South)	10.5	14.1	12.3	29±12 12.2 (mean for 1993-2001) 15.0±7.0 (for 1993-1995)	Lum Sch
Total M50 (South)	27.9	29.4	30.1	37.2	Fis
Total AR7E (South)	24.7	25	26.2	33±4	Lum

Table 5.2: Transport estimates across sections through the North Atlantic [Sv]

Lum From Lumpkin and Speer (2003)

Sch From Schott et al. (2004)

Schi From Schiller (1995)

Fis From Fischer et al. (2004)

DYN From DYNAMO models (Willebrand et al., 2001)

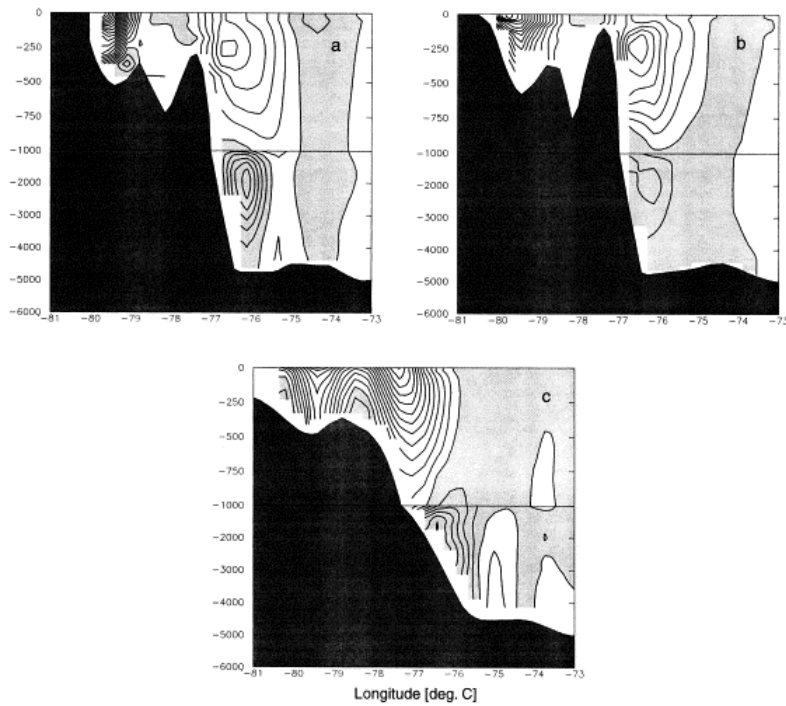


Figure 5.31: Comparison of three DYNAMO models of  $1/3^\circ$  degree resolution across AR1 section. Panels *a*, *b*, *c* are the results for LEVEL, SIGMA and ISOPYCNAL models, respectively. The core velocities in DWBC are of -13 cm/s, -7 cm/s, -15 cm/s for LEVEL, ISOPYCNIC and SIGMA models respectively.

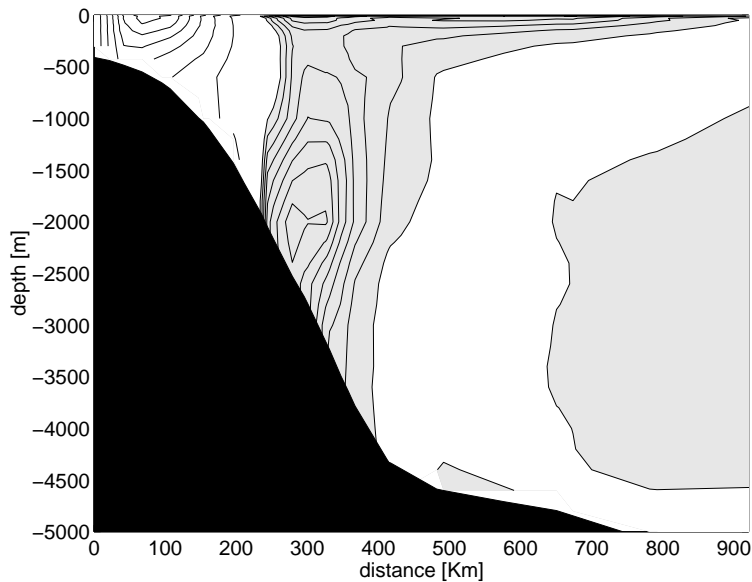


Figure 5.32: The velocity across AR1 section corresponding to the **LOZ** solution. Contour intervals are of 0.1 m/s for the northward velocities and 1 cm/s for southward ones. The area of southward transport is shaded.

## 5.12 Interpentadal variability

In this section, we return to the assimilation of the Lozier et al. (1995) data set to discuss the variability derived from assimilation of separate pentades. Table 5.3 and accompanying it Fig. 5.33 present time series of transports across the sections described earlier in the North Atlantic which are computed from the set of inverse solutions.

The variability that could be detected from the inverse solutions is on the order from a fraction of Sv to 10 Sv depending on the section. The largest variability is found across AR1 and A2 section. The result with respect to A2 section is not surprising given the large scatter in transport estimates obtained by other authors (see table 5.2).

section	year								
	50-54	55-59	60-64	65-69	70-74	75-79	80-84	85-89	90-94
Upper A5 (North)	30.2	29.2	31.3	29.5	31.0	32.9	30.1	31.1	31.3
Deep A5 (South)	20.0	20.3	19.6	18.5	18.5	19.2	20.3	18.9	20.3
Upper AR1 (North)	37.2	38.5	38.7	36.9	37.9	40.0	35.7	37.3	38.8
Deep AR1 (South)	15.6	16.9	16.1	15.1	14.9	15.4	15.6	15.5	15.6
Upper A2 (North)	37.7	35.3	33.5	35.9	31.9	31.1	36.2	41.2	39.9
Deep A2 (South)	14.2	13.3	13.3	14.6	11.9	12.3	12.0	16.1	13.9
Total M50 (South)	29.7	29.9	29.3	29.3	28.6	29.3	29.4	29.8	29.5
Total AR7E (South)	25.9	25.2	24.3	23.8	24.3	25.1	25.6	26.2	24.3

Table 5.3: Time series of transports through some sections computed from nine inverse solutions.

By inspecting curves for transports through the sections we conclude that southward and northward transports are correlated, especially at the north of the basin (see the figure caption for labeling the curves). This is obviously the result of volume conservation which is accounted for in our model equations as a strong constraint (see chapter 4) and the fact that the sections are located in the western part of the basin.

The variability in transports is also reflected in the barotropic streamfunction. It is plotted in Fig. 5.34. Its standard deviation (Fig.5.35) shows the largest amplitude in the region of the Gulf Stream where it reaches 6 Sv. This variability is much smaller than the results obtained by Myers et al. (2004) working with the same Lozier et al. (1995) data set. He reports much larger variability (up to 20 Sv over certain areas). However, in his case only diagnosis of the data was carried out with a 2D model (including effects of JEBAR), so it may happen that partly the large signal is due to inconsistency between the bottom topography and the data.

The mean meridional overturning streamfunction and its variability are shown in Figures 5.36 and 5.37 (left panel), respectively. The maximum of MOC is located at about 43°N and has the mean value of about 14 Sv. It shows small interpentadal changes of about 1 Sv. These small magnitudes are consistent with those produced by the forward models when averaged over a

five-year time span, as follows from comparison with paper by Beismann and Barnier (2004) presented in Fig. 5.37 (right panel). However our variability does not correlate with their very well. The possible reason could be that their hydrographic fields produced by the forward run are different from the Lozier data and are influenced by a particular surface heat and freshwater.

The other reason can be that we constrained the deep pressure gradient to the same field (computed from the FEOM run for ten years) in each assimilation run. Although one would expect the deep circulation not to vary very much on the time scale of five years, the changes in the meridional overturning are really small so that small changes in the deep ocean circulation could matter.

The fact is that both our estimates and the results by Beismann and Barnier (2004) show very small changes in the MOC on interpentadal time scales.

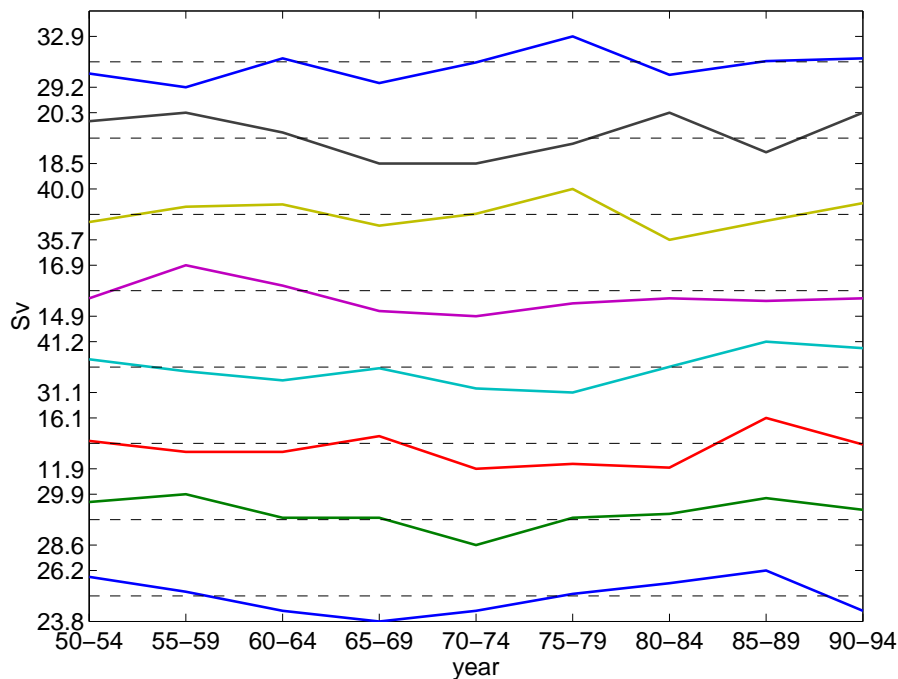


Figure 5.33: Time series of transports. The plot corresponds to the table 5.3 and represents the transport variability (from top to bottom) for the following waters and sections: Upper A5 (North), Deep A5 (South), Upper AR1 (North), Deep AR1 (South), Upper A2 (North), Total M50 (South) and Total AR7E (South).

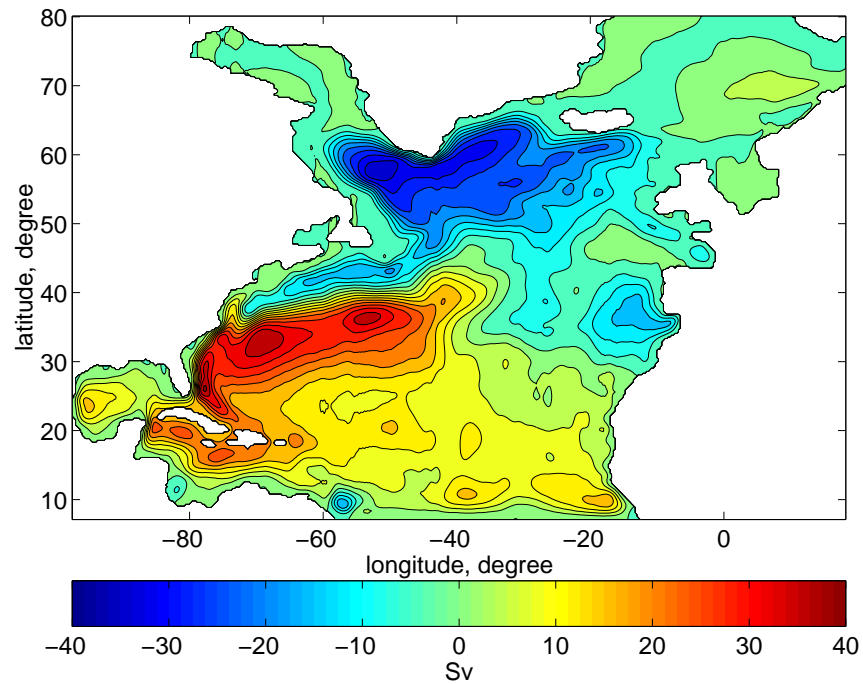


Figure 5.34: The mean barotropic streamfunction corresponding to the **LOZ** solution. Contour interval is 4Sv.

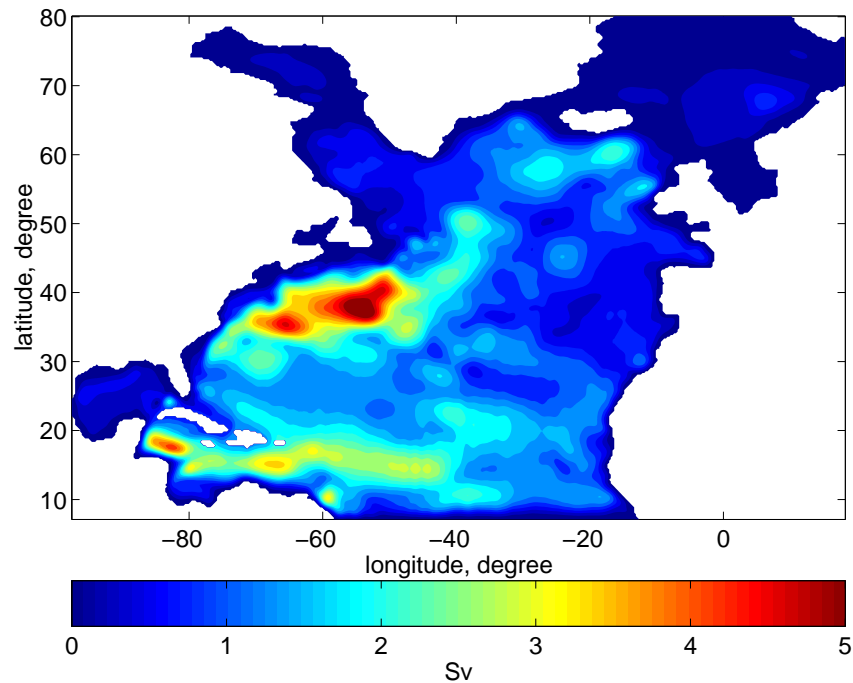


Figure 5.35: The standard deviations of barotropic streamfunction computed from nine inverse solutions.

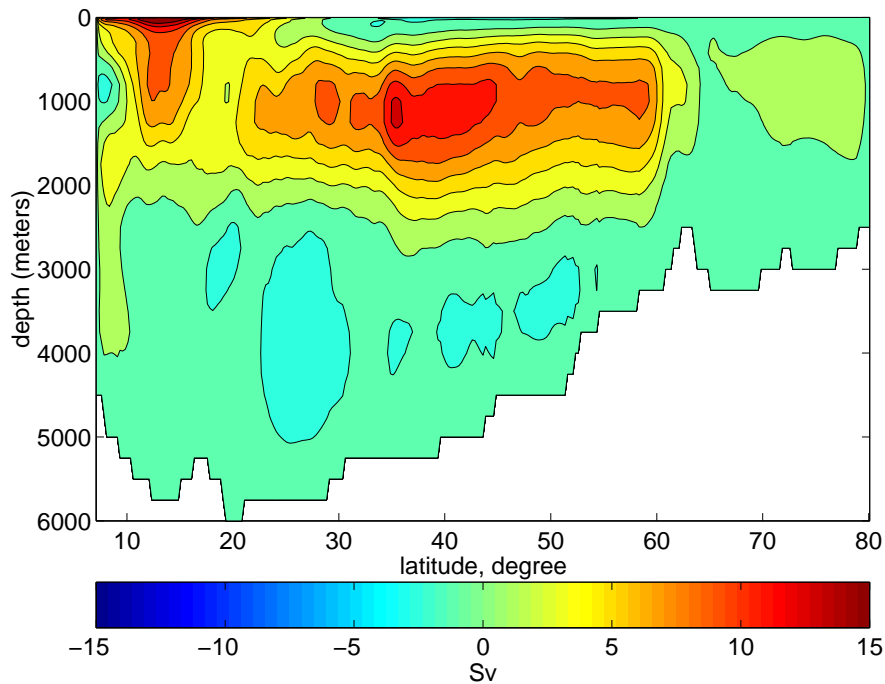


Figure 5.36: The mean meridional overturning streamfunction corresponding to the **LOZ** solution. The maximum overturning is 13.6 Sv. Contour interval is 2 Sv.

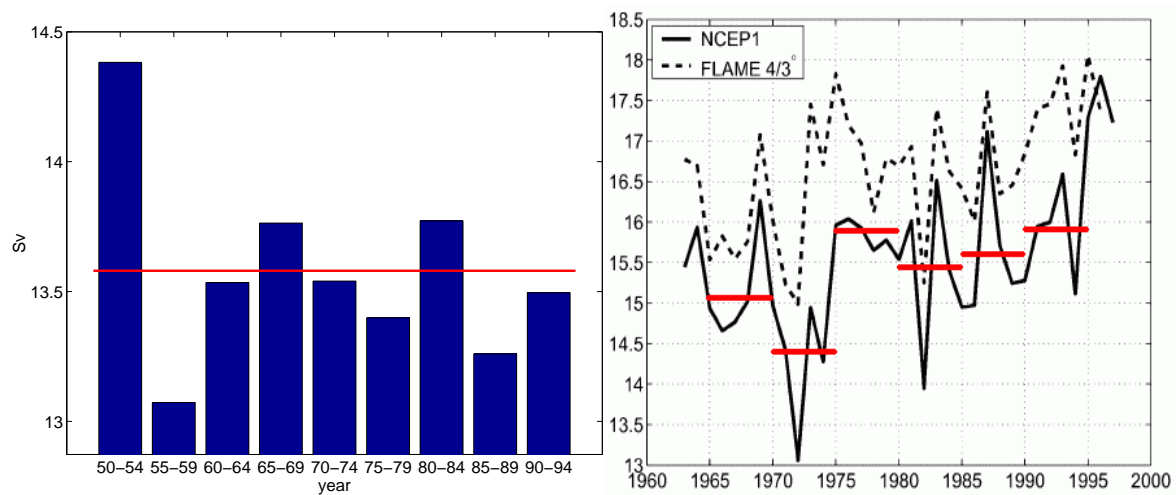


Figure 5.37: Time series of the maximum value of the overturning streamfunction at  $43^\circ\text{N}$  computed for nine inverse solutions (left panel). The red line corresponds to the mean value of 13.6 Sv. Comparison of time series of the overturning streamfunction at  $48^\circ\text{N}$  produced by two forward models (right panel, after Beismann and Barnier (2004)). Bars denote the mean values over five years period for the NCEP1 experiment.

# Chapter 6

## Conclusions

The goal of this thesis was the development of two numerical models for data assimilation and using them for transport estimates in the North Atlantic.

The first model called FEMSECT estimates transports across a hydrographic section by combining hydrography and mooring data in a least square sense. It was developed together by M. Losch and the author of this thesis and is described, together with applications, in chapter 3. The FEMSECT uses thermal wind relations to estimate the velocity shear across the section. The reference velocity and hydrographic fields (temperature and salinity) are treated as control parameters which are varied to find the optimal state which corresponds to the minimum of an objective function. The novel aspect of FEMSECT is the use of finite elements to discretize the thermal wind relations. This alone leads to some advantages over traditional section models since it makes possible using flexible computational grids which can represent the bottom topography in a smooth piece-wise linear way. Furthermore, the finite element method gives continuous representation of model parameters everywhere within the domain which simplifies estimating the difference between the model state and the data.

The estimates of transports through the Fram Strait performed with FEMSECT show the skill of the model in compensating for the omissions of the current meter data compared to estimates based on only interpolating these data. This demonstrates the ability of the model to interpolate the data within the section in a consistent way. The FEMSECT is already used at AWI for interpreting observational data, and more details on Fram Strait transports will be reported in a paper that is in preparation (Losch et al., 2004).

The second model called IFEOM was designed by the author based on the prognostic Finite Element Ocean Model (FEOM) (Danilov et al., 2004a,b). The main motivation for developing the IFEOM was the need for local and global volume conservation which could be achieved by looking for a solution within some 3D domain and using full momentum and continuity equations to compute the velocity field. The IFEOM can use density, open boundary velocities and the wind stress as control parameters and seek for a compromise

between the data and model results. The data can include density, altimetry, wind stress and open boundary velocities, in addition to deviations from the data, the cost function penalizes residuals of the stationary equation for the potential density.

The success of IFEOM in practical terms is linked to using one more constraint suggested by the author. Namely, the cost function includes a term which penalizes the deviation of the model deep pressure gradient (below 2000 m) from that of the forward run of FEOM. The physical motivation behind this constraint is in keeping the deep circulation nearly intact while assimilating the data. The constraint forces the adaptation of the density field to occur mostly over the upper ocean which agrees with our expectation that largest changes in the density structure are observed within the thermocline.

The IFEOM was applied to reconstruct the circulation in the North Atlantic given the Levitus atlas (Levitus et al., 1994; Levitus and Boyer, 1994), nine pentades of Lozier hydrography (Lozier et al. (1995)) and the novel climatology by Gouretski and Koltermann (2004) which is based on WOCE Hydrographic program, as data.

We analyze transports through several sections (A5, AR1, A2, M50 and AR7E) and demonstrate that they compare reasonably well with recent estimates done by other authors as follows from table 5.30. Our general result is that solution based on the Levitus climatology underestimates transports in the North Atlantic through almost all sections, and the solutions based on the mean Lozier climatology and that of Gouretski and Koltermann (2004) are in better agreement with the results of other authors. In addition, we showed that the climatology of Gouretski and Koltermann (2004) reproduces some details of circulation (like Gulf Stream separation and the Labrador Current) better than other data sets. The main conclusion from the comparison of solutions obtained from different data sets is that Lozier et al. (1995) and Gouretski and Koltermann (2004) are more dynamically consistent in the North Atlantic.

We also present the interpentadal variability of the circulation in the North Atlantic as derived from the nine pentades of the Lozier climatology. The variability of the barotropic streamfunctions reaches 6 Sv while it is much smaller in the meridional overturning streamfunction where it is only a fraction of a Sv.

The results obtained by us here on the circulation in the North Atlantic present only an initial phase of using IFEOM. It is our future plan to augment the IFEOM by functionality of assimilating separate sections and the surface heat and freshwater (buoyancy) fluxes, and apply it to systematic estimates of transports in the North Atlantic and, hopefully, in other areas of the World Ocean.

# Bibliography

- Barber, C. B., Dobkin, D. P., Huhdanpaa, H. T., 1996. The quickhull algorithm for convex hulls. *ACM Transactions on Mathematical Software* 22 (4), 469–483.
- Beismann, J. O., Barnier, B., 2004. Variability of the meridional overturning circulation of the North Atlantic: sensitivity to overflows of dense water masses. *Ocean Dynamics* 54, 92–106.
- Bennett, A. F., 2002. *Inverse methods in physical oceanography*. Cambridge University Press, Cambridge.
- Conkright, M., Antonov, J. I., Baranove, O., Boyer, T. P., Garcia, H., Gelfeld, R., Johnson, D., Locarnini, R. A., Murphy, P., O'Brien, T. D., Smolyar, I., Stephens, C., 2002. *World Ocean Database 2001. Vol.1: Introduction*. NOAA Atlas NESDID 42. U.S.Gov. Printing office, Washington, D.C.
- Danilov, S., Kivman, G., Schröter, J., 2004a. A finite-element ocean model: principles and evaluation. *Ocean Modelling* 6, 125–150.
- Danilov, S., Kivman, G., Schröter, J., 2004b. Evaluation of an eddy-permitting finite-element ocean model in the North Atlantic. *Ocean Modelling* in press.
- Dimet, F. X. L., Talagrand, O., 1986. Variational algorithms for analysis and assimilation of meteorological observations: Theoretical aspects. *Tellus* 38A, 97–110.
- Dobrindt, U., Schröter, J., 2003. An adjoint ocean model using finite elements: An application to the South Atlantic. *J. Atmos. Ocean Tech.* 20, 392–407.
- Eden, C., Greatbatch, R., 2003. Adiabatically correcting an eddy-permitting model using large-scale hydrographic data: Application to the Gulf Stream and the North Atlantic current. *J. Phys. Oceanogr.* 34, 701–719.
- Fahrbach, E., Meincke, J., Osterhus, S., Rohardt, G., Schauer, U., Tverberg, V., Verduin, J., 2001. Direct measurements of volume transports through Fram Strait. *Polar Res.* 20 (2), 217–224.

- Fischer, J., Schott, A., Dengler, M., 2004. Boundary circulation at the exit of the Labrador Sea. *J. Phys. Oceanogr.* 34, 1548–1570.
- Ganachaud, A., Wunsch, C., 2000. Improved estimates of global ocean circulation, heat transport and mixing from hydrographic data. *Nature* 408, 453–457.
- Ganachaud, A., Wunsch, C., 2003. Large-scale ocean heat and freshwater transport during the World Ocean Circulation Experiment. *J. Climate* 16, 696–705.
- Gilbert, J., Lemaréchal, C., 1989. Some numerical experiments with variable storage quasi-Newton algorithms. *Mathematical Programming* 45, 407–435.
- Gilbert, J. C., Lemaréchal, C., 1993. The modules M1QN3 and N1QN3. Tech. Rep. ver 2.0, INRIA, France.
- Gouretski, V. V., Koltermann, K. P., 2004. WOCE Global Hydrographic Climatology. Bundesamt für Seeschifffahrt und Hydrographie, Hamburg und Rostock, Germany.
- Hellerman, S., Rosenstein, M., 1983. Normal monthly wind stress over the world ocean with error estimates. *J. Phys. Oceanogr.* 13, 1093–1104.
- Johnson, C., 1990. Numerical solution of partial differential equations by the finite element method. Cambridge University Press, Cambridge.
- Karypis, G., Kumar, V., 1998. Parallel threshold-based ILU factorization. Tech. Rep. 96-061, University of Minnesota.
- Kelley, C. T., 1999. Iterative Methods for Optimization. No. 18 in *Frontiers in Applied Mathematics*. SIAM, Philadelphia.  
URL <http://www.ec-securehost.com/SIAM/FR18.html>
- Le Provost, C., Lyard, F., Molines, J., Genco, M., Rabilloud, F., 1998. A hydrodynamic ocean tide model improved by assimilating a satellite altimeter-derived data set. *J. Geophys. Res.* 103 (C3), 5513–5529.
- Levitus, S., 1982. Climatological atlas of the world ocean. Tech. Rep. 13, U. S. Department of Commerce, National Oceanographic and Atmospheric Administration.
- Levitus, S., Boyer, T., 1994. World Ocean Atlas. Salinity, Vol.3. Vol. 4. NOAA, Washington DC.
- Levitus, S., Boyer, T., Conkright, M., O'Brien, T., Antonov, J., Stephens, C., Stathopoulos, L., Johnson, D., Gelfeld, R., 1998. World Ocean Database 1998. Vol.1: Introduction. NOAA Atlas NESDID 18. U.S.Gov. Printing office, Washington, D.C.

- Levitus, S., Burgett, R., Boyer, T., 1994. World Ocean Atlas. Salinity. Vol. 3. NOAA, Washington DC.
- Liu, D., Nocedal, J., 1989. On the limited memory bfgs method for large scale optimization. *Mathematical Programming* 45, 503–528.
- Losch, M., Redler, R., Schröter, J., 2002. Estimating a mean ocean state from hydrography and sea-surface height data with a non-linear inverse section model: Twin experiments with a synthetic data set. *J. Phys. Oceanogr.* 32 (7), 2096–2112.
- Losch, M., Sidorenko, D., Beszczynska-Möller, A., 2004. FEMSECT: an inverse section model based on the finite element method. in preparation .
- Lozier, M. S., Owens, W. B., Curry, R. G., 1995. The climatology of the North Atlantic. *Progr. Ocean.* 36, 1–44.
- Lumpkin, R., Speer, K., 2003. Large-scale vertical and horizontal circulation in the North Atlantic ocean. *J. Phys. Oceanogr.* 33, 1902–1920.
- Macdonald, A. M., 1995. Oceanic fluxes of mass, heat and freshwater: A global estimate and perspective. Ph.D. thesis, Department of Earth, Atmospheric and Planetary Sciences, Massachusetts Institute of Technology, Cambridge, MA.
- Macdonald, A. M., 1998. The global ocean circulation: a hydrographic estimate and regional analysis. *Progress in Oceanography* 41, 281–382.
- Marotzke, J., 1992. The role of integration time in determining the steady state through data assimilation. *J. Phys. Oceanogr.* 22, 1434–1457.
- Marotzke, J., Willebrand, J., 1996. The North Atlantic mean circulation: Combining data and dynamics. In: *The Warmwatersphere of the North Atlantic Ocean*, W. Krauss. Gebrüder Borntraeger, Berlin, Germany.
- Marotzke, J., Wunsch, C., 1993. Finding the steady state of a general circulation model through data assimilation: Application to the North Atlantic ocean. *J. Geophys. Res.* 98, 20149–20167.
- Martel, F., Wunsch, C., 1993. The North Atlantic circulation in the early 1980s — An estimate from inversion of a finite-difference model. *J. Phys. Oceanogr.* 23, 898–923.
- Mercier, H., Ollitrault, M., 1993. An inverse model of the North Atlantic general circulation using Lagrangian float data. *J. Phys. Oceanogr.* 23, 689–715.

- Morgan, P. P., 1994. SEAWATER: A library of MATLAB computational routines for the properties of sea water. Tech. Rep. 222, CSIRO Marine Laboratories.
- Myers, P., Grey, S., Haines, K., 2004. A diagnostic study of interpentadal variability in the North Atlantic ocean using finite element model. *Ocean Modelling* (in press).
- Myers, P. G., 1995. A diagnostic barotropic finite-element ocean circulation model. *J. Atmos. Ocean Tech.* 12, 511–526.
- Nechaev, D., Schröter, J., Yaremchuk, M., 2003. A diagnostic stabilized finite-element ocean circulation model. *Ocean Modelling* 5, 37–63.
- Nechaev, D., Yaremchuk, M., 1995. Application of the adjoint technique to processing of a standard section dataset: World ocean circulation experiment section s4 along 67s in the pacific ocean. *J. Geophys Res.* 100, 865–879.
- Nechaev, D., Yaremchuk, M., Ikeda, M., 2004. Decadal variability of circulation in the Arctic Ocean retrieved from climatological data by a variational method. *J. Geophys. Res.* 109 (C04006), doi:10.1029/2002JC001740.
- Nocedal, J., 1980. Updating quasi-newton matrices with limited storage. *Mathematics of Computation* 35/151, 773–782.
- Olbers, D., Eden, C., 2003. A simplified general circulation model for a baroclinic ocean with topography. Part I: Theory, waves and wind-driven circulations. *J. Phys. Oceanogr* 33 (12), 2719–2737.
- Olbers, D., Wenzel, M., Willebrand, J., 1985. The inference of North Atlantic circulation patterns from climatological hydrographic data. *Rev. Geophysics* 23, 313–356.
- Rintoul, S. R., Wunsch, C., 1991. Mass heat, oxygen and nutrient fluxes and budgets in the North Atlantic Ocean. *Deep-Sea Res.* 38 Suppl. 1., S355–S377.
- Roemmich, D., Wunsch, C., 1985. Two transatlantic sections: Meridional circulation and heat flux in the subtropical North Atlantic ocean. *Deep-Sea Res.* 32, 619–664.
- Rudels, B., Meyer, R., Fahrbach, E., Ivanov, V., Osterhus, S., Quadfasel, D., Schauer, U., Tverburg, V., Woodgate, R. A., 1999. The water mass distribution in Fram Strait and over the Yermak Plateau in summer 1997. submitted to *Ann. Geophys* .
- Schauer, U., Fahrbach, E., Osterhus, S., Rohardt, G., 2004. Arctic warming through the Fram Strait - oceanic heat transport from three years of measurements. *J. Geophys. Res.* 109 (C0), 6026, doi:10.1029/2003JC001823.

- Schiller, A., 1995. The mean circulation of the Atlantic Ocean north of 30s determined with the adjoint method applied to an ocean general circulation model. *J. Mar. Res.* 53, 453–497.
- Schiller, A., Willebrand, J., 1995. A technique for the determination of surface heat and freshwater fluxes from hydrographic observations, using an approximate adjoint ocean circulation model. *J. Mar. Res.* 53, 433–451.
- Schlichtholz, P., Houssais, A., 1999. An inverse modelling study in Fram Strait, part ii: Water mass distribution and transport. *Deep Sea Res.* 46 (6–7), 1137–1168.
- Schlitzer, R., 1993. Determining the mean, large-scale circulation of the Atlantic with the adjoint method. *J. Phys. Oceanogr.* 23, 1935–1952.
- Schlitzer, R., 1995. An adjoint model for the determination of the mean oceanic circulation, air-sea fluxes and mixing coefficients. Reports on Polar Research, Alfred Wegener Institute for Polar and Marine Research, Bremerhaven 156, 103pp.
- Schott, A., Zantopp, R., Stramma, L., Dengler, M., Fischer, J., Wibaux, M., 2004. Circulation and deep-water export at the western exit of the subpolar North Atlantic. *J. Phys. Oceanogr.* 34, 817–843.
- Stammer, D., Wunsch, C., Giering, C., Eckert, C., Heimbach, P., Marotzke, J., Adcroft, A., Hill, C. N., Marshall, J., 2002. The global ocean circulation during 1992 -1997, estimated from ocean observations and a general circulation model. *J. Geophys. Res.* 107 (C9), 3118–3145.
- Stammer, D., Wunsch, C., Giering, C., Eckert, C., Heimbach, P., Marotzke, J., Adcroft, A., Hill, C. N., Marshall, J., 2003. Volume, heat and freshwater transports of the global ocean circulation 1993 –2000, estimated from a general circulation model constrained by world ocean circulation experiment (WOCE) data. *J. Geophys. Res.* 108 (C1 3007), doi:10.1029/2001JC001115.
- Thacker, W. C., 1989. On the role of the Hessian matrix in fitting models to data. *J. Geophys. Res.* 94 (C5), 6177–6196.
- Trenberth, K. E., Large, W. G., Olson, J. G., 1990. The mean annual cycle in global ocean wind stress. *J. Phys. Oceanogr.* 20, 1742–1760.
- Tziperman, E., Thacker, W. C., Long, R. B., Hwang, S. H., 1992a. Oceanic data analysis using a general circulation model. part 1: Simulations. *J. Phys. Oceanogr.* 22 (12), 1434–1457.
- Tziperman, E., Thacker, W. C., Long, R. B., Hwang, S. H., 1992b. Oceanic data analysis using a general circulation model. part 2: A North Atlantic. *J. Phys. Oceanogr.* 22 (12), 1458–1485.

- Walters, R. A., 1987. A model for tides and currents in the English Channel and Southern North Sea. *Adv. in Water Resources* 10 (3), 138–148.
- Wenzel, M., 1986. Die mittlere Zirkulation des Nordatlantik auf der Grundlage klimatologischer hydrographischer Daten. *Berichte* 157, Institut für meereskunde an der Christian–Albrechts–Universität Kiel.
- Wenzel, M., Schröter, J., Olbers, D., 2001. The global ocean circulation during 1992–1997, estimated from ocean observations and a general circulation model. *Prog. in Oceanogr.* 48 (C9), 73–119.
- Willebrand, J., Barnier, B., Böning, C., Dietrich, C., Killworth, P., Provost, C. L., Jia, Y., Molines, J.-M., New, A., 2001. Circulation characteristics in three eddy-permitting models of the North Atlantic. *Progr. Ocean.* 48, 123–161.
- Wunsch, C., 1977. Determining the general circulation of the oceans: A preliminary discussion. *Science* 196, 871–875.
- Wunsch, C., 1996. *The Ocean Circulation Inverse Problem*. Cambridge University Press, Cambridge.
- Yu, L., Malanotte-Rizzoli, P., 1996. Analysis of the North Atlantic climatologies using a combined OGCM/adjoint approach. *J. Mar. Res.* 54 (5), 867–913.
- Yu, L., Malanotte-Rizzoli, P., 1998. Inverse modelling of seasonal variations in the North Atlantic ocean. *J. Phys. Oceanogr.* 28 (5), 902–922.
- Zienkiewicz, O. C., Taylor, R. L., 2000a. *The Finite Element Method*, 5th Edition. Vol. 1: The Basis. Butterworth Heinemann.
- Zienkiewicz, O. C., Taylor, R. L., 2000b. *The Finite Element Method*, 5th Edition. Vol. 2: Solid Mechanics. Butterworth Heinemann.
- Zienkiewicz, O. C., Taylor, R. L., 2000c. *The Finite Element Method*, 5th Edition. Vol. 3: Fluid Dynamics. Butterworth Heinemann.

# Acknowledgements

Working at this thesis has been very pleasurable on account of a creative and helpful atmosphere in the research group. Needless to say, it has been a tremendous learning experience for me, and I would like to say great thank you to all the people who were close to me all this time.

First, I would like to thank my supervisor Dr. Jens Schröter for giving me the opportunity to perform the PhD study in his research group, providing a stimulating working environment, as well as his guiding support and care for the project and me.

I am particularly grateful to Dr. Sergey Danilov for his invaluable help during my PhD, sharing his great expertise and inexhaustible ideas concerning oceanography with me and for his detailed and stimulating commentaries on the work at every stage of its development.

With a special vote of thanks to Dr. Gennady Kivman who recommended me for a PhD position, first introduced me to the concept of the model and has shared his almost infinite knowledge of oceanography with me. He also made helpful comments on drafts of the thesis, and I am very much in his debt.

Special thanks to Dr. Martin Losch and Dr. Agnieszka Beszczynska for performing a part of my work together with me.

I would also like to record here my appreciation to the reviewers Prof. Dr. Dirk Olbers and Prof. Dr. Reiner Schlitzer for their detailed reading of the work and valuable comments.

Once more, I am grateful to Dr. Sven Harig, Ismael Nunez-Riboni, Dr. Manfred Wenzel and Dr. Svetlana Loza for advice and assistance.

Finally I am infinitely thankful to my parents, my brother, and his wife Julia for their wisdom, patience and love.